On the Population of the 5:1 Neptune Resonance

by

Rosemary Ellen Pike
B.Sc., Massachusetts Institute of Technology, 2007

A Thesis Submitted in Partial Fulfillment of the
Requirements for the Degree of

DOCTOR OF PHILOSOPHY

in the Department of Physics & Astronomy

On the Population of the 5:1 Neptune Resonance

by

Rosemary Ellen Pike
B.Sc., Massachusetts Institute of Technology, 2007

Supervisory Committee

Dr. JJ Kavelaars, Co-Supervisor
(Department of Physics & Astronomy)

Dr. Kim Venn, Co-Supervisor
(Department of Physics & Astronomy)

Dr. Colin Goldblatt, Outside Member
(Department of Earth & Ocean Sciences)

Supervisory Committee

Dr. JJ Kavelaars, Co-Supervisor
(Department of Physics & Astronomy)

Dr. Kim Venn, Co-Supervisor
(Department of Physics & Astronomy)

Dr. Colin Goldblatt, Outside Member
(Department of Earth & Ocean Sciences)

ABSTRACT

The recent discovery of objects near the 5:1 Neptune resonance prompts the study of the size, structure, and surface properties of this population to determine if these parameters are consistent with a 'Nice model' type evolution of the outer Solar System. Previous TNO discovery surveys have primarily targeted the ecliptic plane, where discovery of high inclination objects such as the 5:1 resonators is unlikely, and theoretical work on the evolution of the outer Solar System has focused on structure in and around the main Kuiper belt and largely ignored the distant resonant TNOs. I tracked these objects for several semesters, measured their positions accurately, and determined precise orbits. Integrating these orbits forward in time revealed that three objects are 5:1 resonators, and one object is not resonant but may have been resonant in the past. I constrained the structure of the 5:1 resonance population based on the three detections and determined that the minimum population in this resonance was much larger than expected, 1900^{+3300}_{-1400} with $H_g < 8$. I compared this large population with the orbital distribution of TNOs resulting from a Nice model evolution and determined that the population in the real 5:1 resonance is $\sim$20–100 times larger than the model predicts. However, the structure of the 5:1 resonance in this model was consistent with the orbital distribution I determined based on the detections. The orbital distribution of the scattering population in the Nice model is consistent with

other models and survey results, leading to the conclusion that the 5:1 resonance cannot be a steady state transient population produced via resonance sticking from the scattering objects. To test the origin of the 5:1 resonators, I measured the objects' surface colors in multiple wavelength ranges and compared their surface reflectance to TNOs from a large color survey, ColOSSOS. The 5:1 resonators have a consistent selection criteria to the TNOs from the ColOSSOS survey, so these samples have known selection biases and can be usefully compared to each other. The surfaces of the three 5:1 resonators showed three different spectral reflectance shapes, indicating that these three objects do not share a common formation location. The surface properties and orbital distribution of current 5:1 resonators are consistent with the remnant of a large captured population, partially resupplied by the scattering objects. However, the scattering event which produced this large 5:1 population remains unexplained.

Contents

List of Tables

List of Figures

Chapter 1

Introduction

This thesis focuses on objects in the trans-Neptunian region, the remnant disk from the formation of the Solar System. The surface colors of trans-Neptunian objects (TNOs) provide information about their surface composition, and their dynamical characteristics provide insight into the evolution of the Solar System. Understanding the small bodies in the outer Solar System also provides constraints on theories of planet formation in general. My work benefits from the significant efforts from both theorists and observers to understand the origin and history of the Kuiper belt.

1.1 Discovery of the Kuiper Belt

One of the earliest indications of large reservoirs of objects beyond Neptune was the observations of comets. The orbits of comets are not long term stable; they can be ejected, collide with other Solar System bodies, or disintegrate during perihelion passage. Because these objects are unstable, they must be continuously resupplied by a reservoir. Two types of comets are evident, short and long period comets. A plot of the Solar System, depicting typical orbits for short and long period comets as well as the planetary orbits, is shown in Figure 1.1. The importance of their different dynamical origins was quantified in Levison (1996), who proposed a comet taxonomy based on the dynamical tie between the objects and Jupiter. The long period comets, with periods of > 200 years, are believed to originate in the Oort cloud (Oort, 1950), a spherical distribution of small bodies at $\sim 10^4$ AU. These Oort cloud comets approach the inner Solar System at random angles relative to the ecliptic plane, the plane in which the Earth orbits the Sun. At thousands of AU, the proposed distance of the

Oort cloud, galactic tides affect the orbits of the objects and remove any preference for orbits in the ecliptic plane. The short period comets have lower inclinations and periods < 200 years. The Jupiter Family Comets (JFCs) are a subset of short period comets, with periods < 20 years. These objects must come from a source population that is both more confined to the ecliptic plane and much closer to the giant planets. A belt of objects beyond Neptune's orbit would provide such a cometary reservoir.

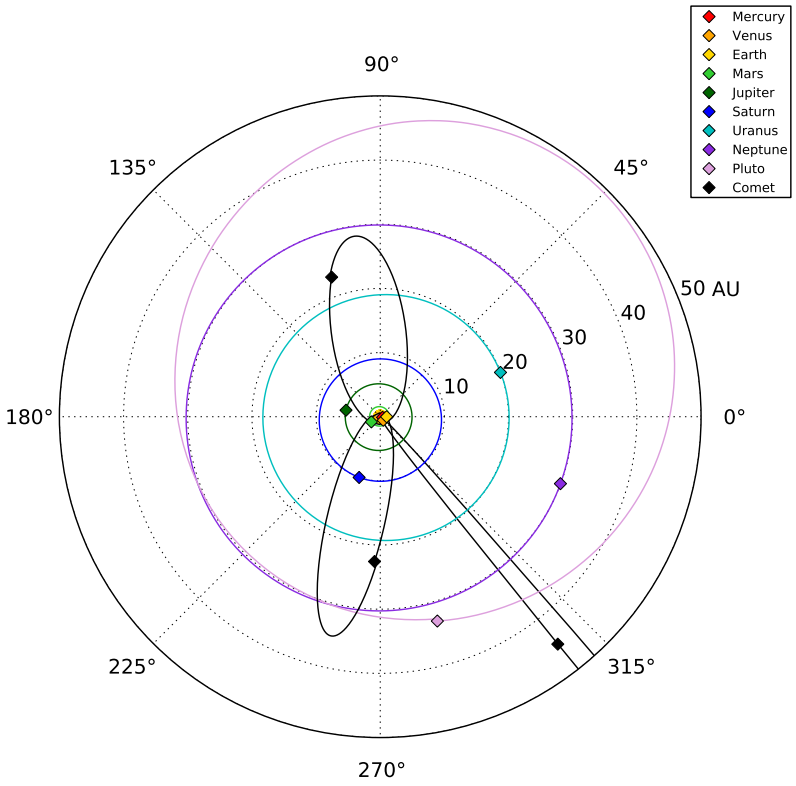

Figure 1.1 This is the Solar System as viewed from above. The orbits of the planets and Pluto are shown, and their position is indicated for March 21, 2016. This is the date of the vernal Equinox, when the Sun crosses the Earth's equatorial plane. The relative scale of planetary orbits is immediately apparent, the terrestrial planets are all clumped in the center of the plot. The non-circularity (ellipticity) of the orbits is noticeable, particularly for Pluto and the comet orbits. The comet orbits are not specific object orbits; these orbits are meant to illustrate typical cometary orbits. The two fully visible orbits are short period comets, and the orbit which exits the region plotted is a long period comet, with an orbit that would approach the Oort cloud, at a few thousand AU.

A variety of sources speculated on the existence of small bodies beyond Neptune. One of the general theories of cometary origin was that the Jupiter family comets are

'fragments' of the outer regions of the nebula from which our Solar System formed (e.g. Campbell, 1916; Aitken, 1926). Pluto was discovered in 1930 by Clyde Tombaugh at Lowell Observatory, and its discovery prompted theoretical and observational research on planetesimals beyond Neptune (review by Davies et al., 2008). Edgeworth (1949) first fully developed the theory of protoplanetary disk formation leaving a remnant, lower density disk of planetesimals beyond Neptune. Kuiper (1951) proposed that these objects were icy bodies, in agreement with the coincident results of Whipple (1950); the coma around the cometary nucleus is the result of sublimating surface ices which are unstable in the inner Solar System. Kuiper (1951) described a belt of objects extending from $38 - 50$ AU, which he believed to be sufficiently large to produce all of the observed comets, produced by a combination of perturbations by Pluto and passing stars. Edgeworth (1961) speculated that these 'gravel' bodies would resemble comets if perturbed into close approaches to the Sun. As a result of the significant contributions of Edgeworth and Kuiper, the trans-Neptunian objects are sometimes referred to as the Edgeworth-Kuiper belt, or Kuiper belt (as suggested by Duncan et al., 1988).

The possibility of a large population of objects in the outer Solar System was further explored over the following decades. Whipple (1964) modeled the Kuiper belt as a ring of icy bodies between $40 - 50$ AU with a total mass of $10 - 20 M_{\oplus}$. A ring of this density, however, would be expected to induce gravitational effects on the orbits of known comets, and these were not observed (Hamid et al., 1968). The ring of icy bodies, however, provided a plausible source for the short period comets. More complex analysis was made possible by the advances in computational capacity. Fernandez (1980) demonstrated that modification of Oort cloud object orbits into Jupiter family comet orbits was much too inefficient to create this population, and he postulated the source of the short period comets was a ring of icy bodies between $35 - 50$ AU from the sun, similar to that proposed by Whipple (1964). Fernandez (1980) also postulated that the comets were sent into their planet crossing orbits as a result of gravitational encounters with large planetesimals in the belt. Fernandez & Ip (1981) used numerical methods to accrete the giant planets and scatter bodies into a cometary reservoir, and tracked their returns as cometary objects. Duncan et al. (1988) showed low inclinations of Jupiter family comets indicate they originate in the Kuiper belt. The precise mechanism for transitioning objects from the trans-Neptunian region into comets is still debated, however the most likely source is TNOs (Duncan & Levison, 1997) whose semi-major axes are currently evolving because of

perturbations from Neptune (referred to as 'scattering' objects).

Quite a few survey efforts have targeted the Kuiper belt; early surveys focused on object discovery. The first survey, by Kowal (1989), taken on astrometric plates at the 122-cm Schmidt telescope at Palomar Observatory, covered 6,400 square degrees of sky, primarily near the ecliptic plane. Moving objects were identified by manually blinking the plates to see if objects moved between the images. The survey depth was $m_V \sim 20 - 21$, depending on the object rates of motion. Though this survey did not discover any objects beyond Neptune, it found several comets and was the first to discover a Centaur; 2060 Chiron has a semi-major axis of 13.7 AU, between Saturn and Uranus (Kowal et al., 1979). Another survey attempt was made by Luu & Jewitt (1988) using telescopes at several sites, with sizes $0.6 - 1.3$ meters. Their survey covered 297 square degrees to $m_V \sim 20$ as well as a 0.34 square degree field to a depth of $m_R \sim 24$. Levison & Duncan (1989) surveyed 4.5 square degrees near the ecliptic plane, using the USNO 40-inch telescope and CCD imaging; this resulted in a limiting magnitude of $m_V = 22.5$. They used an automated searching pipeline, and found nothing with a rate of motion expected for objects beyond 25 AU. A few additional surveys were executed, but their unsuccessful results were not published after the first TNO was discovered.

The first TNO (after Pluto) was discovered by Jewitt & Luu (1993). This object, 15760[1], was discovered as part of a survey on the University of Hawaii 2.2 meter telescope on Mauna Kea. It was found to have a semi-major axis of $\sim$ 41 AU, securely beyond Neptune's orbit. This survey also discovered three additional TNOs. After the first successful surveys, the detection rate increased dramatically, and as of November 2015, the Minor Planet Center lists 1,449 discoveries, ranging from objects with giant planet crossing orbits to TNOs with perihelions (q) beyond 70 AU. A complete discussion of recent surveys is available in Bannister (2016).

Recent major surveys are considerably more successful at TNO detection for several reasons. The sensitivity of CCDs and throughput of filters, particularly in the $\sim r$ band filter where TNOs are brightest, have increased dramatically. Survey design has evolved to attempt to optimize both survey depth and area. Moving object identification has also advanced significantly, and is typically done by a moving object

[1]Object names are assigned through the Minor Planet Center, where discoveries are reported. Provisional designations are assigned to discoveries based on the year, the half-month of discovery, and the number of objects previously discovered in that time period. When the object has been observed for four or more years, it may receive a permanent numerical designation. At this point, names can be suggested for the object, however many objects have only a numerical designation.

detection software, sometimes with verification by a human operator. As a result, a number of surveys are now moving from the 'object collection' mode into characterized detections, where the survey depth and efficiency are carefully measured.

The Deep Ecliptic Survey (DES, Adams et al., 2014) discovered hundreds of TNOs from 1998-2005. This included 304 objects with well determined orbits, that were dynamically classified (details on classification are given in the next section). The search fields used to discover the objects were recorded, and this was used to calculate the probability of detecting objects on a particular orbit in each field. By assessing the probability of detections across all survey fields, the DES was able to provide a debiased estimate of the TNO populations. This process is complicated by the interdependence of many parameters which influence detectability. However, the DES provided distributions of several orbital parameters for TNOs in three different dynamical classifications.

The Canada-France Ecliptic Plane Survey (CFEPS, Jones et al., 2006; Kavelaars et al., 2009; Petit et al., 2011, 2014) covered a total of 701 square degrees, with discoveries from 2003-2009. Approximately half of the survey was centered off the ecliptic plane, which provides a lever arm for determining the extent of the inclination distributions as well as an increased sensitivity to objects from large inclination populations, which spend little time near the ecliptic plane. This survey, with a limiting magnitude of $g \sim 23.5 - 24.4$, discovered 190 characterized TNOs. The characterized objects are above the 40% detection efficiency threshold; characterized objects can be used to model the intrinsic population. The CFEPS survey team calculated the acceptable orbital parameter ranges to describe TNOs from the populations detected in the ecliptic portion of CFEPS, and released these results as the 'L7 model' (Petit et al., 2011).

Based on the success of CFEPS, the Outer Solar System Origins Survey (OSSOS, Bannister et al., 2016) began on the Canada-France-Hawaii Telescope in 2013, aiming to provide a large, fully characterized sample of TNOs with high-precision orbits. This requires extensive time for TNO followup, to ensure that objects are properly tracked and not 'lost'. OSSOS is targeting resonant populations, objects with integer period ratios to Neptune's (see Section 1.3 for details) as one of its primary science goals. OSSOS will provide detailed descriptions of many of the well populated resonances in the Kuiper belt (Volk et al., 2016). This survey is still ongoing.

Trujillo & Sheppard (2014) are currently performing a survey searching for objects beyond 50 AU. They are using the DECam imager on the 4 meter CTIO telescope

and have identified hundreds of TNOs. However, this survey only tracks objects which appear to be beyond 50 AU. To date, they have discovered 2 objects with large perihelia, including 2012 VP_{113} with a perihelion of 80 AU. These high perihelion objects provide an interesting puzzle of emplacement; their current orbits are largely unaffected by Neptune, but objects are extremely unlikely to have formed at these large distances.

With the rise of large surveys intended to probe the intrinsic population, it becomes increasingly necessary to employ useful subclassifications for TNOs. Based on the large number of discoveries, there are clearly several dynamical subgroups of TNOs. Understanding the characteristics of these different subgroups is necessary to unravel the formation and evolutionary history of the Kuiper belt.

1.2 Dynamical Classifications

The orbit of one object around another can be uniquely defined in several different parameter spaces using seven different parameters. For numerical simulations, the typical input is the position and velocity in cartesian space: x, y, z, dx/dt, dy/dt, dz/dt at some epoch, ε. (The epoch is what determines the positions of any other objects relative to the orbit.) This cartesian space, while useful numerically, gives little intuitive understanding of the characteristics of the object's orbit.

Theoretical work and object orbital fitting typically parameterize the orbit of an object as an ellipse. An epoch, ε, is the date that the specific location is valid for. The shape of the ellipse is defined by the semi-major axis, a, half the long axis of the ellipse, and the eccentricity, e, which describes how non-circular the orbit is (see Figure 1.2). A commonly used and dynamically informative quantity, is the pericenter q of an orbit; the point of closest approach: $q = a \times (1-e)$. To describe the orientation of this ellipse, a reference plane and a reference direction, γ, are used. For the Solar System, orbits are given with reference to the ecliptic (Earth-Sun) plane and the first point of Aries, the vernal equinox, when the ecliptic plane and equatorial plane of the Earth align. The inclination of the orbit, i, is the angle between the ellipse and the reference plane. This is measured at the ascending node, where the orbit of the object passes northward through the reference plane. The angle between the reference direction and the ascending node is the longitude of the ascending node, Ω. The intersection between the reference plane and the orbital plane of the object is the line of nodes, and the angle ω between the line of nodes and the point of

closest approach, or periapsis, is referred to as the argument of periapsis. For the Solar System, closest approach is called perihelion and the angle is the argument of perihelion. The mean anomaly of the object, $\mathcal{M}$, is measured from pericenter and gives the position an object would have in orbit at the specific epoch if the orbital velocity was constant. These parameters (a, e, i, Ω, ω, $\mathcal{M}$, ε) can be used to classify TNOs into dynamically meaningful subpopulations.

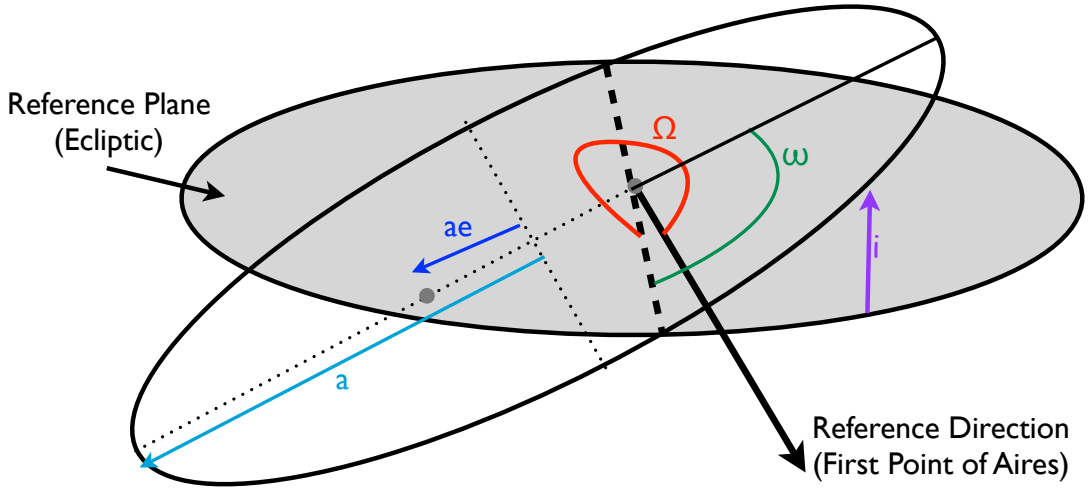

Figure 1.2 This is a representation of the orbital elements used to describe an object's orbit. The semi-major axis, a, indicates the distance and the eccentricity, e, represents the non-circularity of the orbit. The argument of pericenter, ω, is the angle between the pericenter location and the line of nodes (where the orbit crosses the reference plane). The longitude of the ascending node, Ω, is the angle between the reference direction and the ascending portion of the line of nodes. The mean anomaly, $\mathcal{M}$, is the angle representing the object's position along its orbit relative to its pericenter location.

The wide range of dynamical behaviors exhibited by TNOs was unpredicted by theories of the Kuiper belt, and requires a more complex interpretation of the history of the outer Solar System. The dynamical structure of the trans-Neptunian region has been sculpted by the dynamical evolution of the giant planets, imprinting a signature on the orbital distribution of TNOs. The trans-Neptunian region is much more dynamically excited than the asteroid belt; the TNOs are at higher average inclinations and eccentricities. In Figure 1.3, the known outer Solar System objects

show significant structure and large inclinations and eccentricities. TNO orbits also have a wide range of stability timescales; some are stable for the age of the Solar System ($\sim$ 4.5 billion years), and others evolve on million year timescales (Levison & Duncan, 1993; Holman & Wisdom, 1993). TNOs are classified into subpopulations based on their dynamical behavior as a first step toward unraveling their evolutionary histories.

The region between 42 and 48 AU contains the cold classical Kuiper belt. Recent work indicates that the cold classical Kuiper belt may consist of multiple components (Petit et al., 2011; Bannister et al., 2016); dynamical simulations can produce both populations simultaneously by combining multiple periods of different planetary migration rates for Neptune (Nesvorný, 2015b). The two components are the 'stirred' objects, which span a larger a range and slightly hotter eccentricities, and the 'kernel', which is a dense region of very low-e and low-i objects (Petit et al., 2011). The kernel is the densest population in the trans-Neptunian region, and most resembles the theoretically predicted Kuiper belt. Both the stirred and kernel objects are dynamically cold, with low eccentricities ($e < 0.1$) and low inclinations ($i \lesssim 7°$). The cold classical TNOs have different properties than the rest of the TNOs, and may represent the only population which formed in situ. This population includes a significant number of binary objects, two TNOs which orbit their common center of mass. The binary fraction of the cold classical TNOs is higher than any other component, and includes many widely separated binaries (Noll et al., 2008). The cold classical objects have a different size distribution (Petit et al., 2011) as well as a different surface color distribution (Tegler et al., 2003) and albedo distribution (Vilenius et al., 2012). The homogeneity of surface properties and binary fraction between the kernel and stirred populations has not yet been explored. The cold classical objects are contaminated by the overlap of their distribution with the hot classical objects.

The hot main classical belt is found between 42 and 48 AU and has more excited ('hotter') eccentricity and inclination distributions. The hot classical objects overlap in same semi-major axis space as the cold classical belt, and the low eccentricity and inclination tail of the hot distribution is difficult to disentangle from the cold distribution. Dynamically excited objects are also found interior to the cold classical TNOs, with stable semi-major axes, $a < 42$, a region referred to as the inner classical belt (Gladman et al., 2008). The outer classical belt, with $a > 48.4$ AU and $e < 0.24$, is modeled to extend outward (at decreasing densities) to hundreds of AU, however few objects are known in this region due to their low detectability.

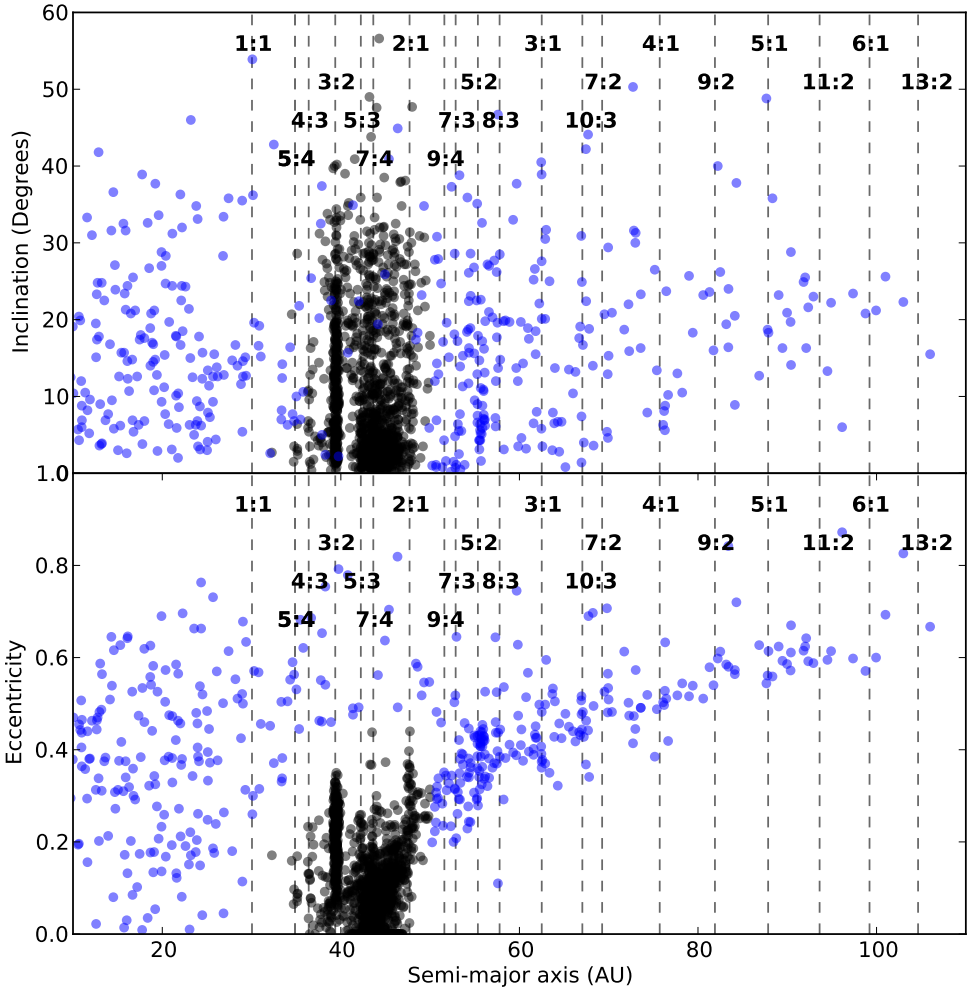

Figure 1.3 These are the objects in the outer Solar System reported in the minor planet center. The black circles indicate objects classified as trans-Neptunian objects, and the blue are reported as 'Centaurs and Scattered Disk' objects. The core of the classical belt is apparent, as well as some of the resonances in the Kuiper belt region. The numbers mark the semi-major axis locations of mean motion resonances with Neptune. (A small number of discoveries were truncated from this plot to show the structure in this range; those objects have larger inclinations or semi-major axes.)

The Centaurs are found inward of the classical belt, between the giant planets. These objects do not cross Jupiter's orbit, and are thus not Jupiter family comets,

but may be a source for these comets. They have semi-major axes $a < a_{Neptune}$, so they are strongly gravitationally influenced by the giant planets. The orbits of the Centaurs are not long term stable and evolve on relatively short timescales.

The Centaurs are essentially an extension of the scattering TNOs inward of Neptune's orbit. 'Scattering' is used to refer to TNOs which are currently scattering because of interactions with Neptune (Gladman et al., 2008). Some of the TNO literature refers to a 'scattered disk', intended to indicate objects which were scattered by Neptune at some time (e.g. Duncan & Levison, 1997), however in practice this classification is ambiguous to apply to real objects because it depends on knowledge of the object's history. The 'scattered disk' classification is often used in dynamical simulations and includes 'scattering' objects as well as hot classicals and sometimes resonant objects. In this work the 'scattering' classification is used, which only depends on the current state of the object's orbit. To be classified as scattering, a TNO must exhibit a change in semi-major axis of > 1.5 AU over a 10 million year orbital integration. This indicates the orbit of the object is currently evolving as a result of interactions with Neptune.

The detached TNOs have pericenters which have decoupled from Neptune (Gladman et al., 2008). This classification is meant to identify TNOs with long term stable orbits, neither affected by Neptune nor distant enough for forces such as galactic tides to influence them. A semi-major axis beyond the main classical Kuiper belt and an eccentricity limit of $e \gtrsim 0.24$ are used for classification (Gladman et al., 2008).

In order to be classified as a hot or cold classical object, Centaur, scattering object, or detached object, the TNO must not be in resonance with Neptune. Resonant TNOs have an integer period ratio with Neptune. The classic example is Pluto, in 3:2 resonance with Neptune. Pluto completes two orbits in the time Neptune completes three. This orbit commensurability provides phase protection for the object, so resonant objects can remain stable in a wider range of eccentricities and inclinations than non-resonant objects at similar semi-major axes as discussed in more detail in Section 1.3.

1.3 Resonant Objects

Resonant objects are dynamically linked; an object in resonance explores a limited phase space relative to the other body. A measure of the relative positions via angular phase of the objects is the resonant angle, ϕ. For resonant objects, the resonant

angle of the objects oscillates over time instead of circulating through a full 360°. The change in this angle can only be measured through forward dynamical integration. Simulation test particles have orbits which are known to arbitrary precision, so these objects are simple to numerically integrate. However, the orbits of real objects are calculated based on their measured positions in the sky; this process has an associated uncertainty. To determine the behavior of a real object over time, one must determine the range of orbital parameters which are within the orbit calculation uncertainty. Integrating several representative clones of the object ensures that the uncertainty in the orbit determination is propagated into the classification. For objects with short arcs of measured position, it is common for clones to display different evolutionary behavior, especially if the object is near a resonance boundary. There are multiple methods for estimating orbital uncertainty, including using the covariance matrix of a fit to the orbit parameters (assuming Guassian and uncorrelated astronomic uncertainty; Bernstein & Khushalani, 2000), searching for the largest and smallest semi-major axes orbital solutions consistent with the astrometry (Gladman et al., 2008), and resampling the astrometric measurements and recalculating additional orbital fits (Pike et al., 2015). Once the evolution of the object is numerically integrated, the resonant angle is analyzed.

The resonant angle is an expression of the distance between the two objects of interest. It is a function of the mean longitude, λ, and the longitude of perihelion ϖ, defined in equations 1.1 and 1.3. The ratio of periods is expressed as p:q. The resonant angle is expressed as ϕ, which depends on the mean longitude of the test particle and Neptune, λ and λ_N, the longitude of perihelion of the test particle and Neptune, ϖ and ϖ_N, and the longitude of the ascending node of the test particle and Neptune, Ω and Ω_N.

$$\lambda = \Omega + \omega + \mathcal{M} \tag{1.1}$$

$$\lambda_N = \Omega_N + \omega_N + \mathcal{M}_N \tag{1.2}$$

$$\varpi = \Omega + \omega \tag{1.3}$$

$$\phi = p\lambda - q\lambda_N - m\varpi - n\Omega - r\varpi_N - s\Omega_N \tag{1.4}$$

The only mean motion resonances found to be important in the outer Solar System are the stronger lower order resonances, involving p and q. (The strength of resonances with non-zero r and s depend on Neptune's eccentricity and inclination respectively; resonance strength $\propto e^m e_N^r \sin i^n \sin {i_N}^s$. Resonances involving the larger TNO eccentricity are clearly strongest.) Because $p - q - m - n - r - s = 0$ as a result of rotational invariance, $m = p - q$ and n, r, and s are assumed to be zero in this work (Elliot et al., 2005). The resonant angle for a p:q resonance is referred to as ϕ_{pq}, and the strength of the p:q resonances depends on the eccentricity of the object.

Objects are classified as securely resonant if their resonant angle oscillates for 10^7 years. In both real detections and simulations, unstable resonators are found. These objects spend $< 10^7$ years in resonance and typically transition into scattering or detached objects.

The specifics of the oscillation of the resonant angle, ϕ, provide additional information about the object's orbit. This oscillation of ϕ is referred to as libration. Resonances have different possible stable configurations, depending on the resonance order. The different islands of stability support a range of libration characteristics. The range of amplitudes of the oscillation, or libration amplitudes, depends on the resonance order. Resonant particles can be in the symmetric libration island or one of the two asymmetric libration islands. Figure 1.4 shows a selection of possible resonant behaviors.

In all resonances except the n:1 resonances, all libration is symmetric, meaning the libration center is 180° from Neptune. (The libration center can be approximated by the median of the ϕ values.) The n:1 resonances, such as the 5:1, have both symmetric and asymmetric libration islands. Particles in the 5:1 resonance can have libration centers of 120°, 180°, and 240°. The amplitude of the oscillation, or the libration amplitude, describes how far from the libration center the particle librates. This is half of the maximum to minimum angular libration. The symmetrically librating Plutinos appear to have libration amplitudes of $\sim 20° - 130°$ (Gladman et al., 2012); higher libration amplitudes for the Plutinos are dynamically unstable (Nesvorný & Roig, 2000; Tiscareno & Malhotra, 2009). In the 5:1 resonance, because of the phase space is separated into the different libration islands, the symmetric resonators have libration amplitudes from $\sim 170° - 178°$, and the asymmetric librators have amplitudes of $\sim 30° - 90°$ (Pike et al., 2015). Understanding the range of allowable libration centers and amplitudes is necessary for a population model because of the different observational biases against detection.

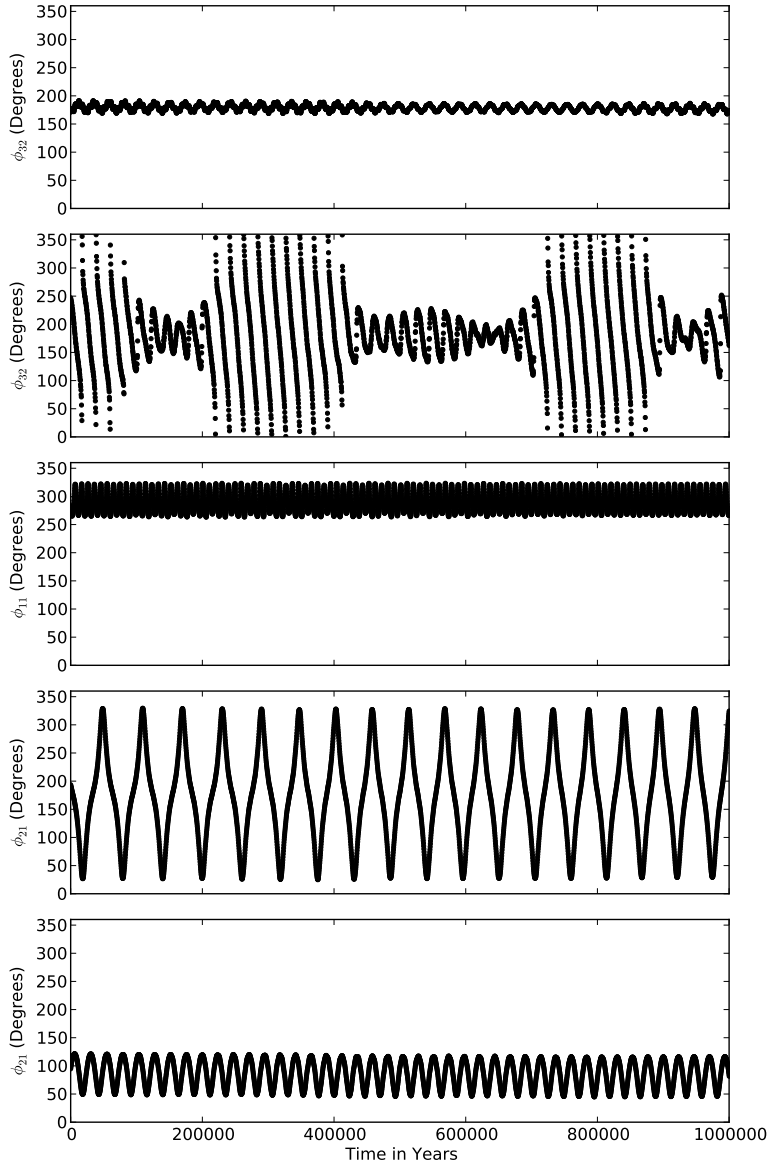

Figure 1.4 The subplots show the time evolution of test particles, selected for their ability to illustrate different resonant oscillation behavior. The upper plot shows a stable 3:2 resonator with a small libration amplitude and a libration center of 180°. The second panel shows a test particle which is sticking in the 3:2 resonance; the test particle's resonant angle circulates before resonating briefly with a resonant amplitude of $\sim 80°$, then circulates (in non-resonant behavior) again. The third panel shows a 1:1 resonator in an asymmetric libration island, L5. The fourth panel shows a high amplitude symmetric librator in the 2:1 resonance, and the bottom panel illustrates a 2:1 resonator in the asymmetric resonant island.

Resonant objects have more complex discovery biases than non-resonant TNOs. Objects are most likely to be detected at pericenter because they are closer and therefore brighter. Resonant objects come to pericenter at specific locations relative to Neptune, so survey longitude is an important factor in discovery. The specific pericenter locations of resonant TNOs depend on their libration island and libration amplitude. As a result, in order to correctly estimate the size of a resonant population it is necessary to know the distribution of libration amplitudes and libration islands, as well as the discovery survey pointings.

The resonant populations in the Solar System include trojans and co-orbitals; these are objects in 1:1 resonance with a planet (a special case of the n:1 resonance). The most familiar trojan population occupies the L4 and L5 Lagrange points of Jupiter's orbit. Trojans have also been found in the 1:1 resonance with Neptune (Chiang et al., 2003) and Uranus (Alexandersen et al., 2013). The Uranian trojan is not long term stable, and the Neptunian trojans include both stable and unstable members (Alexandersen et al., 2013). Co-orbitals are in symmetric libration, and trojan orbits occupy and asymmetric libration islands.

Objects can enter and exit resonances as a result of a multiple dynamical mechanisms. Resonance capture can occur as a result of resonance sweeping or sticking. Resonance sweeping occurs when the slow outward migration of a planet, such as Neptune, causes the resonance locations to migrate slowly outward. This slow migration increases the semi-major axes of small bodies under their influence and causes objects to be deeply captured into the resonance (e.g. Malhotra, 1995). Objects can also enter resonance via resonance sticking; when their unstable orbits happen to cross a resonance they may be captured either temporarily or long-term (e.g. Lykawka & Mukai, 2007b). Objects exit resonances through both resonance dropout and diffusion. Resonance dropout occurs during planetary migration; objects captured into a resonance escape the resonance when the resonance moves too quickly or shrinks too rapidly for their orbits to be sufficiently modified remain resonant. Resonance diffusion is a chaotic evolution of object orbital elements that can result in an object which is not deeply captured leaving the resonance, a common occurrence in particles captured through resonance sticking. These capture and exit mechanisms for resonant TNOs affect their long-term stability.

The dynamical characteristics of TNOs provide insight into their evolutionary history. If the outer Solar System had a quiescent history, it would not have such large resonant populations. The specifics of the objects preserved in resonance also

constrain the specific migration mechanisms that emplaced them. The dynamical properties of the outer Solar System are used to constrain the formation and evolution of the Solar System as a whole.

1.4 Surface Properties

The most basic property of TNO surfaces is object size, however this is difficult to measure accurately. The largest objects, such as Pluto and Eris, can be resolved by Hubble Space Telescope. More accurate measurements of chords across an object can be obtained using occulatations (e.g. Elliot et al., 2007). Most TNO studies use absolute magnitude, H, as a proxy for object size. H-magnitude is the magnitude the object would be if it was located at 1 AU from both the Sun and the observer, with a phase angle (observer–sun angle) of zero degrees. H-magnitude is typically quoted in a particular band, H_r is the r band absolute magnitude. Converting H-magnitude to object size requires knowledge of the object's albedo, or reflectance in the particular band. H-magnitudes are a useful approximation, particularly when objects have similar albedos.

The TNOs in the outer Solar System are expected to be comprised of some of the most unprocessed material from the solar nebula. Some of these bodies have been shown to have volatile ices on their surfaces (e.g. Brown, 2002; Barucci et al., 2005; Trujillo et al., 2005, 2011; Brown et al., 2012). These volatile ices are not stable in the inner Solar System. In spite of likely processing due to solar wind and collisions, TNOs may provide the least altered samples of the solar nebula available. Understanding the composition of the outer Solar System provides insight about the primordial disk from which the planets formed.

The brightest outer Solar System objects have been studied spectroscopically. This includes primarily Centaurs and the largest TNOs. In the visible wavelengths, TNO spectra generally shows a large gradient from neutral to red, which is often interpreted as a signature of organics (Barucci et al., 2008), see the 'tholin' in Figure 1.5 for an example. Absorption features that result from aqueous alteration of surface materials have also been identified on several objects; broad absorption features were identified on several Plutinos (e.g. Lazzarin et al., 2003; Fornasier et al., 2004) and a Centaur (Jewitt & Luu, 2001). However, their detections could not be confirmed in followup observations, perhaps as a result of a rotating non-uniform surface distribution. Most ices expected in the outer Solar System (methane, nitrogen, water,

ammonia (NH_3), and CH_3OH) have absorption features in the near-infrared. Spectra of water and methane ices are presented in Figure 1.5. Some Centaurs and TNOs have spectra with ice features, while others have featureless spectra (Jewitt & Luu, 2001). Approximately 40 distant objects have been observed spectroscopically, in either optical, near-infrared, or both, and about half of them have detections of some kind of ice (Barucci et al., 2008). Many of the objects with obvious volatile detections, e.g. methane on Eris, are too large to be representative of the possible surfaces of the majority of detected TNOs. Smaller TNOs do not have sufficient surface gravity to prevent volatile escape (Brown, 2012).

The majority of TNOs can only be studied (with a realistic telescope time investment) photometrically. The only uncontroversial detected feature in TNO optical spectra is the spectral gradient, and this can be inferred using photometry. The spectral gradient in visible wavelengths can be used to identify Haumea family members (Brown et al., 2007). The Haumea family is the only known TNO collisional family; objects in this family have similar inclinations, eccentricities, and semi-major axes as well as similar surface colors. These objects are likely the remnants of a past collisional event which disrupted a large object. Because these family members have similar orbital parameters, identifying family members with photometry provides constraints on TNO evolution.

Several large photometric studies have identified trends in the TNO color distributions. Tegler et al. (2003) identified a bimodality in the $B - R$ colors of high inclination TNOs and different colors for the cold classical TNOs. A bimodality in the color distribution of Centaurs has been confirmed by several surveys (e.g. Tegler et al., 2003; Peixinho et al., 2003). However, this bimodality may be the result of a relationship between color and TNO size (Fraser & Brown, 2012; Peixinho et al., 2012), manifesting as a classification based dependence because of the biases toward discovering small objects with closer orbits. Most photometric surveys of TNOs are conducted in the optical, however Trujillo et al. (2011) designed custom filters for instruments on Gemini and Magellan observatories which targeted ice absorption bands in the near-infrared. By observing continuum near-infrared bands as well as filters targeting methane and water ice absorption, they were able to identify Haumea family members based on the inclusion of water ice and determined that only the largest TNOs have methane ice on their surfaces. Photometry of TNOs has revealed a wide range of surface properties.

The majority of TNO surface studies have focused on determining the surface

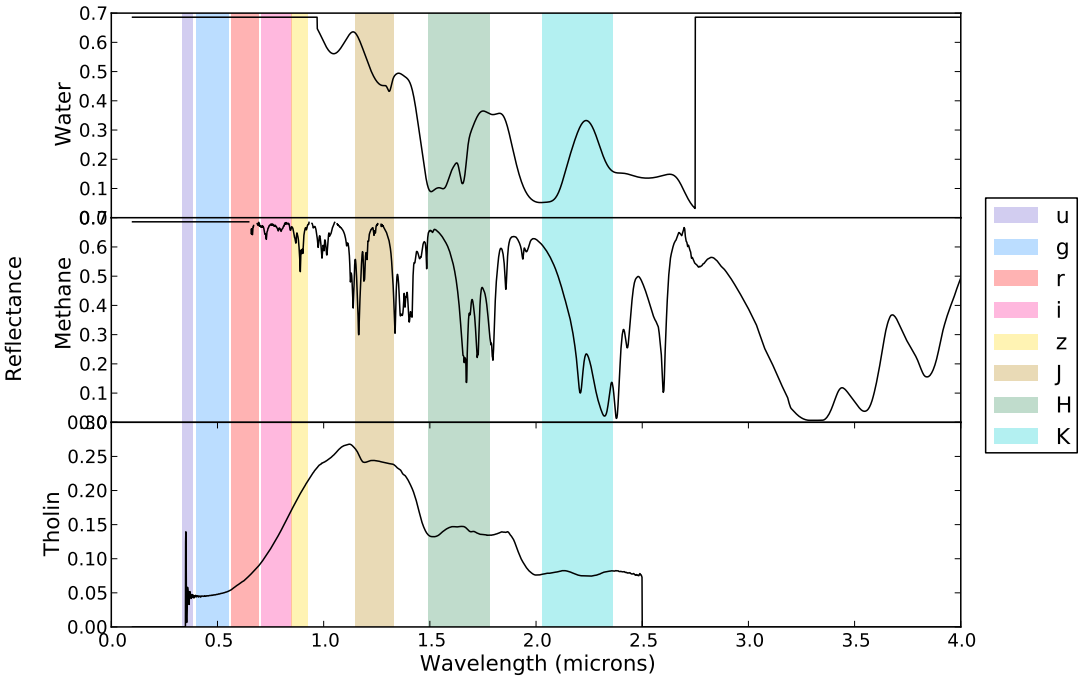

Figure 1.5 These reflectance spectra show the measurements that would result from different surface materials on a TNO, based on laboratory work. The water ice is crystalline, with a grain size of 100 microns; both methane and water are at 60K, a typical temperature in the outer Solar System. The methane and water ice spectra are based on Mastrapa (2010). The 'tholin' is a laboratory material based on organic compounds which have been irradiated. Tholins provide an appropriate spectra for some distant small bodies, such as Titan. Roush & Dalton (2004) reported spectra of these materials at temperatures corresponding to TNO distances; this is presented here. The increasing reflectance of tholins and similar materials at smaller wavelength is frequently measured as a positive $g - r$ color. The shaded panels represent different filter bandpasses; from left to right the filters are u, g, r, i, z, J, H, and K. These filters are from the Near-Infrared Imager and Spectrometer (NIRI) and the Gemini Multi-Object Spectrometer (GMOS). The longer wavelengths, H and K, are clearly sensitive to ice absorption, however the majority of TNOs are too faint for observations in these wavelengths.

properties of individual objects, instead of a carefully selected representative sample of the region. This is primarily a result of the available sample for followup, however, in the era of large discovery surveys it is now possible to determine the composition of the Kuiper belt as a whole.

1.5 Beyond the Solar System

TNOs in the outer Solar System are the remnants of planet formation; they preserve information about the composition and structure of the Sun's protoplanetary disk. At this age in our Sun's evolution, collisionally produced dust in the Kuiper belt region is not detectable from Earth. However, dust is detected around other stars, often in the form of debris disks. These debris disks are found around $\sim 15\%$ of main sequence stars, and the specifics of the disk structures provide information about the planet formation process (Wyatt et al., 2003).

Dust around other stars is detected as an excess of infrared emission. The spectral energy distribution of the star is fitted with multiple black body profiles, and the lower temperature component is attributed to dust. Dust around a star has a short lifetime, as a result of Poynting-Robertson drag which causes the dust to spiral inwards into the sun, so large amounts of excess dust around a star must be regularly replenished. The source of dust is inferred to be collisional grinding of larger planetesimals, therefore the presence of dust is indicative of planet formation.

Debris disk studies can suggest or reveal the presence of planetary mass objects. Resolved images of debris disks show symmetric and asymmetric structures. The early resolved images include HR4796, a disk around a 10 Myr-old A0V star (Wyatt et al., 2003). The disk is edge on, and appears as a double lobe structure, with one lobe $\sim 5\%$ brighter than the other. A possible explanation for this asymmetry is the presence of a planet on an eccentric orbit (Wyatt et al., 1999).

The characteristics of debris disks can also provide insight into the process of planet formation. Another object that has been studied extensively is Fomalhaut, a 200 Myr-old A3V star (Wyatt et al., 2003). Based on multi-wavelength observations, Wyatt & Dent (2002) calculated the size distribution of dust grains, and determined the dust was being produced from a collisional cascade beginning with planetesimals several kilometers in size. Observations in the optical confirmed the dust ring, and calculated that the ring was eccentric, with the star at one focus – a signature of planetary sculpting (Kalas et al., 2005). By comparing their optical images to previous sub-millimeter observations, they also calculated that the dust in Fomalhaut's ring is optically dark. A bright spot in the Fomalhaut images, visible in the optical in multiple visits, has generated considerable speculation. At discovery, the planet candidate (bright spot) was slightly interior to the eccentric dust ring, and appeared to be on an orbit tracing the inner edge of the disk (Kalas et al., 2008). However,

later observations determined that the candidate's orbit is too eccentric, and would cross the region of the disk (Kalas et al., 2013; Beust et al., 2014). The lack of signal in the infrared wavelengths at the planet candidate's position (Marengo et al., 2009; Janson et al., 2012) casts doubt on whether this object can be a planet; at the very least this object must be less massive than Jupiter. Alternate theories for the bright spot include a dust cloud resulting from a recent collision (Lawler et al., 2015). Unfortunately, the existence of planets in this system remains an open question. However, systems such as Fomalhaut provide an environment in which to study planet formation and provide context for the objects in our Solar System.

The recent images of the HL Tau protoplanetary disk display a dramatic structure of dense, dusty regions and lower density gaps (ALMA Partnership et al., 2015). The bright rings are optically thick, but the dark rings do include material with emissivity consistent with grain growth. Some of the dark rings in HL Tau are likely the result of planet formation. The HL Tau rings are not entirely circular; they are found to be eccentric with HL Tau at a focus, and the larger eccentricity rings are at larger semi-major axis. Eccentric rings suggest a shepherding proto-planet. The most compelling evidence for planetary bodies in some of the HL Tau ring gaps, however, is the associated smaller ring gaps at mean motion resonance orbits (ALMA Partnership et al., 2015). The effects of resonances in planetary formation and evolution has consequences for the formation of our own Kuiper belt. The HL Tau system includes significantly more dust than our Kuiper belt, but observing this stage of planetary formation and growth provides insight into understanding our own Solar System and remnant disk.

1.6 Looking Forward

Our understanding of the trans-Neptunian region has evolved rapidly since the discovery of the first TNOs in surveys. Several major observational approaches will dominate the next decade of TNO science: large scale surveys and the New Horizons space mission. The New Horizons mission is providing unprecedented detail about the surface processes of Pluto and its moons, and (if the extended mission is approved) it will also visit another TNO. The large scale surveys such as the Large Synoptic Survey Telescope (LSST) will provide a flux limited sample of TNOs an order of magnitude larger than any survey to date. As many of the surface absorption features are in the near infrared, the James Web Space Telescope (JWST) will provide an optimal

resource for investigating the composition of these new discoveries.

On 14 July 2015, the New Horizons spacecraft made its closest approach to the Pluto system (Stern et al., 2015). The spacecraft captured pictures of Pluto and its moons Charon, Nix, Hydra, and Styx. Because of the large number of images and the slow data transfer rate, Pluto encounter data will be downloading from New Horizons until late 2016. The images received to date, however, are already surprising. Pluto's surface hosts a range of unexpected geological features and evidence of surface modification, including the very large level plane and mountains with heights of two to three kilometers. The mountain features are likely water ice, as the other ices which dominate Pluto's surface do not have sufficient material strength to create these features. There are craters with bright ice deposits and craters which have degraded. The surface color of Pluto varies considerably over its surface, and the abundances of different surface ices (CO, CH_4) correlate with different surface features. The images of the moons reveal a significantly darker Charon and the irregular shapes of the small moons. The extensive imaging of the Pluto system provides an unprecedented amount of information about the unexpectedly active surface and the variety of topographical features which will require years of research.

The New Horizons spacecraft team has been approved for an extended mission to flyby another TNO. Three potential targets were found within the possible maneuvering space of New Horizons (Stern, 2016). These targets are approximately $20 - 55$ kilometers across, and New Horizons has made the course adjustment necessary to encounter potential target 1. The flyby of potential target 1 will have imaging at 90 meter surface resolution (Kavelaars, 2016). New Horizons will provide images of what is likely a cold classical TNO, the most likely dynamical classification to have formed in situ. These data may provide us with the composition of this object's surface and clues to the proto-planetary disk composition, and the number of surface craters will constrain the impact history in this region.

LSST is an 8.4 meter telescope to be built in Cerro Pachon, Chile. The camera will have a 9.6 square degree field of view and six filters, *ugrizy* (Ivezic et al., 2008). The precise survey cadence is still under intense review, however LSST will survey the visible sky ($\sim 30,000$ square degrees) down to a magnitude of $m_R \gtrsim 24$ with repeated visits. This survey is optimal for discovering transient objects, including moving objects such as TNOs, and will reach a depth at least a magnitude beyond the previous large sky survey by Trujillo & Brown (2003). One of the four main science goals of the survey telescope is Solar System object discovery (Ivezic et al.,

2008). This will include near Earth asteroids, asteroids, comets, Centaurs, and trans-Neptunian objects, and is expected to increase the currently known sample of these objects by one to two orders of magnitude. After several years of operation, LSST will provide a complete list of TNOs brighter than the limiting magnitude with its survey field; the TNO detections will be characterized and will be used for statistical studies of the Kuiper belt. The LSST team is currently building a detection pipeline to link moving objects detected in different nights, with the goal of having analysis software fully functional before science operations begin in 2023 (LSST Corporation, 2016).

JWST is a 6.6 meter telescope that will be launched in October 2018 (JWST Collaboration, 2016). JWST will travel to the L2 Lagrange point of Earth's orbit. The telescope is a collaboration of the National Aeronautics and Space Administration, the European Space Agency, and the Canadian Space Agency. JWST is infrared optimized, with a near-infrared camera and a near-infrared multi-object spectrograph (Gardner et al., 2006). A near-infrared imager on a 6.6 meter telescope without atmospheric absorption and background radiation will be able to measure the near-infrared colors of an unprecedented number of TNOs; the TNOs brighter than the limit of $m_K \sim 20$ will increase the observable sample by a factor of ~ 100 over the currently feasible sample (Trujillo, 2008). JWST will also be able to detect complex organics on TNO surfaces (Parker et al., 2016). The near-infrared region of TNOs can exhibit ice absorption, from water and nitrogen surface ice, and JWST will be able to measure the fraction of the outer Solar System objects that harbor these ices.

Future studies of TNOs will benefit both from large scale discovery surveys and from additional resources more sensitive to surface features. The surface properties of Pluto and its moons and possibly the additional flyby target, will provide reference for interpretation of different measured TNO surfaces. Our current research understanding the underlying TNO distributions in the outer Solar System provides testable predictions for these projects, particularly LSST.

Chapter 2

Methods

A variety of analysis techniques were used in this work. I focused on understanding the effect of measurement uncertainties in astrometry and photometry. I approached much of the analysis from a forward modeling perspective; I created a model, biased that model in the same way as my observational data, then compared the biased model to the real observations using a statistical test. The methods and tools I used are described here.

2.1 Characterization Using a Survey Simulator

The discovery method used for TNOs significantly impacts the measured sample, and understanding these biases is crucial to modeling the underlying TNO distribution. Early TNO discovery surveys focused on discovering large numbers of TNOs or TNOs of a particular dynamical type. Surveys also typically focus on the ecliptic plane, in order to maximize object detections. The survey pointings affect which dynamical groups of objects the survey is likely to discover, for example resonant TNOs come to pericenter at restricted sky locations relative to Neptune. This means that the discovery of resonant TNOs, unlike non-resonant populations, depends on the survey latitude. The survey depth combined with the different absolute magnitude distributions of TNO classes results in varying fractions of TNO sub-population discoveries. Objects are typically discovered because of their motion relative to background stars, so the survey discovery cadence and exposure time will result in a survey sensitive to specific projected rates of motion in the images. In addition, the orbital prediction methods project future object positions based on discovery observations that span a

tiny fraction of the object's orbit and must make assumptions about the orbit so that the formal uncertainties in the ephemeris location (given the assumptions are correct) are small enough to be useful. These assumptions can affect tracking efficiencies, for example assuming a circular orbit can result in a preferential loss of non-circular orbits in followup. All of these observational effects contribute to the significant sample biases in the known TNO population.

To mitigate the effects of survey biases in our analysis I make use of the Canada-France Ecliptic Plane Survey (CFEPS) survey simulator (Kavelaars et al., 2009; Petit et al., 2011). (See Sections 3.5.1, 4.4.1, and 5.4.1 for examples.) Using a survey with known discovery biases allows the study of the underlying TNO population (Jones et al., 2010). This survey simulator takes input files containing the pointings and size of the survey discovery blocks, the filling fraction (not 100% because of chip gaps), the time of those observations, the limiting magnitude, the tracking efficiency, and the detection efficiency (which depends on magnitude and rate of motion). The limiting magnitude was determined for the different surveys by the survey teams (Kavelaars et al., 2009; Petit et al., 2011, 2014; Alexandersen et al., 2016) implanting fake objects into the images. The moving object detection pipeline identified possible sources, and these sources were verified by a human operator. The characteristics of the detection and tracking process form the inputs into the survey simulator.

To understand the underlying TNO populations, I first create parametric models of the populations. The models are created based on theoretical orbital element distributions for each component of the Kuiper belt. Each model consists of a 'list' of synthetic orbits or a program that generates orbits based on a distribution of orbital elements. These model orbits combined with an object absolute magnitude and color distribution represent the intrinsic population of TNOs.

The CFEPS survey simulator is used to bias my parametric models to allow me to compare the 'intrinsic' model with the 'observed' population. I supply the survey simulator with model objects, one at a time, and the simulator determines if the input survey fields would have detected the object. Model objects are supplied until the survey simulator detects the number of objects requested by the user. The goals of this process are comparing the orbital distribution of the synthetic detections to the real detections and determining a model dependent estimate of the number of TNOs in the sub-population being modeled. The orbital element distributions of the synthetic detections (e.g. the inclination distribution) can be compared with the detected objects using a statistical test (see Section 2.5). When the input model distribution

is based on a parametric distribution function, then a range of parameter values (e.g. inclination width) can be given as model input, and the statistical acceptability of the 'observed' model is used to constrain the parameters of the input model. To determine a population estimate, the survey simulator is run on a model until the simulator produces the number of detections found in the actual survey. The number of input model objects that is required to generate the correct number of synthetic detections is the population estimate. The randomized model input process is repeated until a median population estimate and 2σ confidence intervals are determined. The survey simulator replicates the biases of the discovery surveys, allowing one to determine a constrained model for the intrinsic population derived from the observed population.

2.2 Forward Integrations with SWIFT

In this thesis I use numerical integrations to investigate the current and future orbits of TNOs in the outer Solar System and to investigate models of planetary migration. I use an integrator to calculate the evolution of test particles and massive bodies over a range of timescales, from short classification integrations to the age of the Solar System (4.5 Gyr). For examples of these applications, see Sections 3.4.2 and **??**.

The orbits of Solar System objects are approximated as Keplerian motion, but the general problem of 3 or more gravitating objects cannot be calculated analytically. In a two body interaction, the objects have elliptical orbits around the center of mass of the system. However, for $n > 2$ bodies (except in a few severely restricted 3 body cases), a center of mass coordinate transformation does not result in a conversion to the solvable Kepler problem. The practical method of investigating the stability of orbits in an n-body system is using numerical integration to calculate the future positions and velocities of each object based on the motion resulting from short time steps.

In order to explore the dynamical evolution of our near-resonant objects, I used SWIFT Regularized Mixed Variable Symplectic Method (RMVS, Levison & Duncan, 1994). Symplectic integration studies the evolution of trajectories induced by the system's Hamiltonian while preserving phase space volumes (Duncan et al., 1998). SWIFT integrates gravitationally interacting objects by calculating the sum of their Keplerian heliocentric motion and the perturbations at each time-step. The Keplerian term provides motion (along a conic section) and the perturbing term affects the velocity of the particle. If the particle passes within the Hill sphere of a planet (where

this method becomes a poor approximation because the planet's gravity dominates) the Keplerian motion is calculated around the planet and the gravity of the Sun becomes a perturbing force. This method conserves the total orbital energy of the massive bodies in the simulation and has been shown to conserve a massless particle's Jacobi integral of the restricted 3-body problem (Levison & Duncan, 1994).

The SWIFT input is optimized for computational efficiency. SWIFT requires heliocentric coordinates and a unit selection in which G=1 (the gravitational constant); this allows a corresponding choice of $M_{\odot} = 1$, so the period of an object at 1 AU is $2\pi[\tau]$, where τ is a time unit of $1/2\pi$ years. The Hamiltonian for the perturbation depends only on the distances between the bodies, so a heliocentric coordinate system is more computationally efficient. The input parameters for SWIFT included the positions of the planets and test particles at the selected Epoch in x, y, z, dx/dt, dy/dt, dz/dt heliocentric coordinates, which I calculated from their barycentric a, e, i, ω, Ω, T_{peri} (time at pericenter) Keplerian orbital elements (see Section 1.2 for details on orbital elements). The Keplerian motion of the particles is best calculated directly in cartesian coordinates (Wisdom & Holman, 1991). The output of SWIFT consists of a time history of the heliocentric orbital elements, from which barycentric orbits or coordinates can be calculated

A variety of integration timescales and time steps can be used depending on the desired stability information and heliocentric distance of test particles and massive bodies. Integrations over $\sim 10^5 - 10^7$ years are used to investigate the current behavior of objects, useful for understanding short term phenomena. To explore the orbital nature of particular selected TNOs, I conducted long duration (4 Gyr) numerical integrations. Timescales of $\sim$4 Gyr (approximately the age of the Solar System) are used to determine if an object could be primordial, i.e. implanted shortly after planetary system formation, or a recent capture. The mass and locations of the planets as well as the distance of the test particles determines an appropriate time step for the integrations. It is important that the time steps are frequent enough that there are multiple calculations per each planetary orbit. More compact systems (e.g. multiple hot Jupiters/Neptunes) have shorter periods, and thus shorter time steps are required in order to correctly resolve planetary encounters. The distance of the test particles is also important; if the particles are at similar semi-major axes to the planets, a shorter time step provides more accurate results. For the outer Solar System, typical SWIFT integrations include the massive bodies of the Sun, Jupiter, Saturn, Neptune, and Uranus. I tested several time-steps for integrations of TNO

test particles in the Solar System (0.2, 0.05, and 0.5 years), and the results were statistically indistinguishable. The 0.5 year time-step is 22 time steps per Jupiter orbit and 329 per Neptune orbit and is usually appropriate for TNO integrations in the Solar System.

I tested the results of simulations to determine if test particles were resonant. Analyzing numerical simulation results is challenging due to the large quantity of data produced and requires an automated approach. I analyzed subsections of the integration, 'windows', to determine if the objects displayed resonance behavior. If the objects were resonant, I recorded the specifics of the resonance behavior. (For details of how this method was tailored to specific integrations and science objectives, see the Methods sections in Chapters 3 and 4.)

2.3 Color Measurements and Photometry

The surface properties of TNOs are frequently investigated using photometry in visible and near infrared wavelengths. The majority of TNOs are too faint for spectroscopic study, which would provide a higher resolution measurement of the surface reflectivity by wavelength. However, TNOs can be divided into surface types based on observations in filters covering multiple wavelength regions. Acquiring reflectivity measurements in several wavelengths provides a coarse spectrum, which can be indicative of particular surface compositions. Precise photometry requires carefully designed observations and analysis.

2.3.1 Photometry

Photometry is a measurement of the quantity of light received from an object. This is reported in magnitudes, m, a logarithmic value based on the object's flux, $\mathcal{F}$. Larger magnitudes indicate fainter objects.

$$m - m_{ref} = -2.5 \times \log(\mathcal{F}/\mathcal{F}_{ref}) \tag{2.1}$$

The reference system ensures that the magnitude is on the same scale as catalog magnitudes. A difference in magnitudes between two bands is the ratio of the flux in those bands. Some common filter bandpasses for photometry are marked in Figure 1.5, including r and g which approximate red and blue. For wavelength ranges a and b,

$$m_a - m_b = -2.5 \times \log(\mathcal{F}_b/\mathcal{F}_a). \tag{2.2}$$

Therefore, an object with a larger $m_g - m_r$ will appear redder.

TNOs are visible in reflected sunlight, so a neutral surface will appear to have solar colors. The most common color measurement is $B-R$ or the similar $g-r$, which can be used to identify two surface types: neutral and red. Photometric measurements in i seem to correlate strongly with r, and therefore provide little additional information (Sheppard, 2012). However, longer wavelengths such as z and J appear to vary independently and provide additional information about the objects' surfaces, and indicate that more than two surface types are required to describe TNOs (Fraser & Brown, 2012).

Acquiring precision photometry requires a careful calibration. Telescope cameras use CCDs to record the photons received by the instrument. In addition to the science images, flat field images are acquired, typically of the sky during twilight or of a uniform surface within the telescope dome. These twilight or dome flats measure the efficiency of each pixel; the pixel to pixel sensitivity of the CCD can vary. Flat field images are also sensitive to telescope optics, imperfections, and dust in the optical path. Bias images are zero second exposures; these images measure the voltage applied to the bias amplifier in order to improve sensitivity. In order to extract the signal from astronomical objects, the signal from the bias frame is subtracted from both the science images and from the twilight or dome flats. Because the flats measure pixel response, the flats are normalized to an average value of 1 and the science images are divided by the flat field images. This results in a science quality image.

After the basic calibrations are completed, the zero point of the image must be calculated. The zero point, ZP, of the image is the magnitude of an object that produces one count per second and is both camera and telescope dependent. The zero point term is used to shift the instrument magnitude onto a standard photometric system.

$$m = -2.5 \times \log(\mathcal{F}) + ZP \tag{2.3}$$

To calculate the zero point, I measure the flux, $\mathcal{F}$, calculate the magnitude of several reference stars in the frame (preferably at least five), and compare these measured magnitudes to catalog magnitudes. I calculate the offset between my measured magnitudes and the catalog magnitudes, determining the zero point. The choice of standard

catalog is important for the zero point calculation because catalogs have different precision, source density, magnitude ranges, and filter bandpasses. If no catalog contains sufficient overlap with the image sources, a photometric standard field (selected because of the availability of sources) can be observed to calculate the camera zero point, however the accuracy of this method depends on identical sky transparency for both sets of exposures. This requires additional observations as near as possible in time and sky location to the science targets of a field known to have standard stars. The zero point for this frame is calculated using the same method, and then this zero point is applied to the science frames. Proper image calibration is necessary to achieve precise photometric measurements.

Photometry methods are devised in order to maximize the signal to noise ratio (SNR) of the measurement. Measuring the magnitude of a source in an image is done using either aperture photometry or PSF (point spread function) fitting. For aperture photometry, the center of the source is calculated, and the flux within a selected distance from that source is summed. In order to optimize SNR, the flux is calculated for multiple aperture sizes. A small aperture, approximately the size of the Full Width Half Maximum (FWHM) of the source is optimal for calculating the object's center but omits much of the object's flux. A larger aperture contains more of the object's flux, but also has higher noise because of the additional sky background and may also have contamination from other sources. Large aperture measurements of bright, isolated, unsaturated sources have sufficient signal to noise, and therefore less uncertainty, so a magnitude correction can be calculated between the small and large aperture based on these sources (Stetson & Harris, 1988). I use bright sources in the frame to calculate a correction factor between the smaller and larger apertures. Then the correction factor is added to the small aperture TNO flux to give a more accurate photometric measurement than would be found using a large aperture around the TNO.

PSF photometry uses a model of the PSF calculated based on other objects in the frame to calculate the brightness of the target. This technique is not well suited to TNOs because of their motion relative to the stars; TNOs are not expected to have the same PSF as the stationary sources in the image. PSF photometry also relies on a similar PSF throughout (at least) large portions of the image, which may not be the case depending on the telescope optics. PSF photometry has the advantage of modeling the shape of the source, and therefore being able to separate nearby sources which may be too blended for aperture photometry. However, ensuring that targets

are sufficiently unblended for aperture photometry is a far more accurate method for ground-based TNO photometry.

2.3.2 TNO Photometry

There are several complications for measuring the brightness of TNOs. The motion of the objects relative to the background stars results in trailing if the exposure is long enough that the motion of the object is greater than the full width half maximum of sources in the image. This means that there is a maximum exposure time based on an object's rate of motion, so many short exposures are often necessary to obtain sufficient signal. To accurately measure flux, one can track at half the TNO rate of motion so that the stars and TNO have a similar trail, or track the stars and model the TNO motion using a non-circular aperture. Tracking the stars has the advantage of a more precise zero point calculation and astrometric solution. I use an aperture photometry method with a pill-shaped aperture, which stretches the typically circular aperture based on the known rate of motion of the TNO to minimize trailing losses (Fraser et al., 2016). This minimizes the effect of trailing loss on the photometric measurements.

Measuring the brightness of TNOs is also challenging because of their rotational variability. Because TNOs are rotating small bodies, the surface visible to the observer changes over time. Large TNOs have rotation periods of $\lesssim$10 hours, and the majority of rotation periods are 4-8 hours (Benecchi & Sheppard, 2013). Smaller TNOs (less than 100 km) with measured light curves fall in a similar range, $\sim 3 - 10$ hours (Trilling & Bernstein, 2006). The magnitude of the TNO may change by up to $\sim$0.3 magnitudes during a complete rotation period (Benecchi & Sheppard, 2013). Large amplitude light curves are more common for small TNOs, as a result of surface features and object shape. TNOs large enough to be round as a result of self-gravity typically have lower amplitude light curves because changes in magnitude are due to changing albedo across the object or smaller surface features. The possibly large change in object brightness as the TNO rotates means that observations in multiple wavelength ranges must be acquired as nearly simultaneous as possible, or any measured spectral slope may simply be a rotational variation. (If the light curve is known to extreme precision, correcting for rotation between different measurements is possible, however this is not typically feasible at a level of precision that is interesting for compositional studies.) Measuring the spectral slope of reflected light off the surface of TNOs

requires contemporaneous measurements at all wavelengths.

An additional challenge for correctly interpreting TNO magnitudes is the effect of viewing angle, called opposition effect or phase effect. At small phase angles ($\lesssim 2^\circ$) from opposition, small bodies brighten dramatically as a result of reduced surface shadows and coherent backscatter from surface regolith. This effect is more severe for asteroids, which explore a large range of phase angles relative to the Earth because of their closer orbits. TNOs have phase angles typically $< 2^\circ$ and up to $7 - 8^\circ$ for Centaurs (Belskaya et al., 2008). Correcting for phase effects is more important for light curve analysis of magnitude over time; phase effects have not been found to impact simultaneous color measurements (Belskaya et al., 2008).

Precise color measurements of TNOs require properly calibrated photometric images as well as specifically designed observations. Short exposures limit trailing loss and nearly synchronous measurements in multiple filters are necessary to avoid light curve effects. Phase effects can be calculated based on the TNO position. Properly executed photometry of TNOs can reveal their surface properties and shapes.

2.4 Astrometry and Astrometric Uncertainties

Large semi-major axis resonant objects require longer arcs to conclusively classify the objects because the observed arc is a small fraction of the total orbit (Jones et al., 2010). After discovery in Canada-France Ecliptic Plane Survey (CFEPS), some TNOs whose orbits were not well measured were imaged in 2010 and 2011 using Megacam on the 6.5 meter Magellan telescope in Las Campanas Observatory, Chile and in 2012-2013 using the Gemini Multi-Object Spectrograph (GMOS) in imaging mode on the 8.1 meter Gemini North telescope on Mauna Kea, Hawaii, USA. I programed the observations using GMOS to target the TNOs approximately twice per dark run for 1-2 semesters. A cadence of acquiring astrometric measurements a few times per opposition provides sufficient sampling of the object's orbit for more precise orbit determination.

I preprocessed the data using the Gemini package for the Image Reduction and Analysis Facility (IRAF, Tody, 1993). The astrometric science images are calibrated using bias and flat field frames in the same way as photometric frames. (This step is not strictly necessary if the target and stars are high signal to noise, but for lower signal sources a good calibration makes the centroid calculation more accurate.) These centroids determine the calculated position of the TNO, and have an uncertainty of

$\sim$FWHM/SNR. If the typical FWHM is $\sim 1''$, a SNR of 15-20 is necessary to ensure the centroid uncertainty does not dominate the measurement. I measured the positions of the TNO and several reference stars.

In order to measure the position of the TNO on the sky, it is necessary to determine how the celestial coordinates correspond to the pixel locations in the image. Distortions in the optical path can cause variations in the image, so the Right Ascension and Declination on the sky may correspond to the image in a slightly non-linear manner. This Right Ascension and Declination fit is referred to as a plate solution. Because we are also projecting the sky to be flat, the plate solution is most accurate over a small area, where the deviation of the projected tangent plane from the spherical sky is small compared to the uncertainties in the plate solution. I selected stars with known positions close to the TNO, preferably distributed in all directions. The star positions used were taken from the Two Micron All Sky Survey (2MASS, Skrutskie et al., 2006) or United States Naval Observatory (USNO, Monet et al., 2003) catalog, and the Right Ascension and Declination of the selected stars were recorded in an input file. The IRAF *ccmatch* routine was used to determine the center of these sources in the image and calculate plate solution that aligned the image world coordinate system to the reference stars with their known positions. This world coordinate system is standard for the astronomy data format of 'fits' files. The IRAF *ccastrom* routine updated the image headers with the correct coordinate transform (plate solution). Once the images were calibrated and the astrometric fits were computed, the TNO positions and photometric magnitudes were measured. The measured magnitudes provided an additional verification that the object measured was the TNO and that the measurement is uncontaminated by background sources.

The choice of reference stars is important for minimizing the uncertainty of the measurement. Near the tangent plane point a linear (first order) transformation between pixel and sky-coordinates is sufficient. The WCS transformation, where xi and eta are the tangent plane coordinates in radians ($\sim$ Right Ascension and Declination), has the form:

$$\begin{aligned} xi &= CD1\_1 \times (x - CRPIX1) + CD1\_2 \times (y - CRPIX2) \\ eta &= CD2\_1 \times (x - CRPIX1) + CD2\_2 \times (y - CRPIX2) \end{aligned} \tag{2.4}$$

which has six degrees for freedom. The reference points about which the projection and rotation refer are $CRPIX1$ and $CRPIX2$, and the CD values are the coordinate

matrix. For each centroid measured (x, y) there are two parameters, thus a minimum of three stars is required to determine a solution. With additional sources high proper motion stars were more easily identified and excluded from the plate solution fit. (Proper motion of stars is the movement of stars relative to the sun; this is typically only noticeable for nearby stars.) Many imagers have multiple CCD chips combined in order to optimize area while controlling cost and readout time. As a result, these imagers have several chips that do not quite touch, resulting in gaps between the CCD chips. Sources were only considered on the same CCD chip as the target, as reference stars on the outer chips produced significantly higher fit residuals, likely due to uncertainties in the measured chip gap positions.

For these images, the predicted TNO position was found for the date of each observation based on the Bernstein & Khushalani (2000) fit of all previous astrometry. Where possible, the object identification was verified based on target motion. I estimated the photometry of these objects using the aperture method (Section 2.4) to verify that the brightness was consistent with previous measurements.

Once the astrometry was acquired, I fit an orbit (Bernstein & Khushalani, 2000) to the measured positions of our TNOs. The majority of the motion TNOs appear to exhibit is actually parallax due to the Earth's motion. The Bernstein & Khushalani (2000) orbital fitting method uses a coordinate transform to a cartesian coordinate system with the origin on the observer's location (on Earth) at the time of the first measurement. This method accounts for the light-travel time from the TNO to the observer, which is a function of the Earth's location. The accuracy of the Bernstein & Khushalani (2000) orbital fit is limited by the uncertainty in the absolute reference from of the astronomic catalog, the unknown proper motions of stars, and the uncertainty in determining the measured centroids. The uncertainty that results from the Bernstein & Khushalani (2000) approximation of Earth's position (with the observer's location calculated based on a constant rotation and an oblate spheroid) and the uncertainty from their orbital calculations are significantly smaller than the astrometric uncertainty. The method calculates the orbit of an object from the position, velocity, and gravitational perturbations it encounters, based on the Sun and the giant planets. Then a nonlinear minimization is applied to find the solutions to the equations of motion in their cartesian coordinates and transform back into orbital elements. This orbital fitting algorithm is efficient to run and produces object ephemerides, derived from the orbital fits, that precisely predict the locations of the object.

Because I acquired a significant fraction of the known orbital arc at monthly in-

tervals, discrepant astrometric measurements were immediately apparent. For high residual points, I reanalyzed the original astrometric data, and either rejected the images (some had too poor a signal for a sufficiently accurate centroid) or repeated the astrometric plate solution and the astrometric measurement. The resulting final astrometry has unusually small measurement uncertainty (see Table 3.3). To determine the orbital parameters that were consistent with our astrometric measurements and uncertainties, I used a resampling method based on the 0.2 arc second uncertainty of our astrometric measurements, representative of the 1-1.5σ uncertainty range in Right Ascension and Declination. For every set of resampled astrometric points, I recalculated the orbital fit. The solution then retains the interdependence of the orbital parameters and provides a better representation of uncertainty than the Bernstein & Khushalani (2000) uncertainties.

The precise positions of TNOs relative to the stars are necessary for accurate orbit predictions. This requires a careful mapping of sky coordinates onto the CCD image, based on catalog positions of known sources, and is limited in accuracy because of uncertainties in these catalogs. Orbital fits determined from these position measurements have associated uncertainty, which must be carefully propagated to ensure that the real object's orbit is well understood, which is typically done using a number of clones consistent with the objects' orbital parameters.

2.5 Anderson-Darling Statistical Test

In the analysis I frequently use the one dimensional Anderson-Darling statistical test (AD, Anderson & Darling, 1952). The AD statistic sums square of the distance between two cumulative distributions of the same variable from two different samples, similar to the Kolmogorov-Smirnov (KS) test. The AD statistic (D) is adjusted by a weighting function which places more emphasis on the tails of the distribution.

$$D = n \int \frac{(F_n(x) - F(x))^2}{F(x)(1 - F(x))} dF(x) \tag{2.5}$$

The weighting function is the term $w(x) = (F(x)(1 - F(x)))^{-1}$; $w(x)$ is minimum when $F(x)$ is 0.5 and maximum when $F(x)$ is 0 or 1 (i.e. at the ends of the cumulative distribution, $F(x)$). I input the model as $F(x)$ and the measured sample as $F_n(x)$ and calculate the D value. The functional form of the model, $F(x)$, depends on the hypothesis being tested. A common test is to compare the real detections to a Gaus-

sian distribution; I typically use a more complicated model such as the inclination distribution of TNOs (equation 3.1).

The significance of the D value is then calculated by using a bootstrapping method. A synthetic sample is randomly selected (the size of the measured sample) from the model, and the D statistic for this sample is computed compared to the model the synthetic sample was drawn from. Random re-sampling of the model is repeated until a well sampled distribution of D statistics is created, thousands of times. I compare the D statistic from the data to the distribution of D statistics from the model to determine the significance with which I can reject the null hypothesis (the observations can be drawn from the model).

For some of the analysis (see Section 5.4.5), I employ an additional bootstrapping routine to understand the effects of uncertainties in our measurements. I resample each data point within its uncertainty and compute a new D statistic for the new uncertain data distribution. By repeating this process 1000 times, I obtain a mean and standard deviation of D values for the data. As a result, I report a range of significance values which provides the reader with an understanding of the D statistic and a measure of the confidence one might have in the conclusions.

Chapter 3

The 5:1 Neptune Resonance as Probed by CFEPS: Dynamics and Population

This chapter contains my research from Pike et al. (2015). I used the four objects discovered in Petit et al. (2011) and Petit et al. (2014). Dr. JJ Kavelaars and I successfully applied for astrometric observations at Gemini Observatory tracking these targets. I reduced the data and measured the astrometric positions for all images listed in Section 3.3. I calculated orbital fits for the data by modifying an implementation of Bernstein & Khushalani (2000) provided by Dr. JJ Kavelaars. I converted the orbital fits into input for the SWIFT integrator, including aspects of some conversion scripts provided by Dr. Katherine Volk. I wrote a classification script to analyze the output and classify resonance, then extracted the results and plots related to the dynamical simulations. I discussed the implications of some of these results with Dr. JJ Kavelaars, Dr. Brett Gladman, and Dr. Katherine Volk. For the population estimate, I used the survey characterization files provided by Dr. Mike Alexandersen and the CFEPS team, particularly Dr. J. M. Petit. I used a modified version of the survey simulator provide by Cory Shankman, which provided a mechanism for implementing my population model in python. I created the population model and ran the survey simulator to determine the population estimate.

The focus of this chapter is to understand the populations in the outer resonances, particularly the 5:1 Neptune resonance. The discovery of objects from a characterized survey in the 5:1 resonance makes it possible to model the intrinsic population. The

long-term dynamical simulations provide insight into the evolution of this population over time, as well as possible origin from scattering object capture. However, planetary migration models do not produce a population of this magnitude in the 5:1 resonance, so some additional capture or population mechanism may be required.

3.1 Abstract

The Canada-France Ecliptic Plane Survey discovered four trans-Neptunian objects with semi-major axes near the 5:1 resonance, revealing a large and previously undetected intrinsic population. Three of these objects are currently resonant with Neptune, and the fourth is consistent with being an object that escaped the resonance at some point in the past. The non-resonant object may be representative of a detached population that is stable at slightly lower semi-major axes than the 5:1 resonance. We generated clones of these objects by resampling the astrometric uncertainty and examined their behavior over a 4.5 Gyr numerical simulation. The majority of the clones of the three resonant objects ($> 90\%$) spend a total of 10^7 years in resonance during their 4.5 Gyr integrations; most clones experience multiple periods of resonance capture. Our dynamical integrations reveal an exchange between the 5:1 resonance, the scattering objects, and other large semi-major axis resonances, especially the 4:1, 6:1, and 7:1. The multiple capture events and relatively short resonance lifetimes after capture suggest that these objects are captured scattering objects that stick in the 5:1 resonance. These 5:1 resonators may be representative of a temporary population, requiring regular contributions from a source population. We examined the dynamical characteristics (inclination, eccentricity, resonant island, libration amplitude) of the detected objects and their clones in order to provide an empirical model of the orbit structure of the 5:1 resonance. This resonance is dynamically hot and includes primarily symmetric librators. Given our orbit model, the intrinsic population necessary for the detection of these three objects in the 5:1 resonance is 1900^{+3300}_{-1400} (95% confidence) with $H_g < 8$ and $e > 0.5$.

3.2 Introduction

The Trans-Neptunian Objects (TNOs) in the outer Solar System are the remnants of the original planetesimal disk, a record of the composition and history of the Solar System. Many TNOs have experienced large dynamical perturbations as a result of

giant planet interactions, particularly with Neptune (e.g. Malhotra, 1995; Levison et al., 2008; Batygin et al., 2011; Dawson & Murray-Clay, 2012). The dynamical history of the outer Solar System results in a complex dynamical structure in this region. The TNOs are dynamically classified into sub-populations. The clump of TNOs with low eccentricity, e, and low inclination, i, found between 42-47 AU is referred to as the cold classical Kuiper belt (Kuiper, 1951). These objects may have undergone little dynamical perturbation. A large number of objects, however, are currently dynamically interacting with Neptune. These scattering objects have pericenters, q, between $\sim$30-37 AU, such that giant planet interactions cause changes in orbital properties (such as semi-major axis, a) of the TNO on timescales of 10 million years (Gladman et al., 2008). Objects with larger q are no longer interacting with Neptune and are considered detached (Gladman et al., 2002; Delsanti & Jewitt, 2006; Gladman et al., 2008). A significant fraction of TNOs are trapped in mean motion resonances with Neptune (Gladman et al., 2008). The objects trapped in these mean motion resonances provide a unique diagnostic of the dynamical history of the outer Solar System (Gladman et al., 2012) because resonance dynamics preserve TNOs which would otherwise scatter out of their present locations. Mapping and cataloging these TNO populations will provide insight into the planetesimal disk's origins and evolution.

The resonance structure in the outer Solar System is extremely complex. Significant populations of TNOs have been identified in the 3:2 resonance, at $\sim$39 AU where Pluto resides, and in the 5:1 resonance at 88 AU, as well as in many other Neptune mean motion resonances. Lykawka & Mukai (2007b) find that resonance sticking occurs out to 250 AU, which implies there may be other resonance populations, such as 6:1 resonators, still undetected. The resonances each have different trapping efficiencies (Lykawka & Mukai, 2007b), and if the resonances share the same source population their trapping efficiencies constrain their relative populations. Many of the closer resonances (7:4, 5:2, 5:3, etc.) appear to contain objects with colors similar to the cold as well as the hot classical belt objects (Sheppard, 2012) and it is unknown if this trend continues to larger a. One must, however, be cautious when comparing colors of different populations of TNOs as detection biases can produce misleading results (Pike & Kavelaars, 2013). Part of these resonant populations (of all surface types) were likely captured through a sweep up process during giant planet migration, similar to the capture of Pluto described by Malhotra (1995). Objects can also enter a resonance via a phenomenon referred to as 'resonance sticking' (Dun-

can & Levison, 1997; Gomes et al., 2005; Lykawka & Mukai, 2006, 2007b). In this process, objects in the scattering disk population experience orbital perturbations that move them into the resonant phase space. The objects then become temporarily ($\sim 10^5$ years) or long-term ($> 10^7$ years) stable in the resonance. Temporary resonance sticking extends the lifetimes of scattering objects (Lykawka & Mukai, 2006), so these populations are dynamically linked. The complex dynamical structure of the known resonant objects can be used to constrain the possible resonance capture mechanisms and source populations for the resonances.

The resonance structure in the outer Solar System has been explored by analytical models and dynamical simulations. The structure of the 5:1 resonance in eccentricity and semi-major axis space is described in Morbidelli et al. (1995), demonstrating that the resonance width is greatest at $e \sim 0.5$. The n:1 resonances contain symmetric and asymmetric libration islands (Beauge, 1994; Malhotra, 1996; Murray-Clay & Chiang, 2005; Gladman et al., 2012) that determine where the TNOs come to pericenter relative to Neptune. The n:1 resonances are the strongest resonances in the scattered disk (Gallardo, 2006). The Kozai mechanism (Lidov, 1962; Kozai, 1962), characterized by an exchange of eccentricity and inclination, occurs in portions of resonance phase space. Gallardo et al. (2012) find that the Kozai mechanism occurs in the n:1 resonances when the inclination is higher than a critical value which increases with semi-major axis. This lifts the pericenters of the resonant objects. The orbital characteristics of the intrinsic population is required for the interpretation of 5:1 resonant TNOs discovered in surveys.

Discovery biases complicate all TNO studies, but the complex structure of the 5:1 resonance makes observational studies particularly challenging. Typical survey biases include limiting magnitudes, latitude of pointings, observation cadence, and followup methods. Resonant populations also have a longitudinal bias because these populations come to pericenter (maximum detectability) at a specific range of longitudinal offsets relative to Neptune. The particular location of these pericenters depends on the resonance structure; the 5:1 resonance contains both symmetric and asymmetric libration islands. Ignoring libration, the 5:1 objects come to pericenter at approximately 180° (symmetric), 120° (leading), and 240° (trailing) ahead of Neptune; the precise locations are e dependent. As a result, a survey pointing near one of these pericenter locations would be biased toward the discovery of 5:1 TNOs from a particular island. Pointing away from these locations can reduce the likelihood of discovery because these objects are typically only brighter than survey detection lim-

its when they are near pericenter. A well characterized survey with accurate pointing and depth information is needed to understand the size and substructure of the 5:1 resonance population (Jones et al., 2006).

In this chapter we examine four objects discovered near the 5:1 resonance to determine their dynamical classification, and then we use the characteristics of the 5:1 resonant TNOs to build a parametric model of the population. Our observations and astrometry are presented in Section 2. In Section 3 we characterize the uncertainty in our measurements and show the results of our orbital integrations of the clones of these TNOs. We create a parametric model of the 5:1 resonance and determine a population estimate in Section 4. Finally, Section 5 and Section 6 contain a discussion of our results and our conclusions.

3.3 Observational Data

The Canada-France Ecliptic Plane Survey (CFEPS), a characterized 803 degree^2 survey dedicated to detecting and tracking TNOs, discovered four objects with semi-major axes near the 5:1 Neptune resonance, at $\sim$88 AU (Petit et al., 2011, 2014). The first portion of the survey (321 degree^2) targeted the ecliptic plane; these fields were located within a few degrees of the ecliptic plane. The second portion of the survey (482 degree^2) pointed off the ecliptic with the goal of providing constraints on the inclination distributions of TNOs by characterizing detections at higher latitudes. The higher latitude blocks have a lower TNO discovery rate, but these fields provide a lever arm on the inclination widths of TNO populations and discover some interesting high inclination objects. L3y02 was discovered in the ecliptic CFEPS fields (2003), and HL7c1, HL7j4, and HL8k1 were discovered in the high latitude fields (2007-2008). All four of these objects have large inclinations (20°-50°), requiring the intrinsic population to be dynamically excited. The combined CFEPS ecliptic and high latitude fields constrain the inclination distribution of the intrinsic population better than purely ecliptic surveys because high i populations spend more time at high latitudes and are more difficult to discover in ecliptic surveys.

After orbital determination in CFEPS, a number of objects were flagged for extended astrometric followup because large a resonant objects require longer arcs to conclusively classify the objects (Jones et al., 2010). Additional astrometry was taken over several years using Megacam on the 6.5 meter Magellan telescope in Las Campanas Observatory, Chile and the Gemini Multi-Object Spectrograph (GMOS) in

imaging mode on the 8.1 meter Gemini North telescope on Mauna Kea, Hawaii, USA. We focus here on the data from Magellan and Gemini, see Table 3.1. Data were taken for two of the targets using Magellan Megacam in r band in 2010 and 2011. The GMOS data from 2012-2013 included observations of each of the targets for multiple nights in each of 3-4 dark runs, approximately 1-2 months apart. The GMOS-N imaging data was taken in queue mode, which is optimal for short exposures of a few targets spread over several months. We observed in r band with a target signal to noise ratio of 10 which gives a centroid precision comparable to the catalog precision. We took a single 7 second exposure of each target field to ensure a non-saturated image of the field stars used for astrometric calculation. Our longer exposure times were based on the magnitude of each object, and we observed each object twice per dark run when possible. The telescope tracked at the stellar rate of motion, which caused negligible extension in the TNO PSF due to motion ($\lesssim$1.7 arc seconds per hour). Some elongation of the TNO was apparent in the 300 second exposures, but the PSF core was sufficiently well defined for a centroid calculation with comparable precision to the astrometric catalog. The astrometry from Gemini and Magellan were then used to refine the orbital fits.

We calibrated the data prior to determining the coordinates of the TNOs. The observations were processed and analyzed using the Image Reduction and Analysis Facility (Tody, 1993, IRAF). Baseline reductions as prescribed by Gemini were performed on the GMOS images. This includes a bias subtraction, flat fielding, and combining the different amplifier chips into a single image. For the data from Gemini and Magellan, TNOs were identified based on their predicted positions and confirmed using object motion in the case of multiple exposures. However, the predicted positions were sufficiently accurate for the easy identification of the target even without identifying its motion with respect to the stars. An astrometric plate solution tied to either the The Two Micron All Sky Survey (Skrutskie et al., 2006, 2MASS) or United States Naval Observatory (Monet et al., 2003, USNO) catalog (depending on the availability of sources) was calculated. We achieved an astrometric fit RMS $\lesssim$0.15 arc seconds, which limits the precision of our observations to the accuracy of the astrometric reference frame. Astrometry was reported to the Minor Planet Center[1] (MPC) and used in object orbit predictions.

We performed an orbital fit (Bernstein & Khushalani, 2000) to all known astrometry of these objects, and all 4 TNOs (Trans-Neptunian Objects) were still near the 5:1

[1] http://www.minorplanetcenter.net/

Table 3.1 Astrometric Images.

Object	Date	Telescope	Exposure Time
L3y02	2013/02/05	Gemini	2×100 sec.
	2013/03/19	Gemini	2×100 sec.
	2013/04/04	Gemini	2×100 sec.
	2013/04/05	Gemini	2×100 sec.
HL7j4	2013/04/03	Gemini	1×100 sec.
	2013/04/04	Gemini	1×100 sec.
	2013/04/30	Gemini	1×100 sec.
	2013/05/03	Gemini	1×100 sec.
	2013/06/10	Gemini	1×100 sec.
	2013/06/15	Gemini	1×100 sec.
	2010/04/21	Magellan	1×120 sec.
	2011/05/02	Magellan	2×120 sec.
	2011/05/03	Magellan	1×120 sec.
HL7c1	2013/02/06	Gemini	2×122 sec.
	2013/02/06	Gemini	2×122 sec.
	2013/03/04	Gemini	2×122 sec.
	2013/03/19	Gemini	2×122 sec.
	2013/04/03	Gemini	2×122 sec.
	2013/04/04	Gemini	2×122 sec.
HL8k1	2013/04/09	Gemini	3×300 sec.
	2013/04/09	Gemini	3×300 sec.
	2013/05/03	Gemini	3×300 sec.
	2013/05/12	Gemini	3×300 sec.
	2013/06/17	Gemini	3×300 sec.
	2013/07/11	Gemini	3×300 sec.
	2013/07/15	Gemini	3×300 sec.
	2010/04/21	Magellan	1×400 sec.
	2011/05/02	Magellan	2×400 sec.

resonance. These new astrometric data were combined with astrometry previously acquired using CFHT, earlier Magellan data, and additional resources (L3y02: University of Wisconsin-Madison, Indiana University, Yale University, and the National Optical Astronomy Observatories Telescope (WIYN), Palomar Hale, and 2.1-m at Kitt Peak; HL7c1: Palomar and WIYN; HL7j4: WIYN, Palomar, Cerro Tololo Inter-American Observatory, and Nordic Optical Telescope; HL8k1: Subaru, WIYN, and Palomar; Petit et al. (2014)). Many years of high precision astrometry is often necessary for resonance classification (Gladman et al., 2008) because resonance behavior can only be securely identified using forward numerical integration of the object's state vector. Table 3.3 shows the results of orbital fits for the objects using Bernstein & Khushalani (2000). These objects have an orbital period of 820-830 years, so the

orbital fit is based on observations of only ∼1% of the orbit. This small arc requires extremely accurate astrometry, like the measurements presented here, in order for integrations to conclusively determine resonance occupation. Our numerical integration of clones (presented in the next section) illustrate the complexity of classifying these objects.

Table 3.2 Nominal Object Orbit Fit. The arc lengths show the years of the earliest and most recent astrometry. The number of astrometric points, n, is provided as well; this large number of measurements is necessary in order to characterize the objects' orbits. L3y02 was measured in g and r band, so the H_g magnitude of that object is calculated. The other 3 objects were measured in r, so their approximate H_g is given, assuming a $g - r = 0.5$ conversion. The distance at discovery is d.

MPC ID	CFEPS ID	Observational Arc [years]	n	H_g (H_r) [mag]	d [AU]
2003 YQ_{179}	L3y02	2003-2013	32	7.3 (6.6)	39.3
2007 FN_{51}	HL7c1	2007-2013	40	∼7.7 (7.2)	39.1
2007 LF_{38}	HL7j4	2007-2013	51	∼6.0 (5.5)	48.4
2008 JO_{41}	HL8k1	2008-2013	33	∼8.4 (7.9)	44.5

Table 3.3 All digits shown for orbital elements are significant based on the barycentric orbital fit and uncertainty from Bernstein & Khushalani (2000). The semi-major axis (a), eccentricity(e), inclination (i), ascending node (Ω), argument of pericenter (ω), and Epoch are from the Bernstein & Khushalani (2000) orbital fit.

CFEPS ID	a [AU]	e	i [°]	Ω [°]	ω [°]	T [JD]	Epoch [JD]
L3y02	88.41	0.5787	20.874	109.793	30.558	2458824.134	2452998.0
HL7c1	87.49	0.6188	23.237	102.286	9.961	2445268.018	2454180.9
HL7j4	87.57	0.5552	35.825	169.293	12.737	2439708.039	2454263.8
HL8k1	87.34	0.5431	48.815	153.057	146.552	2464523.688	2454598.0

3.4 Characterization of Discoveries

This section describes how the astrometry and its uncertainty for each of the targets was used to determine a cloud of clones of the object and presents the results of the forward integration of these clones.

3.4.1 Estimation of Orbital Uncertainties

All astrometric measurements have inherent uncertainties that come from a variety of sources. Errors in the initial orbit solution and location prediction can make target identification and astrometric fits difficult. Stellar crowding, plate boundary errors, stellar motion, and sparse catalogs can make astrometric plate solutions less accurate. Because of these issues, systematic offsets for all observations in a single observing run are common. When a target has clusters of astrometry separated by months without observations, a systematic offset from one observing run can significantly bias the orbital fit (Gladman et al., 2008). Accounting for all sources of uncertainty in astrometric measurements can result in a wider range of orbital fit parameters than a simple orbital fit would suggest.

During our orbital fitting procedure, we examined all outliers in the astrometric fits to determine if the discrepant astrometry should be kept. With years of astrometry, much of it at monthly cadences, outliers are immediately obvious in the fit residuals calculated with the routine by Bernstein & Khushalani (2000). We revisited the original data for all high residual astrometric points, and re-examined the astrometric plate solution. For most of these observations, we calculated a new astrometric position. For several others, we found that a good astrometric solution could not be derived, which occurred as a result of low signal on the TNO (centroiding was impossible) or an insufficient number of (unsaturated) reference stars. We replaced or removed the astrometry in the orbital fit and repeated the check for outliers. Our careful re-measurement of discrepant points resulted in significantly improved astrometry for all of our objects.

Systematic astrometric offsets result in poor orbital predictions for TNOs observed once or twice a year for a limited period of time (Gladman et al., 2008). The orbit parameter estimation by Gladman et al. (2008) allows systematic offsets for some of the astrometric points and calculates the largest and smallest a clones possible from the astrometry. The larger orbit uncertainties occasionally reveal the possibility of resonance behavior for TNOs near a resonance boundary. These targets may have high a or low a clones which show a resonant angle libration. Gladman et al. (2008) noted this effect for L3y02, which at the time would not have been flagged as a potentially resonant object based on the Bernstein & Khushalani (2000) uncertainty range. The Gladman et al. (2008) classification is useful for targeting possible resonant objects with small or sparsely sampled arcs for additional astrometric followup, because

these objects may have systematic offsets in their astrometry that are not apparent from the fit residuals.

Our combination of lower than average astrometric uncertainty and better observation cadence over long arcs allows us to develop our own estimation of the uncertainty in the objects' orbital parameters. After discrepant astrometry is removed from our results, the only sources of uncertainty in our data are the uncertainty in the position of reference stars and the centroid calculation of sources. Our astrometry is accurate to ∼0.2 arc seconds. Instead of using the method by Gladman et al. (2008), we resampled each of our astrometric points linearly within their uncertainty of 0.2 arc seconds. This resamples the astrometry of the objects within 1-1.5σ uncertainty range in Right Ascension and Declination. We calculated a new orbital fit to the resampled astrometry for the object, so we have new orbital parameters for each resampled clone. Repeating this resampling process ∼1500 times provides the range of orbital parameters that are consistent with the astrometric measurements. Using multiple orbital fits instead of resampling the uncertainty on each orbital parameter from Bernstein & Khushalani (2000) also allows us to preserve the interdependency of the orbital parameters. The result was a cloud of clones of each TNO, shown in Figure 3.1. The behavior of the clones over time provides an exploration of the resonance behavior for orbits that are consistent with our knowledge of the intrinsic orbit of these four TNOs.

3.4.2 Dynamical Integrations

We integrated the clones of the 4 potential 5:1 objects for approximately 4.5 Gyr using SWIFT (Levison & Duncan, 1994) in order to determine resonance occupation for each initial condition. SWIFT integrates gravitationally interacting objects using a provided time-step, 0.5 years for this simulation. We used the Regularized Mixed Variable Symplectic (RMVS) method which handles test particle–planet close approaches. The position, velocity, and mass of the Sun, Jupiter, Saturn, Uranus, and Neptune were included as massive bodies, and their initial conditions were calculated for the epoch of the TNO's orbital fit. The clones of the possible 5:1 TNOs were added as massless test particles. We observed a variety of behaviors over the integration time, including short ($\sim 10^5$ years) or long ($> 10^7$ years) term resonance occupation in different 5:1 libration islands, scattering, capture into other Neptunian resonances, and stable non-resonant behavior. Because we are interested in the region

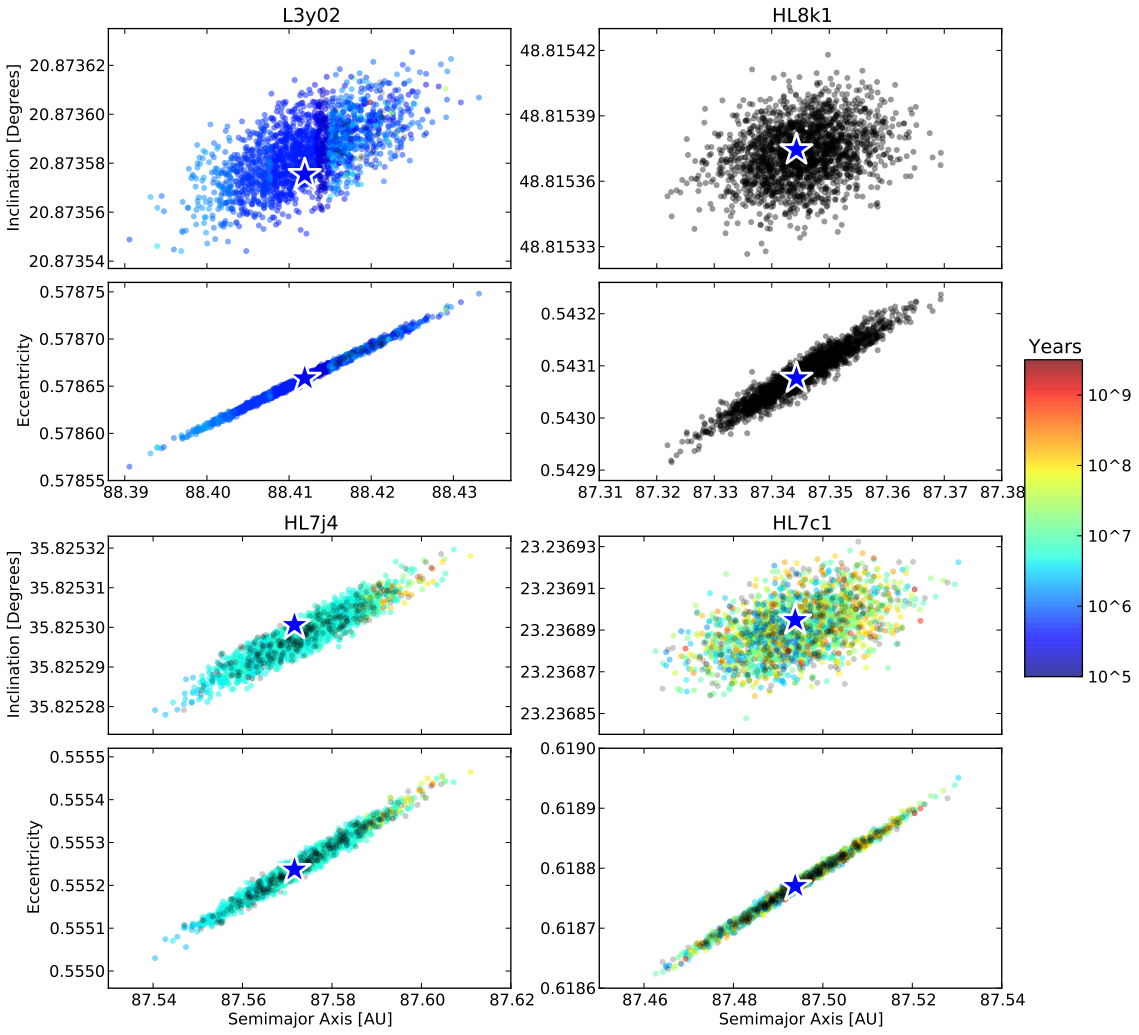

Figure 3.1 The $\sim$ 1500 clones for each TNO are shown here. The nominal best fit clone (no resampling) is shown with a blue star. The other orbital fits were calculated by resampling the astrometry within the uncertainty and producing additional orbital fits. This sample sufficiently explores the phase space; additional clones do not significantly alter the range of a, e, and i values. These clones provide a weighted sampling of the 1.5σ uncertainty range of the orbit, so the median orbital behavior may be indicative of the intrinsic orbit. The color indicates the duration of the first period of resonance occupation from the numerical integrations; if the object displays resonant behavior for $> 10^7$ years the object would be classified as resonant based on Gladman et al. (2008). Many of the clones display multiple periods of resonance and have significantly longer total 5:1 resonance occupation. Section 3.2 provides details on resonance diagnosis. Black indicates a non-resonant clone.

near the 5:1 resonance, test particle information was recorded only for heliocentric distances between 20 AU–150 AU. The positions of the clones that went outside these ranges were not recorded while they were beyond the limits. The behavior of all of the clones provides possible classifications of the TNOs found in our survey.

We determined whether an initial condition was resonant by examining the behavior of the resonant angle. Typically, secure resonant classification requires the resonant angle to librate for 10^7 years from the start of integration for the best fit clone as well as the minimum and maximum a clones (Gladman et al., 2008). We classified objects as resonant if their resonant angle oscillated instead of exploring a full 360° circulation. Following the method of Alexandersen et al. (2013) for the 1:1 resonance, we used a moving window to examine the resonant angle behavior. Because many of these objects experienced multiple periods of resonant libration, the beginning and end of each resonant period was recorded. HL8k1 is never resonant, while L3y02, HL7j4, and HL7c1 all show periods of resonant behavior during the simulation.

3.4.3 HL7j4

Based on our simulations, HL7j4 is in the 5:1 resonance. The behavior of the best fit clone over the first 500,000 years of the simulation is shown in Figure 3.2. This symmetric oscillation was observed for all of the clones for a minimum of 2×10^6 years, so we classify this object as a symmetric 5:1 librator. The median duration of the first period of resonance is 4.9×10^6 years. See Figure 3.1 for a plot of resonance duration. The higher occurrence of longer lived clones in the large a, e, and i corner suggest that this region may be more likely to contain the 'true' orbit of the TNO. When the resonant periods for each clone are summed, more than 99% of the clones are resonant for at least a total of 10^7 years of the entire simulation, and 80% are resonant for 10^9 years. Of the clones that leave the 5:1 resonance, several are captured into other distant resonances, including the 6:1 and 7:1 resonance. Of our four objects, HL7j4 has the highest fraction of resonant clones that are also in the Kozai resonance (Lidov, 1962; Kozai, 1962), which can lead to larger variations in the test particles' eccentricities and inclinations. The clones of HL7j4 display the most stable resonant behavior of our test particles, and the 'true' TNO may be on an orbit in a portion of the phase space stable for ∼Gyr.

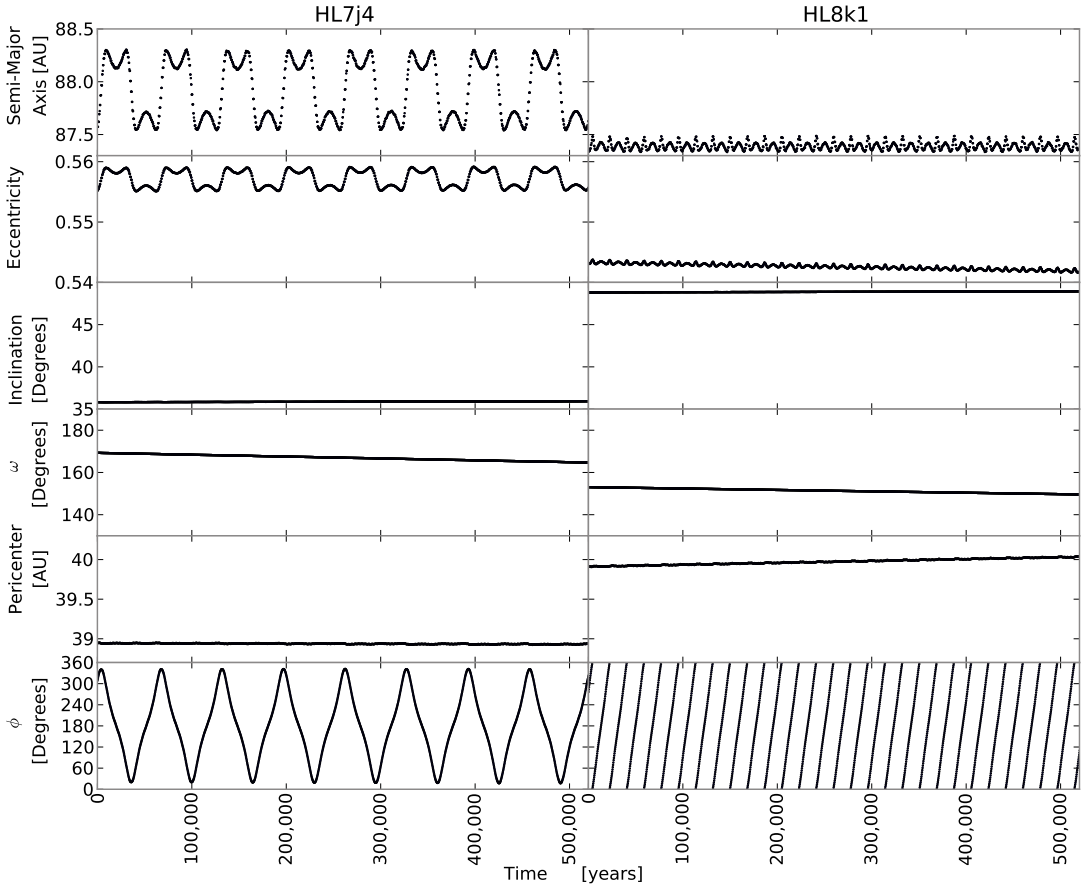

Figure 3.2 Orbital element evolution (sampled at 300 year intervals) of the best fit clone of HL7j4 (left) and HL8k1 (right) are shown for 5×10^5 years (representative of the behavior of both objects for the first 10^7 years). This clone of HL7j4 shows typical resonance behavior. Each libration of the resonance angle corresponds to residence in both the maximum and minimum a in resonance. The majority of the clone's time is spent at these extreme a values, near the resonance boundary. The matching oscillations in e result in a nearly constant q for the object. This clone of HL8k1 is not resonant (similar to all other clones of HL8k1); its resonance angle circulates. This object appears to be in a stable position just slightly sunward of the 5:1 resonance with a slightly lower a than the resonance border.

3.4.4 HL7c1

HL7c1 is also a 5:1 resonator. The best fit clone is resonant for the first 6×10^7 years, before exiting the resonance. The clone experiences two additional short resonance captures ($\sim 10^5$ years) before scattering outward. The best fit clone passes beyond

150 AU at 3.2×10^8 years, then re-enters the region of interest at 7.1×10^8 years. It moves beyond 150 AU again briefly before scattering inward at 9.5×10^8 years where the simulation output ends. All clones of this object begin in symmetric 5:1 resonance, and remain in symmetric resonance for a minimum of 10^6 years. The duration of the first resonance occupation for these clones is shown in Figure 3.1. The seemingly random distribution of resonance occupation times suggests that no particular *aei* region is favored. The median duration of the first period of resonance is 1.6×10^7 years. Approximately 90% of the clones of this object are resonant for a total of at least 10^7 years. However, only 30% are resonant for a total of 10^8 years and <10% for a total of 10^9 years. After the clones leave the resonance, the majority move into scattering orbits and some become detached objects. Some of these scattering clones are captured into other resonances and some are ejected from the region of our SWIFT output (20AU-150AU). HL7c1 is currently a 5:1 resonator.

3.4.5 L3y02

L3y02 is also classified as resonant. The best fit clone begins with 5×10^4 years of resonance, exits the resonance, then re-enters the resonance at 2×10^6 years. Similar behavior is observed for the other clones; there are multiple periods of resonance broken by non-resonant behavior. All of these clones begin their first resonance as symmetric librators. The median duration of the first period of resonance is 6.0×10^5 years. Most of the resonance periods are of short duration; the length of resonance for each clone is shown in Figure 3.1. Over 95% of the clones are resonant for a total of at least 10^7 years during the simulation, 80% for 10^8 years, and 50% for 10^9 years during the simulations. When leaving the resonance, these clones preferentially exit to low a, just sunward of the 5:1 resonance. Many clones remain there, becoming detached objects while the others enter the scattering population, some of which are captured into other resonances.

3.4.6 HL8k1

HL8k1 is not in the 5:1 Neptune resonance, in spite of being extremely close to the resonance boundary. All of its clones experience small periodic oscillations in a and e, shown in Figure 3.2, but not with the characteristic periodic pattern seen in the resonant object integrations. The resonant angle shows only a slow circulation instead of a bounded oscillation, so HL8k1 is classified as a detached object according to the

Gladman et al. (2008) classification scheme. HL8k1 is not resonant, but it may have been associated with the 5:1 resonance at some point in the past.

3.4.7 Resonance Characteristics

The resonant angle behavior in Figure 3.2 for HL7j4 is representative of a typical symmetric libration behavior. Most of the clones of our three 5:1 objects are primarily symmetric librators, although a small number of clones transition into periods of asymmetric libration. The resonance angle ϕ librates with a high amplitude centered around 180°. This large amplitude symmetric libration was typical for $\sim$ 90% of the resonant clones; the smaller amplitude asymmetric libration was far less common and typically occurred between periods of large amplitude symmetric libration. The intrinsic asymmetric fraction of the resonance could be as high as $\sim$30% if the fraction is similar to the n:1 resonance symmetric fractions from Gladman et al. (2012). Our smaller observed fraction may be the result of the longitudinal biases of the discovery surveys. Understanding the distribution of the libration amplitudes and libration centers will be critical to understanding the 5:1 resonance capture process.

The detected 5:1 TNOs all have large eccentricity (> 0.54), but $\sim$5% of their resonant clones were found to undergo a decrease in eccentricity as a result of resonant dynamics. The eccentricity of resonant clones ranged from approximately 0.65 to 0.30, with the majority of clones having values between 0.5-0.65. After 10^9 years 3% of resonant clones had cycled to an e below 0.5, and after $2\text{x}10^9$ years 5% of the remaining resonant clones had cycled to an $e < 0.5$. This cycling is visible in Figure 3.3 and Figure 3.4. This suggests that a Kozai mechanism (Lidov, 1962; Kozai, 1962), where there is an exchange between eccentricity and inclination, is acting on the clones. The evolution of e and i results in objects with inclinations up to 45°. These objects remained primarily resonant, with low e and larger q than the detected objects in the 5:1 resonance. The greater stability of low e objects in the 5:1 resonance, combined with the supply of this population from large e objects, implies that there is likely a population in the 5:1 resonance stored at low e. Many of the 5:1 resonators that are also in Kozai resonance will cycle back to a larger e over time, so the fraction of objects at low e remains relatively constant after 10^9 years. Current survey depths make it nearly impossible to detect all but the brightest low e 5:1 objects; for CFEPS with limiting magnitude of g $\sim$23.5-24.4 (Petit et al., 2011), a 5:1 TNO with $e = 0.3$ (q$\sim$61 AU) would have to have an absolute magnitude H_g $\sim$5.6-6.5 in order to be detected

at perihelion. (See section 1.4 for details on H magnitudes.) We did not detect any low e objects, so to avoid complication from this possibly interesting component we ignore this $\sim$5% component of low e objects that may have evolved from larger e objects when we calculate our population estimate in Section 4.

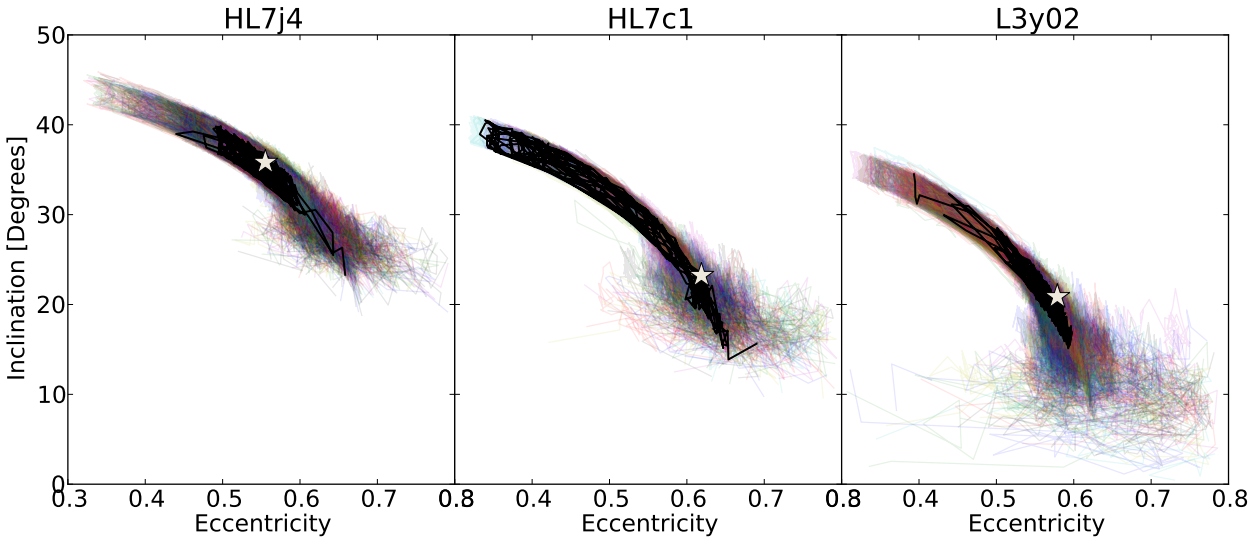

Figure 3.3 Each colored line shows the evolution of a single clone over the age of the Solar System (up to 4.5 Gyr) from the integrations (3.4.2) in eccentricity and inclination. A typical clone in Kozai is bold in each plot. The plot includes all clones with a mean $87 < a < 89$, which limits the plot to primarily resonant TNOs. The current best fit orbital parameters for each object are marked with a star. The Kozai mechanism in the 5:1 resonance is apparent at the upper left of each plot; the resonant objects that evolve to low eccentricity experience a simultaneous increase in their inclination. The Kozai evolution track is obvious in this plot, however, these clones are only $\sim$5% of the test particles.

The clones of the resonant objects that left the resonance with e values such that they do not immediately scatter off Neptune were preferentially deposited or retained at a and e values similar to the current orbit of HL8k1, the non-resonant object. This overabundance of clones is shown in Figure 3.4. These objects are found along the resonance borders and at a slightly smaller a and e than the 5:1 resonance. HL8k1 exhibits stable behavior over the age of the Solar System. Figure 3.2 shows the first 5×10^5 years of HL8k1's evolution, and the behavior is representative of the entire 4.5 Gyr history of all clones of HL8k1. The clones experience regular, but small, changes in a and e as well as slow evolution of the resonance angle. None of the clones of

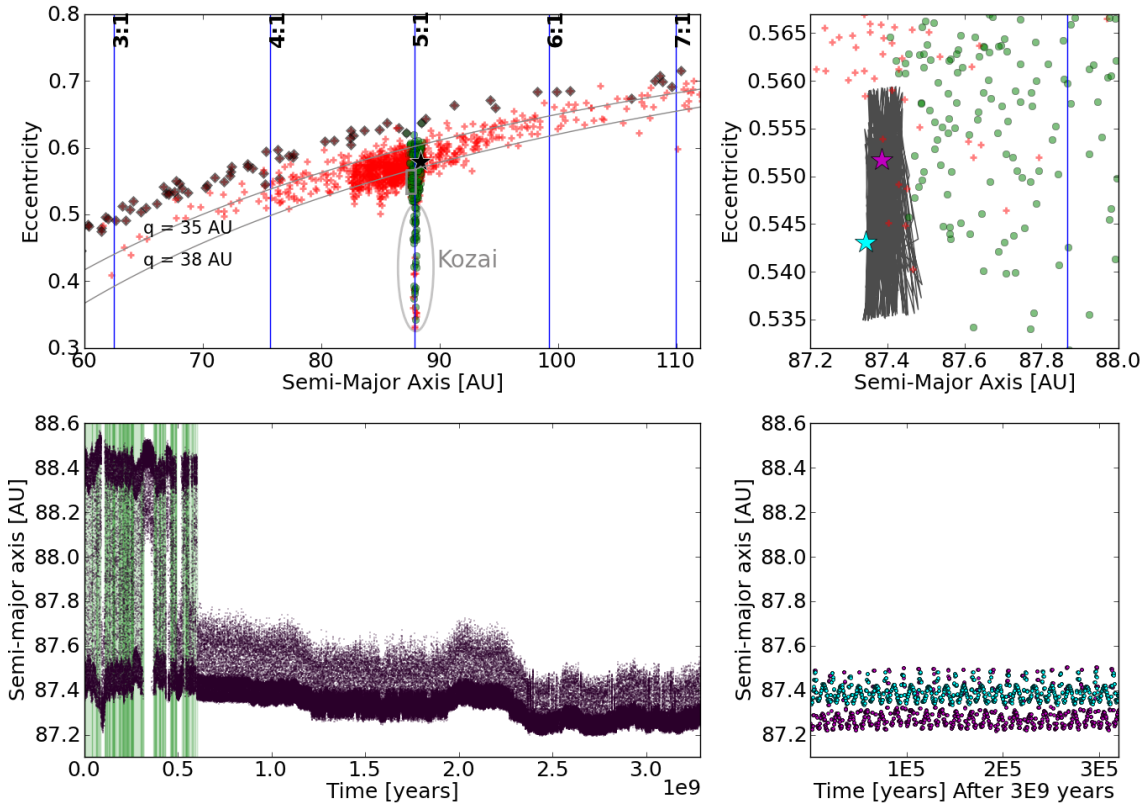

Figure 3.4 Upper Left: This end state plot shows all clones of the resonant object L3y02. The clones which are 5:1 resonators at that time are marked in green circles, non-resonant clones are red '+', and the last recorded position of 'lost' objects are marked with black diamonds. The black star indicates the initial conditions of L3y02. The grey arcs mark the 'q=35 AU' and 'q=38 AU' lines. The clones that have traveled down the 5:1 resonance (decreasing eccentricity) create a population beyond our detection limits as a result of Kozai cycling. This snapshot also contains escaped clones which have been captured into the 3:1 and 7:1 resonance. The overabundance of objects just inside the 5:1 resonance is a pseudo-stable population, likely produced by chaotic diffusion away from the resonance border, of which HL8k1 may be a member. Upper Right: The zoomed in region from the grey rectangle in the left plot shows the non-resonant objects just sunward of the 5:1 resonance boundary. The grey line traces the path of the nominal non-resonant clone of HL8k1 (cyan star) for 3×10^9 years. The magenta star is an end state clone of L3y02 that has diffused out of the resonance. Lower Left: The evolutionary history in a of the magenta resonance diffusion L3y02 clone. Resonant periods are shaded green. Lower Right: A zoomed plot of a for this non-resonant L3y02 clone beginning at 3×10^9 years. The a evolution is similar to HL8k1 (cyan).

HL8k1 are captured by the resonance during their 4.5 Gyr integrations, which reflects the low probability of reentering the resonance. This object could have been emplaced in its current location during Neptune's migration (Gomes et al., 2008) or diffused out of the resonance without the aid of planetary migration, which was not included in our simulations. We use 'resonant diffusion object' to refer to a TNO that appears to have leaked out of a resonance and entered a pseudo-stable region of phase space. The near-resonant object, HL8k1, was likely dynamically associated with the 5:1 resonance and may be representative of a large number of resonant diffusion objects.

3.5 5:1 Population Model

Because of the many biases against detection, the discovery of three distant 5:1 resonant TNOs in the CFEPS survey clearly indicates that the 5:1 Neptune resonance is well populated. We created a model population of objects based on the known characteristics of the real objects, the stability structure of the 5:1 resonance, and the parametric distributions of other known resonant populations. The sensitivity and pointings of the Alexandersen et al. (2016) and CFEPS surveys are known (Petit et al., 2011, 2014). We combined our model of the 5:1 resonance with the discovery biases for real objects in order to estimate the size of the intrinsic 5:1 population.

3.5.1 Parametric Model of the Resonance

Our model of the 5:1 resonance is based on the regions of dynamical stability. The structure of the n:1 resonances is complex, due to the presence of multiple libration islands. The symmetric resonance objects come to pericenter 180° from Neptune (plus or minus their libration amplitude which can approach 180°), and the objects in the two asymmetric resonant islands come to pericenter on each side, 120° from Neptune (plus or minus a smaller libration amplitude). These complexities make visualization difficult, but a simplified model of the 5:1 resonance is presented in Gladman et al. (2012). Here we use a similar parameterization of the resonance structure.

The semi-major axis range of a resonance is restricted by the resonance width. The exact width depends on the other orbital parameters (such as inclination and eccentricity), but for the purposes of detectability it is sufficient to establish a model with a single range of a values. While the density of points at the a resonance edges in the left plot in Figure 3.2 make it clear that the clones spend the majority of their

time near the resonance edges, the resonance is narrow enough that this complication does not have a significant impact on the detectability of model objects. We model the a range as a simple uniform distribution between 87.9 and 88.9 AU.

The objects in the 5:1 resonance appear to have a very excited inclination distribution. The detected objects all have high inclinations, even L3y02, which was discovered in the ecliptic block of CFEPS. The ecliptic blocks of CFEPS were sufficiently deep that 5:1 objects with low i would have been detectable if they were present. The detection of a high inclination object near the ecliptic, where high i objects spend only a small fraction of their orbits (Gladman et al., 2012), as well as two object discoveries in the high latitude blocks indicates that this population is dynamically excited.

Based on our model analysis, we find that the 5:1 resonance probably has a wider inclination distribution than the Plutinos. We implemented an inclination distribution parameterization from Brown (2001) which is acceptable for other studied resonances (Gladman et al., 2012).

$$P(i) \propto \sin(i) \times \exp\left(\frac{-i^2}{2\sigma_i^2}\right) \tag{3.1}$$

We drew inclinations randomly from this inclination distribution for our 5:1 population model, using $5^\circ < \sigma_i < 65^\circ$ in increments of 1°. 10,000 simulated detections were produced using the CFEPS survey simulator, and then the inclination of these simulated detections was compared to the three measured object detections. We used the Anderson-Darling statistical test with a bootstrapped sample from the simulations to determine the likelihood of reproducing the three measured inclinations, shown in Figure 3.5. HL8k1 has the largest inclination of the discovered objects, so if the fourth object were included, the inclination width would be higher. The most acceptable inclination width, σ_i, for the three 5:1 objects was 22°. We reject inclination widths less than 15° and more than 43° at 95% confidence. The published inclination widths for the Plutinos are $14^{\circ+8}_{-4}$ (Alexandersen et al., 2016, 95% confidence limits), and $16^{\circ+8}_{-4}$ (Gladman et al., 2012, 95% confidence limits), and $10.7^{\circ+2.0}_{-2.3}$ (Gulbis et al., 2010, 68% confidence limits). We find that the 5:1 resonance likely has a wider inclination distribution than the Plutinos and other hot TNO populations, however we cannot rule out some similar inclination widths at 95% confidence.

It is possible that a significant fraction of objects in the n:1 resonances are a result of resonance sticking from the scattering object population, either currently or in a

primordial scattering event. Resonance sticking objects may not include a distribution that extends to low inclinations, in which case the Brown (2001) distribution may overestimate the size of the resonance population. Our sample of 3 objects is too small to rule out a low i tail, but simulations of planetary migration resulting in resonance sticking show an inclination distribution not centered at zero (Gomes et al., 2005). Our clones show a similar evolution to the particles in Gomes et al. (2005), including the influence of the Kozai mechanism on the inclination distribution. We explore a toy model of the inclination distribution based on the i distribution presented in Figure 3 of Gomes et al. (2005); a Gaussian peak center, μ, at 35° instead of 0° with a width σ_i of 7°. This conservative parameterization removes the undetected low i tail present in the Brown (2001) model.

$$P(i) \propto \sin(i) \times \exp\left(\frac{-(i-\mu)^2}{2\sigma_i^2}\right) \tag{3.2}$$

The apparent eccentricity distribution of a population at large semi-major axis is strongly biased. Objects from the 5:1 resonance are typically only sufficiently bright for detection near pericenter, and if their pericenter is too large they may not be detectable even at pericenter. For this reason, we did not assume an eccentricity range for our model population based on another resonant TNO population but instead used an eccentricity range based on the range in our real detections and the bulk of the integrated clones (see Figure 3.4). We used a uniform eccentricity distribution from 0.50 to 0.62, or pericenters of ∼30 to 45 AU. The known objects have eccentricities in the range 0.55 to 0.62. While there may be a component of the 5:1 resonance with lower eccentricity due to the Kozai mechanism (suggested at the 5% level by our simulation results) or some other mechanism not present in our simulations, we present a minimum population estimate by not extending the model to eccentricities significantly lower than our detected TNOs.

Our cloned objects explore much of the resonance space, so we used the resonant libration characteristics of the clones to constrain the libration centers and amplitudes in our parametric model. The population model assumes 90% symmetric and 10% asymmetric resonators. We did not detect any asymmetric resonators and do not place strong constraints on their population fraction. We also calculated the range of libration amplitudes explored by the 5:1 resonators and included that in our orbital distribution model. The symmetric objects had their expected libration centers at 180° from Neptune, and an amplitude of $175^{\circ}{}^{+3}_{-5}$. The trailing island was centered at

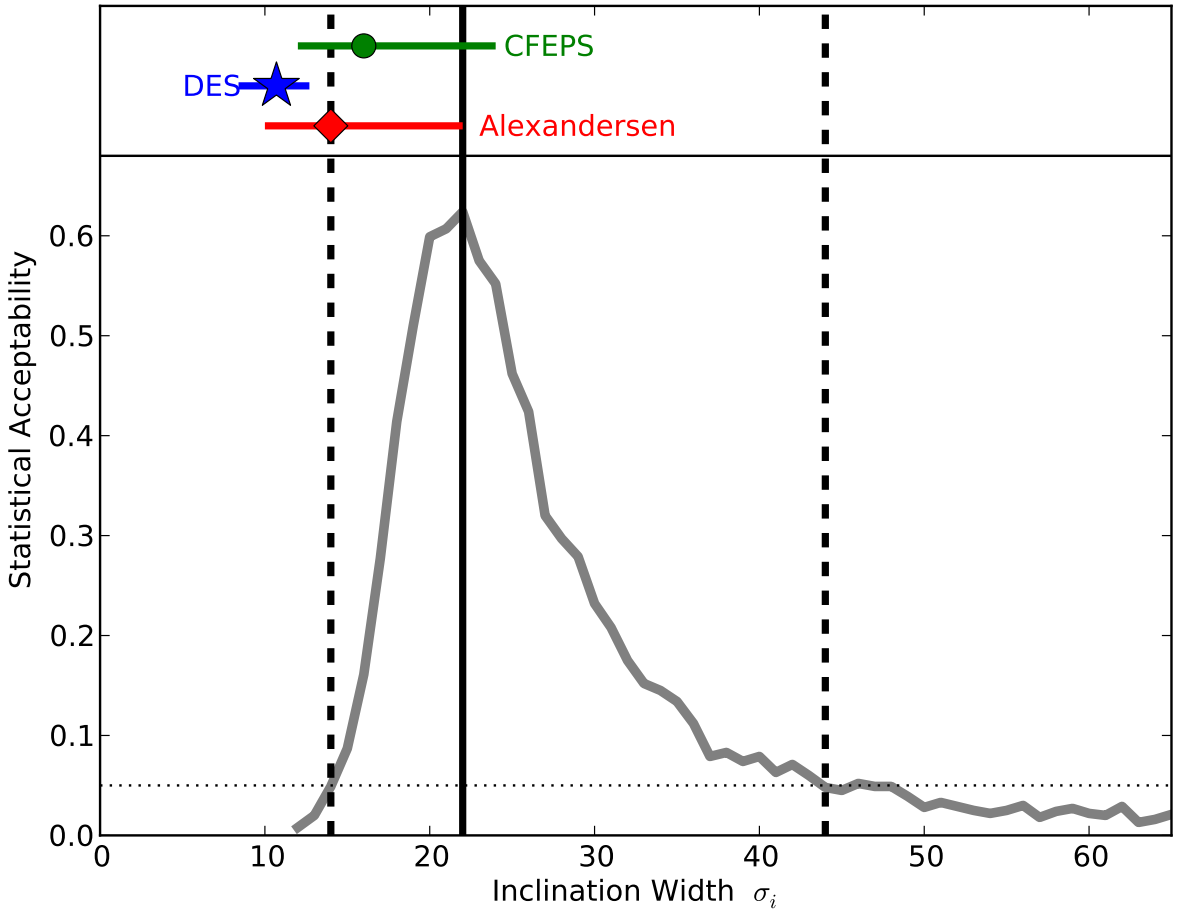

Figure 3.5 The acceptability of different inclination widths for the 5:1 resonance is shown for inclination widths from 5°–65°. The preferred inclination width is 22° (black solid line). The 95% confidence limits are $14° < \sigma_i < 44$ (black dashed lines). The Plutino inclination width is shown for comparison from Alexandersen et al. (2016) (red diamond, 95% confidence limits), Gladman et al. (2012) (green circle, 95% confidence limits), and Gulbis et al. (2010) (blue star, 68% confidence limits).

240° with an amplitude of $70°^{+20}_{-40}$, and the leading island was centered at 120° with an amplitude of $70°^{+20}_{-40}$. We calculated positions for each model object by drawing from a triangular distribution of the libration amplitude encompassing the libration amplitude range reported. An angle was randomly selected from within the object's libration range, instead of sinusoidally weighting the objects position. This gives a

closer approximation to the sawtooth pattern of the resonant angle seen in Figure 3.2. This angle was added to its libration center to give the current resonant angle, ϕ_{51}, for the model object. As described above, the resonance characteristics of the integrated clones were used to generate a representative sample of resonance angles.

The three additional orbital parameters (argument of pericenter, mean anomaly, and longitude of the ascending node) must fulfill the resonance condition. A detailed discussion of the resonance angles can be found in Murray-Clay & Chiang (2005). We selected the mean anomaly ($\mathcal{M}$) and the node (Ω) randomly, and calculated the necessary argument of pericenter (ω) using the resonant angle, ϕ_{51}. This condition required Neptune's position, $\lambda_N = \omega_N + \Omega_N + \mathcal{M}_N$, at the selected epoch. The resonance condition is:

$$\phi_{51} = 5\lambda - \lambda_N - 4\varpi \tag{3.3}$$

where $\varpi = \omega + \Omega$. This means that ω was calculated via:

$$\omega = \phi_{51} - \Omega - 5M + \lambda_N. \tag{3.4}$$

An absolute H magnitude distribution is needed in order to estimate the number of objects in the resonance. This distribution determines the number of objects in the population of each size. Our three 5:1 resonant objects have H_g of 6.0, 7.3, and 7.7 (see Table 3.3). Our population estimate only extends to $H_g = 8$, providing a more accurate population estimate for this sparsely sampled resonance than extrapolating to smaller sizes. $H_g = 8$ corresponds to an approximate diameter of 170 km assuming an albedo of 5% (Petit et al., 2011). A single power law with a slope of $\alpha = 0.8$ has been shown to be appropriate for the scattering objects to $H_g \sim 9$ (Shankman et al., 2013). A similar result for $H_B < 7.7$ was reported by Fraser et al. (2014), who found the 'hot' population had a bright end slope of $\alpha = 0.87$. We expect our objects to be similar to scattering objects, so we used a single power law with a slope of $\alpha = 0.8$ for our size distribution, and only estimate the population for $H_g < 8$. Because we only extended our population estimate over the range of our detected objects, a slightly steeper slope, as in Fraser et al. (2014), does not significantly impact our population estimate.

3.5.2 Population Estimate

With the assumptions described in the previous section, we made a population model for the 5:1 resonant objects. We used inclination width $\sigma = 22°$, the eccentricity range of 0.50-0.62, and symmetric fractions and libration amplitudes consistent with the clones, discussed above. This results in a minimum model-based population estimate for the 5:1 resonance.

We estimated the size of the underlying population of the resonance by using a survey simulator (Jones et al., 2006; Kavelaars et al., 2009). The pointings and depths of each survey field are provided to the simulator from the CFEPS ecliptic and high latitude blocks and the Alexandersen et al. (2016) survey. Analysis similar to Kavelaars et al. (2009) showed consistency between the real object detection and the model objects, once biased by the survey simulator. The survey simulator works by testing the detectability of each model object against the survey fields. Synthetic objects were drawn from the model until 3 tracked TNOs were 'discovered' by the survey simulator; the total number of objects drawn gives a possible population size. This process was repeated 6,000 times, and a range of population estimates were computed, shown in Figure 3.6.

We find that the 5:1 resonance contains 1900^{+3300}_{-1400} TNOs with $H_g < 8$ and $e > 0.5$ (95% confidence). This estimate is approximately the size of the Plutino population (Gladman et al., 2012) and possibly larger, shown in Figure 3.6. Our result is consistent with the 5:1 population from Gladman et al. (2012) based on a single detection; their population model assumed a narrower inclination distribution but extended the model to $0.35 < e < 0.65$. For our toy model with the inclination distribution drawn from a Gaussian centered at 35°, we find 2400^{+4000}_{-1800} objects in the 5:1 resonance with $H_g < 8$ and $e > 0.5$. We tested some additional model parameters to determine the extent of the model dependence of the population estimate. Changing the symmetric fraction from 10% to 30% resulted in a population estimate within 1% of our nominal model. Using the inclination distribution extremes (14° and 44°) gave population estimates 5% larger and 17% smaller, respectively. This outer resonance represents a significant reservoir of TNOs, regardless of the inclination distribution of the population.

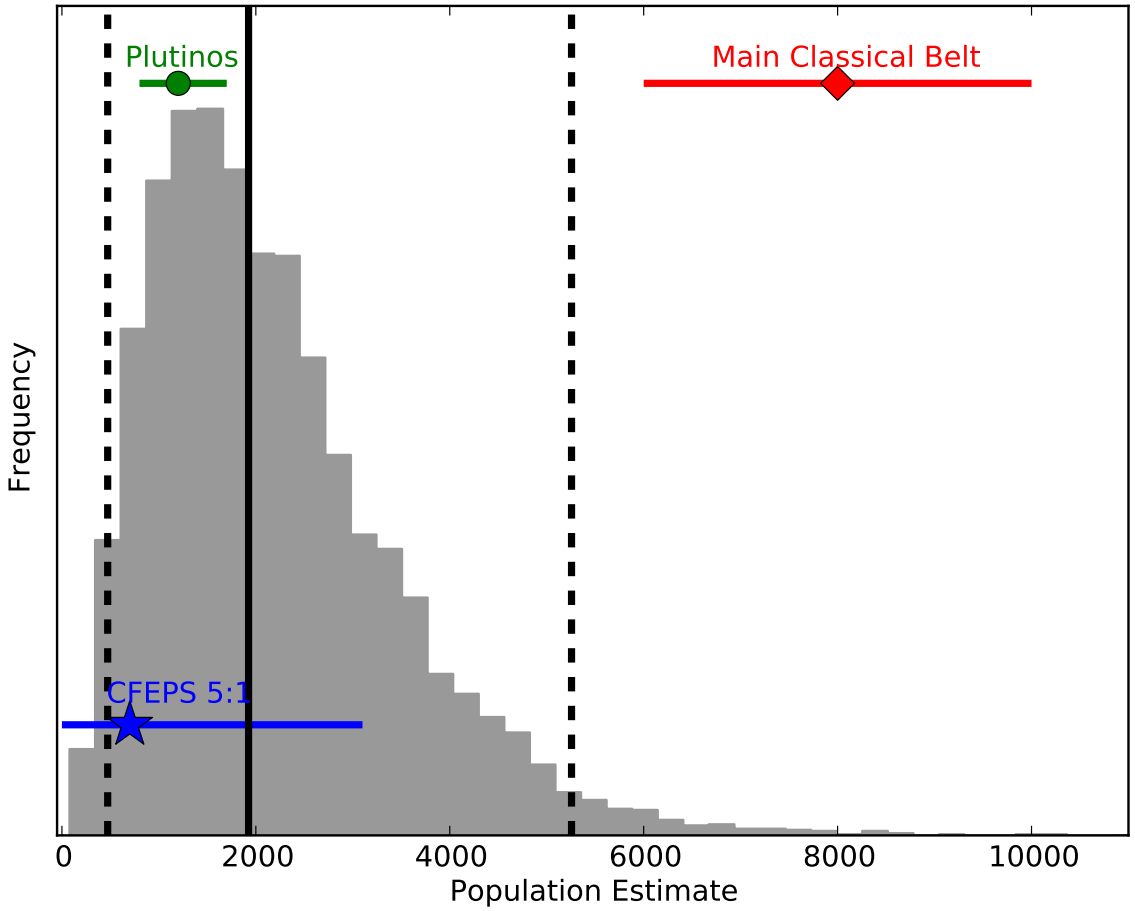

Figure 3.6 The histogram shows the number of intrinsic objects with $H_g < 8$ necessary in the 5:1 resonance in order for the surveys to have detected 3 objects. The wide range of acceptable values is due to the low number of detections, but the median population prediction is 1900 TNOs in the 5:1 resonance brighter than $H_g < 8$. The median value is shown by the bold black line, and the 95% confidence limits are shown in black dashed lines. The blue star shows the Gladman et al. (2012) 5:1 population estimate. For comparison, the population estimates (and 95% confidence ranges) for the Plutinos (green circle) from Gladman et al. (2012) and Main Classical belt (red diamond) from Petit et al. (2011) are shown.

3.6 Discussion

We have found three objects in the 5:1 resonance which appear to be resonance sticking objects, indicating the existence of a large population of temporary and long term

captures. In our integrations, we found that a significant fraction of the clones escaped the 5:1 resonance into the detached or scattering population on timescales of 10^8 to 10^9 years. Some of these objects were ejected, either inward or outward, but many remain non-resonant with semi-major axis values near the 5:1 resonance. We noted captures into the 6:1 and 7:1 resonances, as well as some additional resonances. We also identified cases where clones left the 5:1 resonance, entered a different resonance, escaped that resonance, and were recaptured into the 5:1 resonance. The instability in these resonances implies a regular exchange between the scattering objects and the outer resonances. A reliable estimate of capture efficiency from the scattering objects combined with stability lifetimes would determine the plausibility of different population mechanisms: a steady state population resupplied by the currently scattering objects, remnant long term captures from a past scattering event, or a non-scattering capture source. We suggest that the scattering objects are the 'source' of a resonance sticking 5:1 populations, and the nearby resonances with efficient resonance sticking (such as the 6:1 and 7:1 resonances) should also have large resonance sticking populations.

The detached object HL8k1, located just interior to the 5:1 resonance, may be a resonance diffusion object. This object is stable in its current location for the age of the Solar System. In the integrations of the clones of the resonant objects, we see an over-density of objects exiting the 5:1 and remaining near the resonance borders and just sunward of the 5:1 resonance. Some of these clones remain in this location for the rest of the simulation, so a diffusion out of the resonance could populate the region around HL8k1 where objects are stable. The detection biases against an object like HL8k1 are similar to those against the resonators; a first order population estimate for HL8k1-type objects is $\sim 1/3$ the 5:1 resonant population. Because of the extreme inclination of this object, we prefer the resonant population model with inclination not centered on the ecliptic for the comparison 5:1 population model. HL8k1 suggests the existence of a resonance diffusion population in a stable region of phase space and may be representative of a large, detached resonant diffusion population; in fact HL8k1 exhibits similar behavior to 2004 XR_{190} ("Buffy", Allen et al., 2006), with a semi-major axis just sunward of the 8:3 resonance.

In our model of the 5:1 resonance, we assume only eccentricities that are stable and in the range of those detected by current surveys. This limits our eccentricity range to 0.50-0.62. We find that Kozai cycling can result in resonant objects with eccentricities of 0.3-0.5 and high inclinations. We do not include these objects in the

model because they have very low detectability and, based on the clone integrations, likely represent ∼5% of the population. Because the surveys have low sensitivity to low e objects, we cannot rule out a low e population unrelated to Kozai, with a hot or cold i distribution. If objects with both low e (< 0.5) and low i ($< 15°$) were discovered in the 5:1, such objects might not be dynamically linked to the known 5:1 resonators and could require a different source population or capture mechanism.

We find that the 5:1 resonance is well populated, with 1900^{+3300}_{-1400} TNOs with $H_g < 8$. This supports the tentative prediction in Gladman et al. (2012) that the 5:1 resonance may be the most populous of all the known resonances. Alexandersen et al. (2016), using the CFEPS ecliptic blocks and their additional survey, found a 4:1 population estimate of 230^{+900}_{-220} and a 3:1 population estimate of 270^{+360}_{-180} for $H_g < 8$, significantly less populated than the 5:1. The 5:1 population estimate is larger than the CFEPS estimate of the Plutinos, which have the largest number of detected objects of any resonance. The 5:1 resonance is twice as far from the Sun as the 3:2 resonance, so a different population mechanism and source population are likely. The range of stable inclinations and eccentricities are larger in the 5:1, and it would appear, naively, that the phase space of the 5:1 resonance is significantly larger than the 3:2. A combination of increased phase space and resonance sticking lifetimes could result in this large 5:1 population.

The only other known TNO populations at semi-major axis near the 5:1 are other possible resonances, scattering objects, and some detached TNOs. Shankman et al. (2013) find that there are 10^4 scattering objects with $H_g < 8$ out to $a < 1,000$ AU. This means that the 5:1 resonance is ∼20% the size of the total scattering object population. Based on the semi-major axis distribution of the model used by (Shankman et al., 2013) and the total population estimate therein, we find that the scattering population with $H_g < 8$ between 85-95 AU is approximately 220 objects. The scattering objects have a density of ~ 22 objects per AU, so the 5:1 resonance, with a width of ∼2 AU containing ~ 2300 objects represents a significant over-density in this semi-major axis range.

3.7 Conclusions

Based on extensive tracking of four objects discovered by CFEPS, we have determined that three objects are in the 5:1 Neptune resonance. We have performed orbital integrations of these objects over the age of the Solar System, and it appears that

these objects are likely temporary captures, stable for $\sim 10^8$ years. These resonance sticking events can result in short or long term resonance. The fourth object is not resonant, but is in a stable location for the age of the Solar System, and its location relative to the 5:1 resonance suggests it is a resonance diffusion object.

The characteristics of the three resonant objects and the dynamical integrations were used to create a parametric model. We selected an inclination width, eccentricity and semi-major axis range, and the H magnitude distribution of the scattering objects. The inclination width that reproduced the inclinations of the three detected TNOs was larger than the Plutinos, suggesting a significantly dynamically hotter population. All of the resonant objects begin in the symmetric resonance, and some clones transition into the asymmetric islands. Approximately 5% of the simulated objects are affected by the Kozai mechanism which pushes some objects to low e and high i, but we exclude this small fraction of objects from our model for a population estimate.

We used a survey simulator to apply the survey biases to our model, and found that the resulting model detections resembled our real TNOs. The necessary size of the model in order to produce three detections gives a population estimate for the 5:1 resonance of 1900^{+3300}_{-1400} with $H_g < 8$ and $e > 0.5$. This significant population in the outer Solar System has implications for Solar System evolution as well as implications for other distant resonances because the 5:1 resonance appears to be populated by scattering objects sticking in the 5:1 resonance.

3.8 Acknowledgements

Based on observations obtained at the Gemini Observatory processed using the Gemini IRAF package, which is operated by the Association of Universities for Research in Astronomy, Inc., under a cooperative agreement with the NSF on behalf of the Gemini partnership: the National Science Foundation (United States), the National Research Council (Canada), CONICYT (Chile), the Australian Research Council (Australia), Ministrio da Cincia, Tecnologia e Inovao (Brazil) and Ministerio de Ciencia, Tecnologa e Innovacin Productiva (Argentina).

This research used the facilities of the Canadian Astronomy Data Centre operated by the National Research Council of Canada with the support of the Canadian Space Agency.

Based on observations obtained with MegaPrime/MegaCam, a joint project of

CFHT and CEA/IRFU, at the Canada-France-Hawaii Telescope (CFHT) which is operated by the National Research Council (NRC) of Canada, the Institut National des Science de l'Univers of the Centre National de la Recherche Scientifique (CNRS) of France, and the University of Hawaii.

Research supported by the Canadian National Science and Engineering Research Council (NSERC) Discovery Grant program.

Chapter 4

The structure of the distant Kuiper belt in a Nice model scenario

This chapter contains work submitted to the Astronomical Journal in June 2016. The end state of particles from a literature model were provided to me by Dr. Ramon Brasser. I performed the dynamical integrations, classifications, and analysis of the results. Dr. Samantha Lawler provided a contribution to the Kozai portion of the text as well as feedback on the manuscript. Cory Shankman designed the Fast Fourier Transform method that I implemented to classify resonant objects. I provided the classified model to Dr. Mike Alexandersen, who determined the list of synthetic detections using the survey simulator. Dr. JJ Kavelaars provided feedback on the results and manuscript.

The focus of this chapter is to use the detections from surveys to test a literature model of Solar System evolution. This model was produced independently of the survey teams, so agreement between this model and the detections indicates consensus on the orbital parameters and population sizes of TNOs. I determined that this model produces an accurate scattering population but does not produce the populated 5:1 resonance that I expect based on Pike et al. (2015) as described in Chapter 3.

4.1 Abstract

This work explores in depth the orbital distribution of minor bodies in the outer Solar System created as a result of a Nice model migration from the simulations of Brasser & Morbidelli (2013). This planetary migration through a planetesimal disk

between 29-34 AU reproduces a two-component inclination distribution of classical belt objects, as well as the orbital distribution of the scattering objects and distant resonant populations. From the 2:1 Neptune resonance and outward, the test particles analyzed populate the outer resonances with orbital distributions consistent with trans-Neptunian object (TNO) detections in a, e, and i. The relative populations of the simulated scattering objects and 3:1 and 4:1 resonators are also consistent with survey expectations, but the 5:1 resonance is severely underpopulated compared to expectations from survey results. The Brasser & Morbidelli (2013) Nice-model simulation produces a high inclination detached component beyond the 2:1 resonance, as observed in the outer Solar System. Scattering emplacement results in the expected orbital distribution for the majority of the TNO populations, however the origin of the large observed population in the 5:1 resonance remains unexplained.

4.2 Introduction

The trans-Neptunian objects (TNOs) populate the region beyond Neptune, and the specifics of their formation location and evolutionary history are the subject of much theoretical study. The idea of a quiescent belt, surviving beyond the giant planets, was clearly incomplete based on the orbital characteristics of the early TNO discoveries (Levison et al., 2008). Even the first known TNO, Pluto, has large eccentricity and inclination; the TNOs must have been dynamically stirred in the past (Malhotra, 1995). The TNO population has dynamically excited eccentricity and inclination distributions, and the objects extend out to large semi-major axes. In addition, the resonant populations are much larger than expected for a Kuiper belt population which experienced no dynamical stirring or scattering. The over-population of objects in resonance is an indicator of a previous dynamical instability affecting the outer Solar System (Malhotra, 1993, 1995; Hahn & Malhotra, 2005; Gomes et al., 2005; Levison et al., 2008).

The sub-populations in the Kuiper belt also hold clues to their evolutionary history. Some regions of the Kuiper belt have different physical properties; for example, the cold classical objects, with a less excited inclination distribution, have a steeper size distribution than the hot classical objects (Bernstein et al., 2004). The surface colors of TNOs are also correlated with their dynamics; different color distributions correspond to different dynamical sub-populations (e.g. Tegler et al., 2003). Brown et al. (2012) suggests that the surface colors of TNOs could be produced by forming

these objects interior to their present location and moving them outward to their current orbits. The outer Solar System population characteristics are complex and provide clues about the formation and evolution of the Solar System.

An acceptable model of Solar System evolution will reproduce these aspects of the TNO population. A dynamical instability of the giant planets can increase both the eccentricity and inclination of small bodies and capture a large number of TNOs into resonance. A slow migration of Neptune outward would sweep TNOs into mean motion resonances (Malhotra, 1995). This slow sweeping would pump up the eccentricity of captured TNOs without significantly altering their pericenter distances. The large binary fraction of some subpopulations of TNOs favors a slow or minimal migration because these binaries are likely to have been disrupted by more violent scattering interactions (Parker & Kavelaars, 2010). Smooth migration scenarios typically result in TNO populations which are not sufficiently dynamically excited in inclination, and the possibility of more granular and less smooth migration models have been explored (Hahn & Malhotra, 2005; Nesvorný, 2015b).

Thommes et al. (1999) suggested that the giant planets were dynamically unstable. The early incarnations of rapid planetary migration models are known as the 'Nice model' (Tsiganis et al., 2005; Morbidelli et al., 2005; Gomes et al., 2005). In this scenario, there is a large dynamical instability, such as Saturn and Jupiter crossing their 2:1 mean motion resonance, scattering Uranus and Neptune, which subsequently scatter small bodies, emplacing the TNOs and Oort cloud and causing the Late Heavy Bombardment. This scenario also results in capture of the Jupiter Trojan asteroids (Morbidelli et al., 2005). A more rapid planetary scattering event results in different characteristics of captured objects.

A detailed comparison of TNO detections and numerical simulation results requires a carefully observed Kuiper belt in addition to a well-sampled simulation. Several recent surveys of the Kuiper belt have attempted to provide TNO discoveries with known discovery biases (Kavelaars et al., 2008; Petit et al., 2011; Adams et al., 2014; Alexandersen et al., 2016; Bannister et al., 2016). These surveys characterize their discovery biases to facilitate comparison with population models.

This work explores the specific effects of the 'Nice' model migration on the TNO populations in more detail in the following sections. The predicted TNO population from the Nice migration simulation by Brasser & Morbidelli (2013) is tested against the real TNO detections from Kavelaars et al. (2008), Petit et al. (2011), and Alexandersen et al. (2016). The combination of real detections from the surveys and survey

simulator provides a powerful tool for comparing an external model to the survey detections. The simulation and test particle classification are discussed in Section 4.3. The characteristics of the initial planetesimal disk and an explanation of the survey simulator debiasing procedure are provided in Section 4.4. Section 4.5 presents the results of the classification and analysis, including comparisons of relative population size and parametric distributions of real TNOs and model particles. The discussion and conclusions are presented in Section 4.6.

4.3 Migration Model

Brasser & Morbidelli (2013) use a Nice model framework to populate the scattered disk and Oort cloud. This includes a dynamical instability following the removal of the gas in the Solar System's protoplanetary disk, after the last encounter between the ice giants. The planetary evolution track from Levison et al. (2008) 'Run A' was repeated, which starts with Neptune at 27.5 AU with an eccentricity of 0.3 and Uranus at 17.5 AU and an eccentricity of 0.2. Uranus migrates outward to ∼19 AU and Neptune migrates to ∼31 AU. Jupiter and Saturn experience some small evolution of their eccentricities, however their semi-major axes remain at 5 AU and 9.5 AU. This migration takes place over a time period of ∼ 100 Myr.

The model from Brasser & Morbidelli (2013) is examined here, referred to as the B&M simulation, to assess the accuracy of this model in producing the trans-Neptunian region. The TNO comparison population is from the CFEPS (Petit et al., 2011; Kavelaars et al., 2008) and Alexandersen et al. (2016) surveys. Using a model from a source external to the survey collaborations provides a useful test of the orbital distribution models created by the survey team. The goal of the initial B&M simulation was to populate the Oort cloud and scattered disk as a result of giant planet migration and subsequent evolution. Brasser & Morbidelli (2013) compared the relative size of these populations produced by the model, and found that the Oort cloud is 44^{+54}_{-34} times more populated than the scattered disk. This work focuses on the 'scattered disk' portion of the simulation, which is all objects beyond Neptune and interior to the Oort cloud (a distance cut of 3,000 AU was used).

The B&M numerical simulations for the scattered disk objects were run in two stages. The first stage is the numerical integration of the planetary migration described above with 30,000 massless test particles. The test particle initial locations were based on Levison et al. (2008), with $29 < a < 34$ AU, $e = 0.15$, and $i = 0$;

each test particle had unique position and velocity vectors. For the scattered disk component, after the planet migration was completed, all test particles beyond 3,000 AU were removed from the simulation. At this point, Uranus was forced outward 0.25 AU to its true position and the eccentricities of Uranus and Neptune were damped slightly. At the end of the simulation, Neptune is slightly beyond its true position, at 30.8 AU instead of 30.1 AU, however this was left unchanged to avoid disrupting resonant objects. Once the giant planet orbits were adjusted, the planets and test particles were integrated for the second stage, an additional 3.8 Gyr with SWIFT RMVS3 (Levison & Duncan, 1994). Because of significant scattering loss, after 1 Gyr and 3.5 Gyr, the remaining test particles were cloned three times to ensure a sufficiently well-sampled Kuiper belt. The results from the end state of the 3.8 Gyr B&M simulations are utilized in this work.

4.3.1 Additional Integrations

The end state planet and test particle positions from the B&M simulation were integrated in order to determine dynamical classifications. Additional integrations were necessary because resonance classification requires more frequent output than the previous full simulation in order to conclusively classify the test particles. The Sun, Jupiter, Saturn, Uranus, Neptune, and test particle end states from the previous simulation were provided as input for SWIFT RMVS4 (Levison & Duncan, 1994). The particle positions were recorded every 300 years to ensure sufficient sampling of the resonant angle. During the 30 Myr integration, the particles between $20 < a < 160$ AU were recorded, to focus on the classical Kuiper belt region as well as some of the distant resonances.

Neptune's final semi-major axis from the B&M simulations was $\sim$0.8 AU farther from the Sun than the true position of Neptune. This results in a slight outward shift in the outer Solar System structure, but otherwise the dynamics of both the outer Solar System minor bodies and the giant planets remains unchanged. After the simulations completed, the semi-major axes of all objects in the B&M simulation were adjusted to correspond with their locations if Neptune's semi-major axis were identical to the real position, using a scale factor of 30.047/30.8. This adjustment was done to facilitate direct comparison with the Solar System, and for the remainder of this work, the positions discussed for Neptune, the test particles, and the mean-motion resonances in the simulations are the same as in the real Solar System today.

4.3.2 Particle Classifications

The subpopulations determined here are compared with survey detections from Kavelaars et al. (2008), Petit et al. (2011), and Alexandersen et al. (2016), so a classification scheme consistent with those survey classifications is used (from Gladman et al., 2008). Figure 4.1 shows a plot of all classified test particles. The primary goal is to describe the behavior of the test particles at the start of the extended simulations, to characterize the model 'end state.'

A classification of resonance requires an oscillation of the resonant angle, ϕ_{pq}, over time, where p and q are integers, and ϕ_{pq} describes the p:q mean-motion resonance. Each particle whose semi-major axis is within 1.5 AU of a Neptune resonance location had the relevant resonant angle computed:

$$\phi_{pq} = p\lambda - q\lambda_N - (p-q)\varpi. \tag{4.1}$$

The particle mean longitude is $\lambda = \Omega + \omega + \mathcal{M}$, Ω is the longitude of the ascending node, ω is the argument of pericenter, and the longitude of perihelion is $\varpi = \Omega + \omega$. λ_N refers to the mean longitude of Neptune. If ϕ_{pq} oscillates instead of circulating, then the test particle is resonant.

Diagnosing resonance based on a visual inspection is straightforward, but an automated detection method is more complicated. However, on such a large set of test particles, an automated detection method is required. A spectrogram analysis was used on a series of windows to identify oscillation in ϕ_{pq} over time (Shankman et al., 2016a). The behavior of ϕ_{pq} in overlapping windows of $5{\times}10^6$ years was analyzed using a fast Fourier transform (FFT). If a particle's ϕ was resonant for all windows it was classified as stable; unstable particles only displayed oscillations in a subset of windows. If an object was resonant, the libration amplitude (maximum to minimum ϕ_{pq} oscillation) and libration center (median value of ϕ_{pq}) of the particle were calculated. Resonant particles were also tested for Kozai oscillation (Lidov, 1962; Kozai, 1962) with the spectrogram method on the argument of pericenter, ω, to determine if the test particle ω oscillated instead of circulating, as in Chiang & Jordan (2002). (See Section 4.5.6 for details on the analysis of Kozai resonators.)

Once resonant objects are classified, the next diagnostic check is for scattering objects. The definition of 'scattering' objects is intended to refer to objects that are currently scattering, instead of the 'scattered' classification which refers to objects that were scattered in the past (Gladman et al., 2008). In this simulation all test

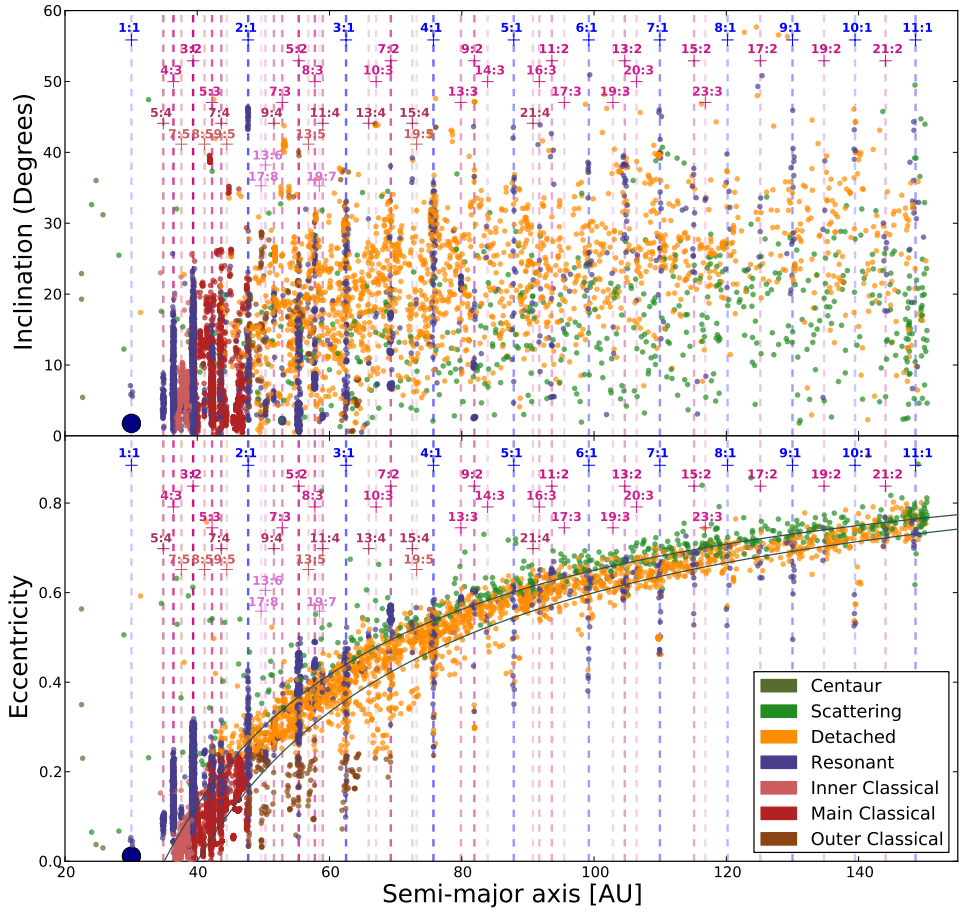

Figure 4.1 Test particle inclination, i, and eccentricity, e, distributions with semi-major axis, a, of the end state of the B&M model. The dashed lines mark resonances where more than two test particles are found; these resonances are listed in Table 4.2. The opacity of the dashed lines scales with the number of particles in the resonance. The large number of inner and main classical objects is apparent. The outer classical objects are consistent with emplacement through resonance dropout, similar to the slightly larger e detached objects. The solid lines indicate specific pericenter locations, q of 35 and 40. Neptune is indicated by the large dark blue circle.

particles beyond 34 AU, the original extent of the implanted disk, must have been scattered by Neptune. 'Scattering objects' specifically refers to the dynamically unstable objects in the simulation, particles that experience a change in $a \geq 1.5$ AU in the first 10^7 years of the additional integration.

If a particle is not currently scattering or resonant, then the particle is classified based on its current a, e, and i values. Objects are classified as main classical if they are between the 3:2 and 2:1 resonance, 39.4 AU – 47.7 AU, and have eccentricities $e < 0.24$. Inner classical objects are found between Neptune and the 3:2 resonance, 30.04 AU – 39.4 AU with eccentricities $e < 0.24$. Test particles beyond the 2:1 resonance at 47.7 AU in the same eccentricity range are classified as outer classical objects. Detached objects are particles beyond Neptune with $e > 0.24$. Objects that exhibit semi-major axis evolution and have $a < 30$ AU are classified as centaurs.

4.4 Comparing the B&M Model to the Solar System

4.4.1 Biasing the Model with a Survey Simulator

To facilitate direct comparison of the orbital distributions from the end state of B&M to real TNO detections, an observational bias is applied to the B&M simulation particles using a survey simulator. The survey simulator uses survey detection characteristics (pointings, detection efficiencies, tracking efficiencies, etc.) to determine which input model objects would have been detected by the survey (Kavelaars et al., 2009). The B&M test particles are compared to the detections from the CFEPS ecliptic (Petit et al., 2011) and high latitude (Kavelaars et al., 2008) surveys as well as the survey by Alexandersen et al. (2016). These surveys provide the well characterized survey detection and tracking efficiencies needed for the survey simulator input. In all plots where B&M simulation particles are compared to real TNOs, the TNOs are the characterized detections from these surveys. To determine the acceptability of the B&M particles as a model of the populations, the survey simulator-biased test particles are compared to the real TNO detections.

The subcomponents of the B&M simulation results are also directly compared to the CFEPS L7 model, the orbital element distributions and absolute populations of different TNO components based on debiasing CFEPS (Petit et al., 2011). The L7 model is consistent with the detections, but is not uniquely consistent; for example, an equally consistent model could contain additional populations at very large pericenters entirely undetectable by the surveys. As a result, agreement between the B&M simulation and the L7 model implies that the B&M simulations must be consistent

with the detections, while disagreement with the L7 model does not necessary require that the B&M simulation results are inconsistent with real detections.

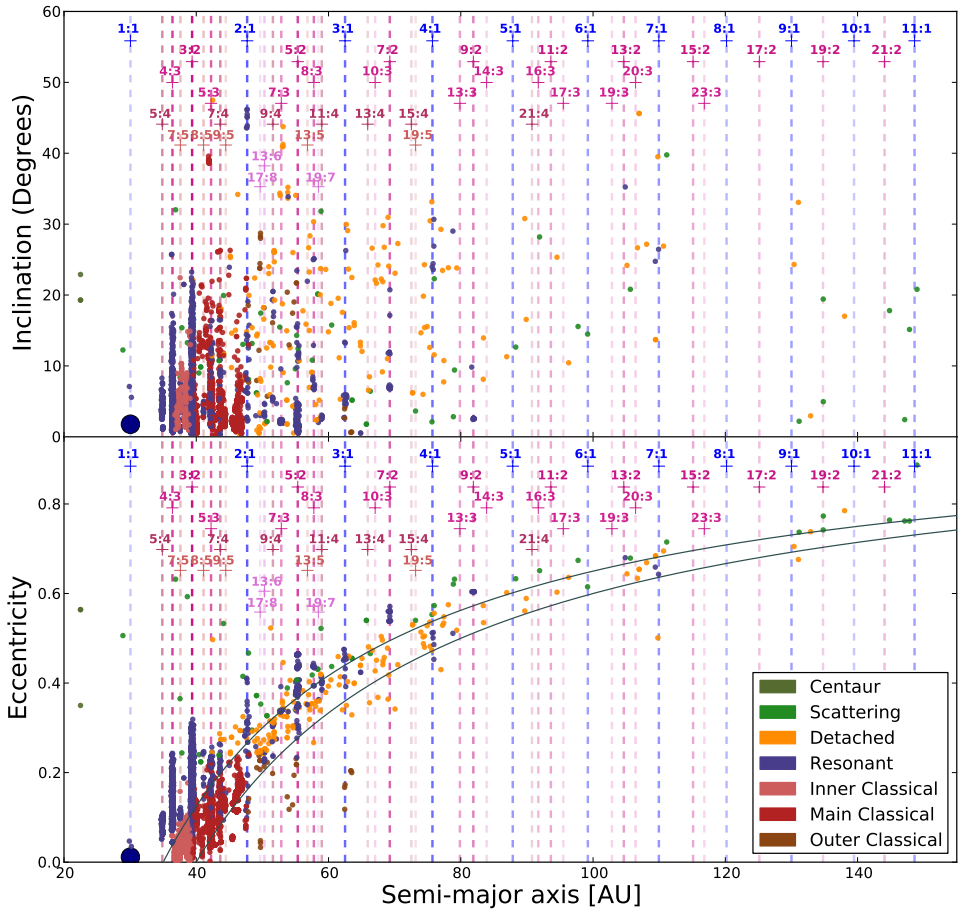

Figure 4.2 Similar to Figure 4.1, inclination, i, and eccentricity, e, distribution with semi-major axis, a, of the B&M simulation end state biased using a survey simulator. The objects shown are 30,000 particles which were 'detected' by the survey simulator using the Kavelaars et al. (2008), Petit et al. (2011), and Alexandersen et al. (2016) survey pointings with H magnitudes randomly assigned from a SPL H-magnitude distribution with $\alpha = 0.9$. This plot includes only detections with $H_g < 8$, which roughly corresponds to 170 km in diameter. The significant selection effects of TNO surveys are apparent; the inner classical and close resonances are much easier to detect compared to more distant populations. The knee and divot distributions show qualitatively similar detection biases.

The B&M simulation results were used as the input orbital model for the CFEPS survey simulator. Conducting a survey simulator analysis of a simulation output requires a large number of orbit samples. The simulation particles were cloned, preserving a, e, i, and in the case of resonant objects, the resonant angle (ϕ), while randomizing the position angles (ω, Ω, and $\mathcal{M}$). This cloning ensures a sufficient number of simulated detections; objects are randomly drawn until a larger sample than the known TNOs is 'detected' to ensure the parameter space is sufficiently well sampled.

In order to determine the detectability of the B&M orbital model, an absolute magnitude, H, distribution for the particles is assumed. This is a proxy for object size, which is not directly measurable for unresolved objects because albedos are typically unknown. H distributions are typically parameterized as an exponential, equivalent to a single power law (SPL) in diameter; in differential form the SPL has a slope of α:

$$dN/dH_g \propto 10^{\alpha H_g}. \tag{4.2}$$

Shankman et al. (2013, 2016b) describes a broken power law by joining two power laws with different slopes, $\alpha_{\rm bright}$ and $\alpha_{\rm faint}$, at a specific magnitude, $H_{g-{\rm transition}}$. In addition to the change of slope, they also propose a sudden drop (a 'divot') in number density after the transition, parameterized as the contrast, c. (A contrast of one is referred to as a 'knee' in the literature.) The simulation particles are assigned an absolute brightness, H_g from three different size distributions from the literature. These are: an SPL with a slope of $\alpha = 0.9$ as in Gladman et al. (2012); a knee distribution with $\alpha_{\rm bright} = 0.87$, $\alpha_{\rm faint} = 0.2$, and $H_{g-{\rm transition}} = 8.35$ as in Fraser et al. (2014) converted to g using $g - r$=0.65 from Petit et al. (2011); and a divot distribution with $\alpha_{\rm bright} = 0.8$, $\alpha_{\rm faint} = 0.5$, $H_{g-{\rm transition}} = 9.0$, and a contrast $c = 6$ as in Shankman et al. (2013). The B&M particles were input into the CFEPS survey simulator to determine which of the B&M objects would have been detected in the surveys. For the majority of the B&M populations the choice of size distributions had no impact on the conclusions, so for these populations only the knee distribution is presented. An example of the 'detected' simulation objects is shown in Figure 4.2. The selection biases which complicate TNO population studies are apparent when comparing Figure 4.1 and Figure 4.2.

The biased simulation results reflect the detectability of different populations. The

fraction of detached objects detected is significantly smaller than other populations, because of their large pericenters. The closest objects dominate the simulated detections. The choice of size distribution model affects the expected number of detections roughly as a function of perihelion distance. The SPL produces more small object detections per each large object, so for the same number of simulated detections, a SPL distribution results in more low-a and large-H detections, while a knee or divot distribution is more likely to have larger-a and low-H detections. The survey simulator biased results for several resonant subpopulations are presented in Section 4.5.

4.4.2 Initial Disk Mass

Once a size distribution is assigned, the mass of the planetesimal disk is determined. For the knee distribution, because of the shallow slope after m_g=8.35, the objects above the knee effectively contain all of the mass. Assuming an albedo of 5%, m_g=8.35 corresponds to an object diameter of 160 km. For 30,000 particles above the knee in the size distribution up to 2400 km diameter (∼Pluto), assuming a density of 1.5 g/cm^3, the mass of the planetesimal belt is 3.1×10^{23} kg. Because of the cloning during the simulation, the initial planetesimal disk is increased by a factor of 9, so the starting mass is 3×10^{24} kg, ∼half an Earth mass, $M_\oplus$. The planetesimal belt can be scaled up to match the number of starting particles needed to produce the survey detections; for the well-modeled populations this is a factor of 5-10 (see Section 4.5.3), which indicates a starting disk mass of 2-5 $M_\oplus$ for the B&M simulation. Nice-model migrations typically require disks of $\sim$ 20 $M_\oplus$ (Nesvorný & Morbidelli, 2012) to 35 $M_\oplus$ (Levison et al., 2008) in order to cause migration. However, the B&M simulation begins after the first instability, and a factor of ∼10 removal of the disk mass is consistent with the rapid decay of the mass in a Nice-model scenario (Booth et al., 2009).

4.5 Results: Populations of the Outer Solar System

Using the methods described in Section 4.3.2, the end-state orbits of the test particles in the B&M simulations were placed into orbital classes. In this section, several Kuiper belt sub-populations are compared to real object distributions to test how well the

B&M model represents the Kuiper belt as a whole. The sub-populations discussed in detail include the main classical objects (section 4.5.1), the 5:1 resonators (section 4.5.4), 2:1 resonators (section 4.5.5), large-a resonators (section 4.5.5), and scattering objects (section 4.5.7). The signatures of libration island capture (section 4.5.5) and the Kozai mechanism (sections 4.5.6 and 4.5.6) are also explored. The full population statistics for the B&M model are summarized in Table 4.1 and the model objects' orbital distribution is plotted in Figure 4.1.

Table 4.1 Test Particle Classifications

Classification	Number of Particles	Fraction of Total
Resonant	3,910	42%
Inner Classical	871	9%
Main Classical	1,943	21%
Outer Classical	181	2%
Scattering	535	6%
Detached	1,921	21%
Centaurs	5	0.05%
Total Particles	9,366	100%

4.5.1 Characteristics of the Main Classical Belt

The main classical belt members of the end state of the B&M model, between the 3:2 Neptune resonance and the 2:1 Neptune resonance with $e < 0.24$, exhibit a two component inclination distribution. The inclinations of the test particles in this region of the B&M simulation strongly resemble the dynamically hot and cold classical belt distributions observed in the Kuiper belt. The initial state of the B&M simulation was 0° inclination and e=0.15 for all test particles. A cold belt resulting from scattering simulations was predicted by Levison et al. (2008) as a result of damping Neptune's eccentricity with particles trapped in resonance, however their simulations did not have sufficiently large number of test particles captured in the classical belt to test this hypothesis. The higher resolution sampling available in the B&M model confirms this prediction by Levison et al. (2008).

The B&M simulation clearly shows a two component inclination distribution in the classical region (see Figure 4.3). Inclination distributions have been found to be well modeled using the distribution from Brown (2001). The more general equation

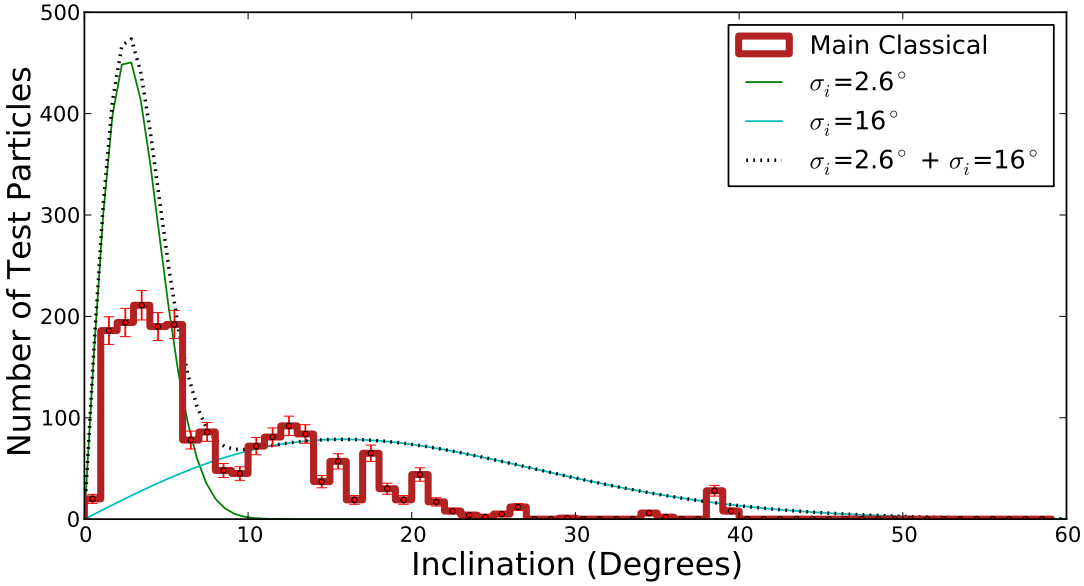

Figure 4.3 The bold red histogram shows the main classical B&M test particles between the 3:2 and 2:1 Neptune resonances with uncertainties calculated from the number of objects in the bin. There are clearly two components to the inclination distribution. The green and cyan lines show inclination distributions from Equation 4.3 with σ_i of 2.6° and 16° respectively, weighted to match the relative population sizes determined by CFEPS (Petit et al., 2011). The black dotted line shows the sum of the two inclination components.

includes a peak shift, μ, as well as the width, σ_i (Gulbis et al., 2010; Pike et al., 2015):

$$P(i) \propto \sin(i) \times \exp\left(\frac{-(i-\mu)^2}{2\sigma_i^2}\right). \tag{4.3}$$

In Figure 4.3, the B&M inclination distribution is shown, as well as the three theoretical inclination distributions from Equation 4.3: one with hot parameters σ_i of 16° ($\mu = 0°$), one with cold parameters σ_i of 2.6° and the sum of the two. These are the inclination widths of the real cold and hot classicals as found by Petit et al. (2011). The relative size of the two components is scaled to match the CFEPS ratio. Figures 4.3 and 4.4 include the preferred inclination widths and fractions from the CFEPS model.

The Anderson-Darling static (AD, Anderson & Darling, 1954), a weighted version of the Kolmogorov-Smirnov test, rejects the real object detections as being drawn from the biased B&M simulation, but the result of a multi-component inclination

distribution from an initial population without inclinations should be investigated further. The B&M simulation under-produces the cold classical objects compared to the hot population; this is evident from the much higher peak of the combined inclination model in Figure 4.3. The hot population is not quite as dynamically excited as the CFEPS model distribution, however the B&M objects exhibit a similar shape to the CFEPS model inclination distribution. The lack of a high quality match in the inclination distributions should not be interpreted as a failure of the B&M model; matching the two-component general structure should be interpreted as a success of the B&M model as a higher quality match could be produced by tuning starting conditions.

The cumulative eccentricity distributions of the B&M simulation as well as the CFEPS model and detections are shown in Figure 4.4. The eccentricity distribution of the B&M particles with lower inclinations is more excited than real detected TNOs by a factor of ~ 2, but there are a significant number of particles with both low eccentricity and low inclination in the B&M simulation. The AD statistic rejects the eccentricity distribution of the detections as being drawn from the survey simulator biased B&M simulation. The hotter e-distribution in the B&M model is likely a result of the large initial e values of the test particles. These starting eccentricities are hotter than is typically assumed in a proto-planetesimal disk, and this likely resulted in a classical region with hotter eccentricities.

A two component inclination model is necessary to represent the main classical B&M simulation particles in spite of the initial test particle inclinations of zero. The CFEPS detections are inconsistent with this model, however adjusting the initial eccentricity distribution of the simulation should result in a larger dynamically cold population in both eccentricity and inclination. The eccentricity of the B&M particles is too broad, and these large-e particles likely experienced more energetic scattering. Although the inclination distribution is statistically rejectable by the detections, a tuning of the starting planetesimal disk could produce acceptable hot and cold main classical populations. This style of scenario was investigated by Nesvorný (2015a,b), who finds that a slow migration rate produces the inclinations of the hot component of the classical belt, and the 'kernel' of the cold main classicals can result from jitter or jumping during Neptune migration, but requires the presence of a primordial cold classical population. It is significant that for the B&M model relatively dynamically cold TNOs were emplaced during the B&M Neptune migration and not formed in situ as has been previously suggested (Brown, 2001; Batygin et al., 2011); this suggests

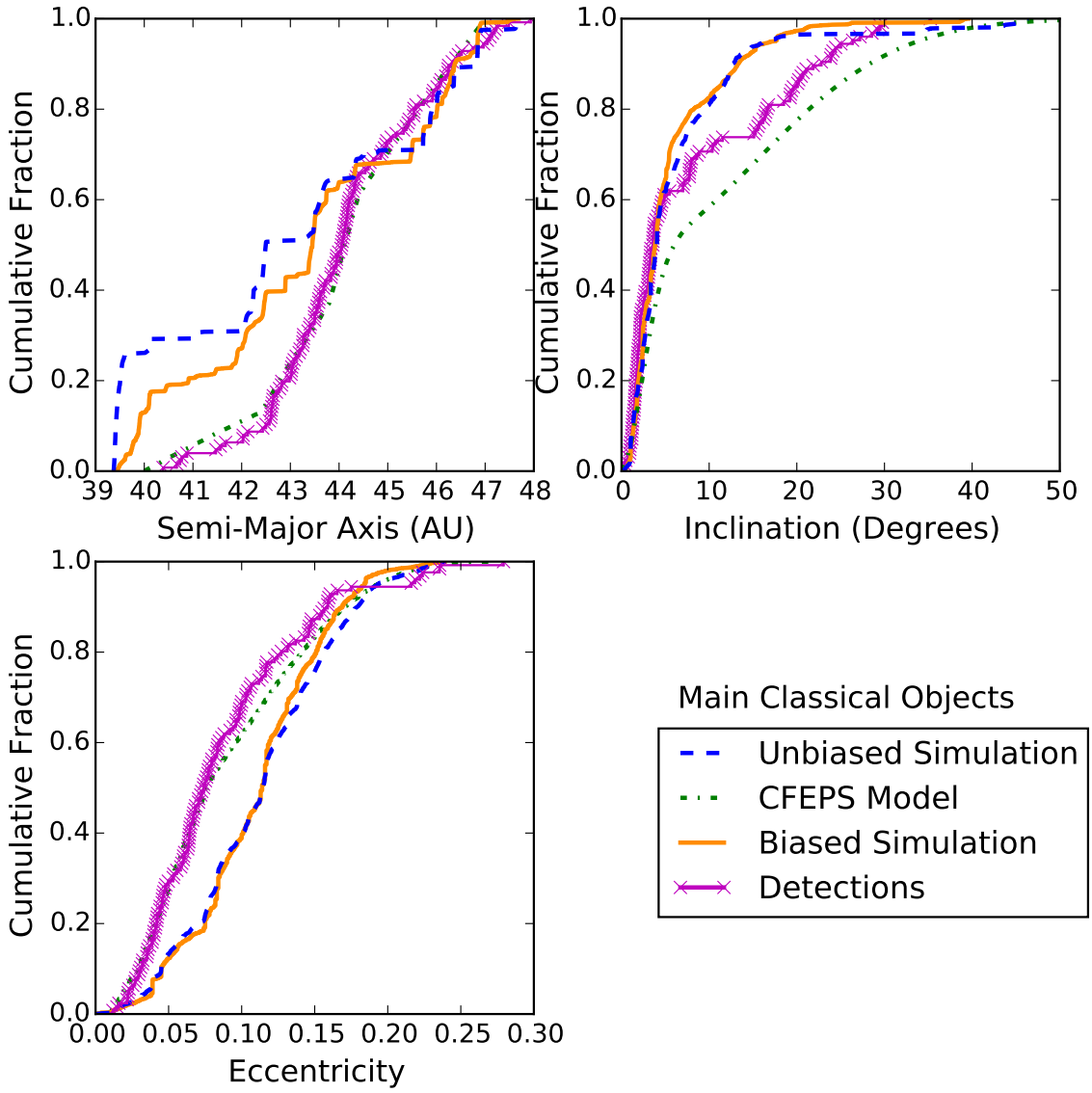

Figure 4.4 Cumulative distributions of the orbital elements of the main classical objects from the B&M model (blue dashed). The B&M model has been biased using the survey simulator (orange). The CFEPS model (green dash-dotted) and detections (magenta 'x') are also shown. The B&M model and the CFEPS model can be directly compared, as can the biased B&M model and the real TNO detections. While the shape of the i-distribution is good, the biased B&M model under-predicts low-i objects. The e-distribution of the B&M model is hotter than the detections.

that if a primordial dynamically cold population survived in this region it would at least be contaminated as a result of object emplacement during planetary migration.

4.5.2 Resonant Test Particles

The resonant particles comprise a significant fraction, 42%, of the B&M simulation. The resonant component is enhanced relative to the Solar System as the model inner resonances are overpopulated. This analysis of B&M resonant test particles focuses on resonances beyond the main classical belt, including the 2:1 resonance. The orbital distribution of the B&M resonant particles at smaller semi-major axes, such as the 3:2, 4:3, and 5:4, are unlikely to represent the real object distributions because of the initial B&M simulation design. This is likely a result of the large eccentricities of disk particles before scattering, which results in some unrealistic sweeping capture. However, many of the more distant resonant populations in the B&M simulation provide an excellent match to observations, as these resonances are populated by captured scattering objects.

The resonance occupation at the end state of the B&M simulations is presented in Table 4.2. All resonances with more than 2 particles are included, however resonances with fewer than ~ 10 particles are likely not well sampled enough to provide a statistically robust comparison population for the real TNO detections. The number of test particles in each resonance is reported, as well as the fraction classified as 'stable'; this requires that the test particle be resonant for the entire classification integration of 30 Myr. Unstable resonant particles are resonant for a minimum of 5 Myr. To assess the B&M simulation, these resonant B&M populations must be compared to debiased survey results from the literature, as well as biased using a survey simulator for comparison with real resonant object detections.

Table 4.2: Resonance Occupation

Resonance p:q	Semi-Major Axis (AU)	Number of Test Particles	Fraction Stable
1:1	30.05	4	100%
5:4	34.87	64	100%
4:3	36.40	588	100%
7:5	37.60	20	100%
3:2	39.37	1640	99%
8:5	41.10	17	100%
5:3	42.24	217	100%
7:4	43.63	67	100%
9:5	44.46	5	100%
2:1	47.70	111	97%
17:8	49.66	4	100%
13:6	50.31	17	100%

Continued on next page

Table 4.2 – *Continued from previous page*

Resonance *p*:*q*	Semi-Major Axis (AU)	Number of Test Particles	Fraction Stable
9:4	51.59	30	100%
7:3	52.86	39	100%
5:2	55.35	337	99%
13:5	56.81	5	100%
8:3	57.78	109	100%
19:7	58.47	3	100%
11:4	58.98	24	100%
3:1	62.50	77	85%
13:4	65.93	4	100%
10:3	67.05	3	100%
7:2	69.26	137	100%
15:4	72.53	4	100%
19:5	73.17	3	100%
4:1	75.71	70	80%
13:3	79.86	22	100%
9:2	81.90	55	98%
14:3	83.91	3	66%
5:1	87.86	19	84%
21:4	90.76	4	75%
16:3	91.72	9	77%
11:2	93.62	15	100%
17:3	95.50	3	0%
6:1	99.21	16	75%
19:3	102.85	3	66%
13:2	104.65	20	60%
20:3	106.43	4	75%
7:1	109.95	21	66%
15:2	115.13	14	92%
23:3	116.83	3	100%
8:1	120.19	7	28%
17:2	125.15	6	66%
9:1	130.01	16	62%
19:2	134.78	4	50%
10:1	139.47	4	50%
21:2	144.08	8	25%
11:1	148.62	15	40%

4.5.3 Comparing Population Sizes: Resonant and Scattering Objects

A successful model of planetary migration should reproduce the relative population sizes of the Kuiper belt resonances. The B&M simulation population ratios are pre-

sented in two ways in this section. In Table 4.3, the end state B&M populations are compared to published debiased literature population estimates. The 'L-Scale Factor', literature scale factor, in this table shows the factor the simulation would need to be increased by in order to match the literature estimate, and the uncertainty in the literature population estimate is translated into the scale factor uncertainty. For Table 4.5, the B&M model is biased using the survey simulator and compared to the number of real TNO detections of the surveys. Each population was analyzed separately and population estimates were calculated; these estimates have been divided by the number of objects in the model of that resonance. The 'B-Scale Factor', or biased scale factor, is the median number of times the model of that resonance must be sampled in order to produce the number of real detections listed, with 95% confidence intervals from the population estimate distributions. These scale factors indicate the factor by which the initial disk would have to be increased in order to result in the appropriate population size. The initial disk particles have a total mass of $\sim$0.5 $M_\oplus$ (see Section 4.4.2); multiplying this initial mass by the scale factor indicates the size of the initial disk necessary to produce the population. In each table, when the populations have similar scale factors to each other this indicates that these populations are produced consistently in the B&M model.

The population sizes of the B&M model sub-components are compared to population estimates of the resonances from carefully characterized surveys (Kavelaars et al., 2008; Petit et al., 2011; Alexandersen et al., 2016; Bannister et al., 2016). The population estimates (Gladman et al., 2012; Pike et al., 2015; Alexandersen et al., 2016; Volk et al., 2016) were calculated by creating a parametric model of the resonance, then using the survey simulator to forward bias the model to statistically compare it to the observations. (See Gladman et al. (2012) or Volk et al. (2016) for a detailed explanation of the paramaterization.) The size of the underlying population necessary to generate the number of detections in the survey is the estimated size of the population. The population estimates for many resonances explored by these surveys are summarized in Table 4.3.

As discussed previously, the B&M simulation was too effective at populating resonances interior to the classical Kuiper belt compared to those beyond the 3:2 (see Table 4.3). Most of the resonances are populated by captured scattering objects, but these low-a resonances include a component captured by resonance sweeping. The initial planetesimal disk extended to 34 AU with $e = 0.15$, contrary to expectations about the real proto-planetesimal disk, as disk particles are expected to have low

Table 4.3 Literature Estimates of Resonant Populations from Surveys

Resonance	a	B&M Simulation Population Estimate		Survey; Source
$p:q$	(AU)	L-Scale Factor[a]	N($H_g < 8$)	
1:1	30.05	2.5^{+10}_{-2}	10^{+40}_{-9}	Alexandersen et al. (2016)[b]
5:4	34.87	$0.2^{+1.2}_{-0.18}$	10^{+60}_{-9}	CFEPS; Gladman et al. (2012)
4:3	36.40	$0.2^{+0.2}_{-0.16}$	70^{+100}_{-50}	CFEPS; Gladman et al. (2012)
3:2	39.37	$0.8^{+0.3}_{-0.3}$	1200^{+500}_{-400}	CFEPS; Gladman et al. (2012)
		$0.7^{+0.3}_{-0.2}$	1100^{+400}_{-300}	Alexandersen et al. (2016)
		$0.6^{+0.2}_{-0.2}$	900^{+330}_{-270}	CFEPS+OSSOS; Volk et al. (2016)
5:3	42.24	6^{+6}_{-3}	450^{+470}_{-280}	CFEPS; Gladman et al. (2012)
7:4	43.63	20^{+30}_{-10}	300^{+400}_{-200}	CFEPS; Gladman et al. (2012)
2:1	47.70	10^{+6}_{-7}	340^{+200}_{-220}	CFEPS; Gladman et al. (2012)
		11^{+7}_{-5}	360^{+230}_{-180}	CFEPS+OSSOS; Volk et al. (2016)
7:3	52.86	8^{+20}_{-7}	320^{+760}_{-270}	CFEPS; Gladman et al. (2012)
5:2	55.35	3^{+4}_{-2}	1100^{+1400}_{-700}	CFEPS; Gladman et al. (2012)
		2^{+2}_{-1}	770^{+680}_{-420}	CFEPS+OSSOS; Volk et al. (2016)
3:1	62.50	5^{+12}_{-4}	340^{+800}_{-290}	CFEPS; Gladman et al. (2012)
		3^{+4}_{-2}	220^{+270}_{-150}	Alexandersen et al. (2016)
4:1	75.71	$1.3^{+5.8}_{-1.3}$	80^{+360}_{-80}	Alexandersen et al. (2016)
5:1	87.89	120^{+210}_{-90}	1900^{+3300}_{-1400}	CFEPS; Pike et al. (2015)

[a]The 'L-Scale Factor' (literature scale factor) indicates how much the B&M simulation (with $H_g < 8.35$) must be scaled up to match the population estimates (Population Estimate scaled to 8.35 ÷ Number of B&M model objects).
[b]Population estimate is for the stable Neptune Trojans, as all of the B&M test particles in this resonance are stable.

eccentricities unless shaped by shepherding planets. The starting conditions for Neptune in the B&M simulation placed the 5:4 resonance at 32 AU and the 4:3 resonance at 33 AU before planetary migration. The 3:2 resonance was at 36 AU, just beyond the original extent of the implanted disk, but the test particles had sufficient eccen-

tricity to reach an apocenter of 39 AU. The B&M 5:4, 4:3, and 3:2 resonances are the only resonances that include a significant number of particles swept into resonances from an unrepresentative disk in addition to capture from scattering particles, so these populations are not representative of the real TNOs.

The number of objects in the B&M resonant populations (2:1, 7:3, 5:2, 3:1, 4:1) and the population estimates from Gladman et al. (2012), Volk et al. (2016), and Alexandersen et al. (2016) are consistent. The L-scale factors for these populations in Table 4.3 are consistent with each other and additionally agree with the survey results from Gladman et al. (2012) and Volk et al. (2016) that the 5:2 resonance has a large population.

Table 4.5 Populations from the B&M model biased using a survey simulator. The knee H-distribution is presented because the effects of different distributions are minimal.

Resonance p:q	a (AU)	B&M/Survey B-Scale Factor[a]	Survey Detections[b]
1:1	30.05	4^{+20}_{-4}	1
5:4	34.87	$0.2^{+0.8}_{-0.2}$	1
4:3	36.40	$0.2^{+0.3}_{-0.1}$	6
3:2	39.37	$0.8^{+0.3}_{-0.2}$	42
5:3	42.24	$2.5^{+1.8}_{-1.2}$	12
7:4	43.63	5^{+6}_{-3}	5
2:1	47.70	10^{+8}_{-5}	9
7:3	52.86	3^{+6}_{-2}	2
5:2	55.35	$1.4^{+1.4}_{-0.7}$	8
3:1	62.50	11^{+15}_{-7}	4
4:1	75.71	$6.6^{+31}_{-6.4}$	1
5:1	87.89	180^{+330}_{-140}	3
Scattering	20–155	5^{+4}_{-2}	12

[a]The 'B Scale Factor' (biased scale factor) is the number of times the B&M model of the selected population with the knee size distribution must be sampled by the survey simulator to generate the number of detections found by the surveys. The simulated detections were counted to H_g <8.35, the knee in the size distribution.
[b]Total number of detections as found by Gladman et al. (2012), Kavelaars et al. (2008), and Alexandersen et al. (2016) surveys.

The survey population estimates have large uncertainties. To avoid relying on the specific orbital distributions from the survey population models, the B&M model is biased using the survey simulator (see Section 4.4.1). The biased B&M simula-

tion results are presented in Table 4.5. The scale factors for the knee H-magnitude distribution are presented; the choice of size distribution was unimportant for all resonances and only the the SPL for the scattering objects produced a significantly different result. Previous work by Shankman et al. (2016b) has conclusively rejected a SPL for real scattering objects, while the knee and divot distributions are both acceptable and result in no meaningful differences in the results. For this analysis, the knee distribution is appropriate for all populations.

The n:1 resonances should be populated by the capture of scattering objects, so if the B&M model accurately reproduces one population it should reproduce the others as well. This is apparent for the biased simulation and real detections in Table 4.5. The relative sizes of the scattering object population and some of the n:1 resonance populations are consistent with observations. For the real survey detections, the scattering / 3:1 / 4:1 populations have a ratio of 12 / 4 / 1; the biased B&M simulation gives consistent a ratio of 20 / 5 / 1 before conversion to the scale factor. The B- and L-scale factors between the detections and the model is within uncertainties for these populations. The scale factors of 5-10 mean that these populations require an initial disk mass of 3-5 $M_\oplus$, which is consistent with a partially depleted Nice-model initial mass (see Section 4.4.2). The B&M model for the scattering objects, 3:1, and 4:1 resonance are consistent with each other and the expected initial disk mass.

The 5:1 resonance should be populated by the same mechanisms as the 3:1 and 4:1 resonances, but both comparisons show that the B&M model significantly underpredicts this population. The efficiency of detection for the 5:1 resonance is extremely low; producing three 5:1 detections in the surveys, should result in $\sim 1,000$ scattering object detections. In order to be consistent with the scattering / 3:1 / 4:1 populations, the 5:1 B&M population would need to be $\sim 20 - 100\times$ larger, and the initial planetesimal disk would have needed to contain an unreasonable $\sim$100 $M_\oplus$ of material. As the B&M model, which populates resonances through scattering, results in appropriate populations in the 3:1 and 4:1 resonances, the detections in the 5:1, and thus the large population in that resonance, requires a different population source. This confirms that the extremely large population estimate for the 5:1 found by Pike et al. (2015) is unexplained by the currently explored models.

4.5.4 The Large Population of 5:1 Resonators

The previous section demonstrated that the 5:1 resonance is significantly underpopulated in the B&M simulation compared to survey results. Pike et al. (2015) predict an enhancement of a factor of $\sim 50 - 100$ compared to the local scattering objects, but this is not confirmed in typical Kuiper belt formation models (Hahn & Malhotra, 2005; Levison et al., 2008). The non-resonant populations in the B&M model within ± 5 AU of the 5:1 resonance (89 AU) include 54 scattering and 159 detached test particles. This is a linear density of 5 scattering and 16 detached objects per AU. The B&M 5:1 resonance has 16 particles, with an approximate width of 1 AU it is ~ 3 times denser than the scattering object population and comparable in density to the detached population, inconsistent with the prediction.

Pike et al. (2015) investigated the 5:1 Neptune resonance using both real and simulated detections. The three real object detections were found by CFEPS (Petit et al., 2011; Kavelaars et al., 2008) and a population model was created based on the constraints provided by the detections and the survey characterization. The parametric model of the 5:1 resonance from Pike et al. (2015) is reasonably consistent with the orbital distribution of 5:1 resonators from the B&M model.

The eccentricity and inclination distributions of the 5:1 resonators from the B&M model and the parametric model distributions from Pike et al. (2015) are shown in Figure 4.5. The upper limit of the eccentricity distribution is a good match, however the B&M simulation has test particles in the range $0.35 < e < 0.62$, extending to lower eccentricities than the model from Pike et al. (2015). If the B&M simulated population distribution is representative of the real 5:1 resonators, the Pike et al. (2015) eccentricity distribution underestimates the population size by $\sim$35%. The AD statistic shows that the eccentricity distribution of the biased B&M 5:1 resonators is consistent with detections. The preferred inclination width $\sigma_i = 22^\circ$ from Pike et al. (2015) is also consistent with the B&M model results (see Equation 4.3 for the inclination distribution). The toy model from Pike et al. (2015) with an inclination width of $\sigma_i = 7^\circ$ shifted to a center of $\mu = 35^\circ$ under-predicts the $i < 35^\circ$ portion. Overall, the distribution of the B&M test particles in the 5:1 resonance compares favorably to the preferred parameterization of the 5:1 resonators by Pike et al. (2015).

Once biased by the survey simulator, the three H-distributions do not produce equally good inclination distributions for the preferred inclination width $\sigma_i = 22^\circ$. The knee and divot provide statistically acceptable matches, with bootstrapped AD

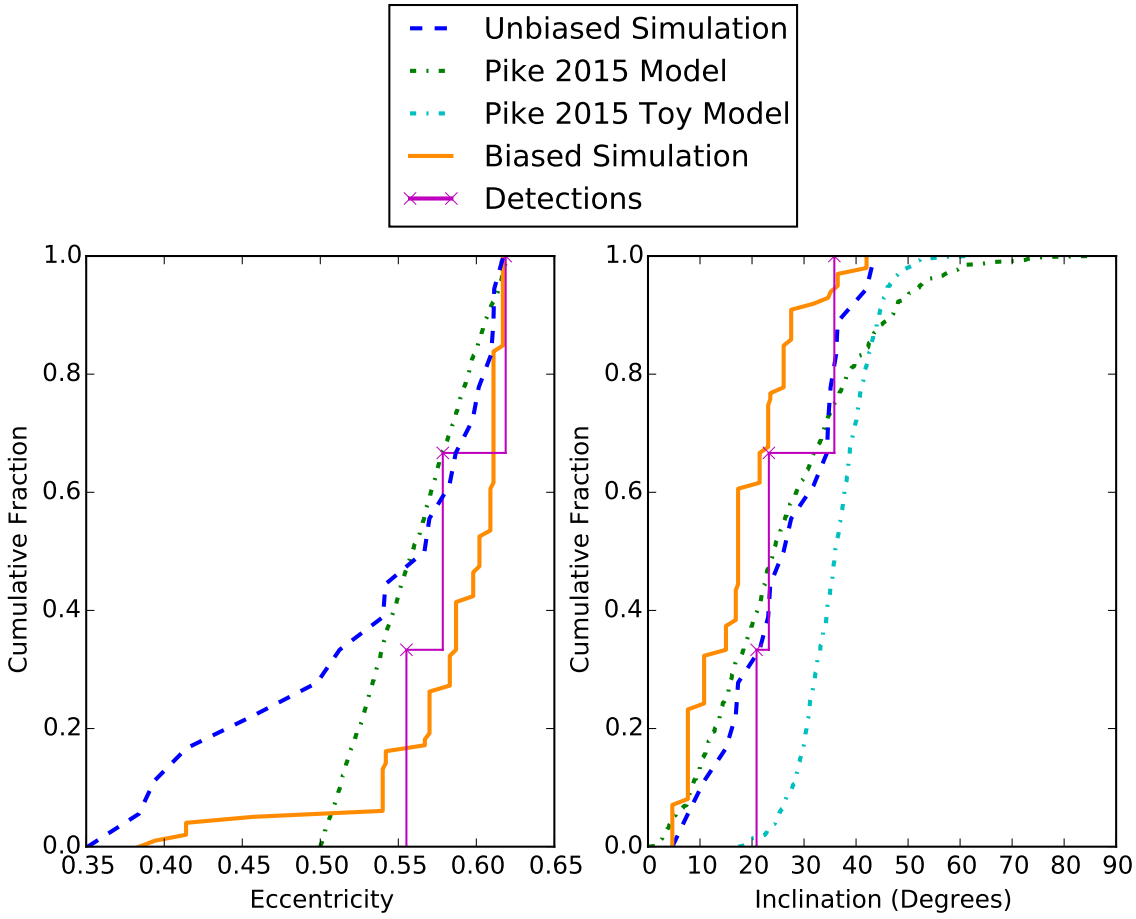

Figure 4.5 These are the 5:1 resonators in the B&M simulation (blue dashed) as well as the parametric model from Pike et al. (2015, green dash-dot) and the toy inclination model from Pike et al. (2015, turquoise dash-dot). The toy model was proposed to explore the possibility of an exclusively large-i population, $\sigma_i = 7°$ and $\mu = 35°$. The magenta 'x' detections are the real 5:1 objects discovered in Petit et al. (2011) and Kavelaars et al. (2008). The model eccentricity distribution has an appropriate upper limit, but the B&M results suggest the eccentricity is not truncated at 0.5. Also plotted are the results of biasing the B&M simulation using the survey simulator and the knee H-magnitude distribution. The biased population does not include the low-e component, reflecting the difficulty of observing the low-e particles. The preferred inclination distribution with $\sigma_i = 22°$ is an acceptable match for the B&M test particles.

statistics of 18% and 16%, but the SPL is almost rejectable at 6%; below 5% would be rejectable at the 2σ level. The SPL has more low inclination detections; this results from the not entirely uniform survey depth and highlights the interdependence of

orbital parameters and the importance of careful survey characterization.

The three 5:1 detections in CFEPS imply a large population that is inconsistent with the B&M model; some additional population mechanism must emplace objects into the 5:1 resonance. Minor model differences, such as the assumptions by Pike et al. (2015) of a smaller asymmetric libration fraction and eccentricity distribution only result in a larger population estimate, and therefore this discrepancy could not reconcile the estimates. The large population in the 5:1 resonance remains unexplained, with no improvements from the B&M simulation results.

4.5.5 Other Resonant Populations: Detailed Properties

The Twotinos (2:1 Resonators)

The B&M model contains 108 stable 2:1 resonators, or twotinos; their characteristics are shown in Figure 4.6. They occupy roughly the range of semi-major axes and eccentricities expected for this population compared to the CFEPS model and detections (Gladman et al., 2012; Petit et al., 2011; Alexandersen et al., 2016). When the biased B&M model is compared to the detections, the inclination distribution gives an AD statistic result of $2\%^{+2}_{-1}$, which is statically rejectable (the uncertainty in the AD statistic is from the different H-distributions). The eccentricity distribution of the B&M twotinos is consistent with detections. Three unstable resonators (3%) found are at lower eccentricity than the bulk population, supporting the idea that low-e resonant objects drop out and enter the detached and outer classical populations (see Section 4.5.6 for details).

The 2:1 resonators illustrate the necessity of careful survey characterization for all resonant populations. When the B&M model is biased using the survey simulator, the effects of observational bias are significant. In Figure 4.6, the SPL and knee H-distribution are shown (the divot distribution produced nearly identical results to the knee). H-magnitude distributions cannot be treated as an independent parameter from inclination, eccentricity, and libration amplitude. The choice of H-distribution significantly affects detectablity. The libration amplitudes of the particles demonstrate the effect of survey blocks of slightly different depths at different latitudes relative to Neptune, and the detected leading to trailing fraction of TNOs is also strongly affected by survey pointings. The sensitivity of the survey at different inclinations affects the measured i-distrubutions. The 2:1 resonance results demonstrate the importance of carefully characterized discovery surveys for modeling intrinsic res-

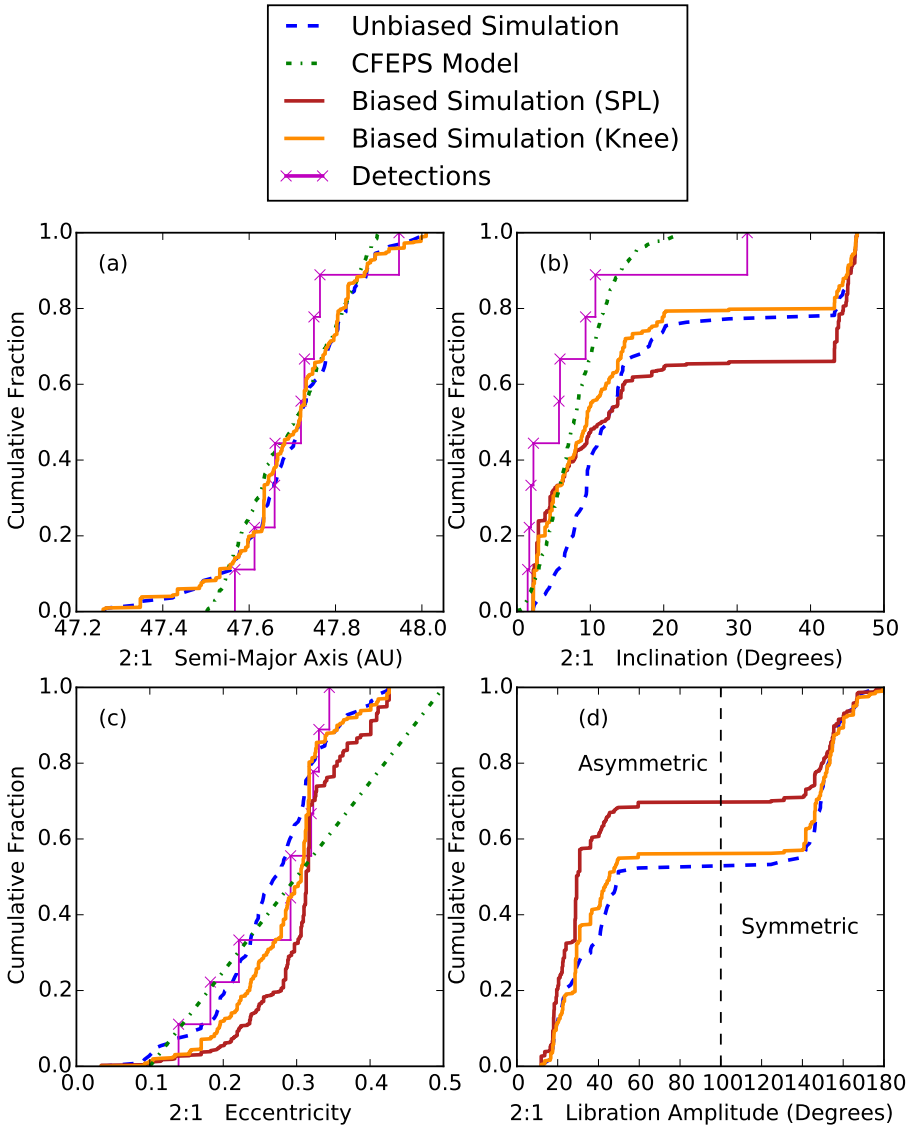

Figure 4.6 The blue dashed lines are the unbiased B&M 2:1 simulation test particles. The green dash-dot lines are the unbiased Gladman et al. (2012) model. The red and orange lines are the simulation particles biased using the survey simulator randomly assigned H-magnitudes from the SPL and knee H-distribution; these biased models can be compared with the magenta 'x' detections. The interdependence of the H, e, and libration amplitude distributions are evident (see text for details). Unstable resonators are not included in the libration amplitude plots.

onant populations.

Large-a Resonances

The resonances beyond the 2:1 display a different morphology than the resonances interior to and within the main classical belt. In Figure 4.1, the different structure is visually obvious. The resonances exterior to the 2:1 resonance do not contain very low e members, and the minimum e roughly increases with semi-major axis. The maximum e also increases with semi-major axis; this is an expected result because at larger a, a larger e is necessary for the particle to scatter off Neptune. The inclination distribution of objects in the distant resonances is visibly broader and hotter than the 3:2 and 2:1.

The eccentricity distribution of these resonances show 'fingers' of descending eccentricity from the main population of outer classicals (see Figure 4.1). These populations are likely created as a result of the Kozai mechanism, which also contributes to the hotter inclination distributions. This effect is stronger for the n:1 resonances, but is also apparent for the n:2 resonances. (See Section 4.5.6 for a discussion of the extensive effects of Kozai.) Simply due to large distances, TNOs in these distant resonances are sparsely sampled by current observations, and a theoretical model of their parametric distribution would provide useful constraints for population models derived from surveys.

The B&M model resonances beyond the 2:1 are not affected by the starting conditions of the simulation, so they provide realistic models of these distant resonances. Figures 4.7 and 4.8 show the cumulative distribution of the unbiased B&M particles in the n:1 and n:2 resonances by inclination and eccentricity. The range of eccentricities and inclinations displayed by the distant n:1 and n:2 resonances are particularly interesting, because they affect population estimates and are weakly constrained by surveys. Survey population estimates suggest the distant resonances should have relatively large populations, albeit with large uncertainties (Gladman et al., 2012; Pike et al., 2015; Alexandersen et al., 2016).

Several conclusions are evident from the distributions of inclination and eccentricities for the n:1 and n:2 populations in the B&M model. The B&M model suggests a hot inclination distribution is likely for all n:1 resonances beyond the 3:1, but increased inclinations are not obvious for the n:2 resonators until the 13:2, at a much larger semi-major axis. The average eccentricities of n:1 and n:2 resonant populations increases with semi-major axis; the more distant n:1 resonances all have less than 5% of particles with $e < 0.35$ (see Figure 4.7) and the distant n:2 resonances have less

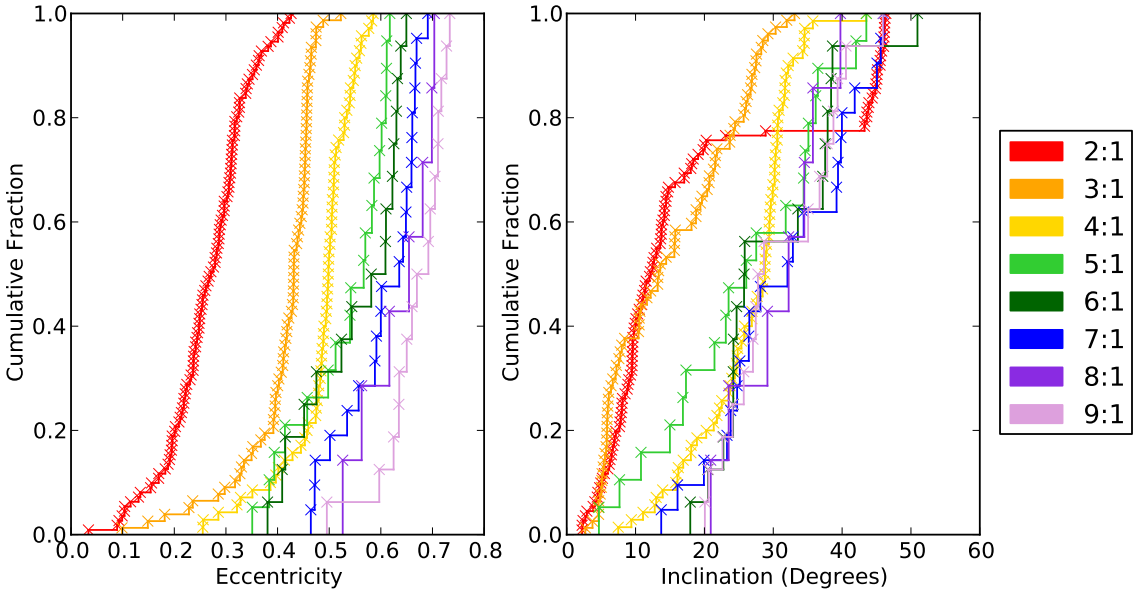

Figure 4.7 The cumulative fractions of the n:1 test particles are given for e (left) and i (right). The 2:1 and 3:1 have a significantly different morphology, especially in the i-distribution, than the more distant resonances. Beginning with the 4:1, there is a slight trend for hotter i values with increasing a. This different morphology between the resonances likely results from the additional Neptune encounters needed to emplace an object at large-a.

than 5% of particles with $e < 0.5$ (see Figure 4.8). The bulk of the population in these resonances has nearly the maximum stable eccentricity. Population estimates which exclude a low-e component are not significantly underestimating the population, however a uniform e-distribution may overestimate the population by including too many particles at low-e.

Resonance Libration

The libration amplitude, or range of resonant angles a particle explores (the amplitude of Equation 4.1), is influenced by the specific capture mechanisms and migration timescales (e.g. Chiang & Jordan, 2002). The libration amplitudes of the stable B&M n:1 and n:2 resonators are shown in Figure 4.9. The n:2 resonators occupy a single resonant island and have libration amplitudes from 6° (for the lowest libration amplitude 5:2 resonator) to just less than 180° (for the largest amplitude 5:2 resonator). The n:1 test particles include both large-amplitude symmetric and small-amplitude

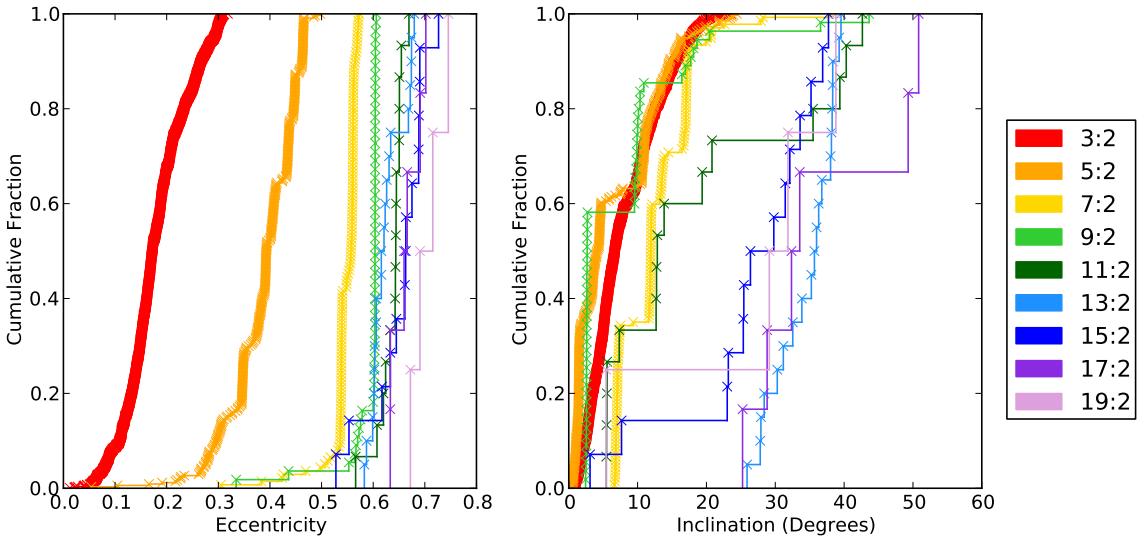

Figure 4.8 As in Figure 4.7, the cumulative fractions of n:2 test particles in the resonances are given for e (left) and i (right). The resonances beyond the 5:2 have $< 5\%$ of members with $e < 0.5$. The 5:2 and 9:2 contain a significant fraction of low-i members.

asymmetric librators.

The B&M n:2 resonators have a large range of libration amplitudes in a single libration island. The 3:2 and 5:2 resonance have roughly uniform distributions from 20° to 140° and 160°. The 7:2 and 9:2 resonances have a lower median libration amplitude, and the 11:2 and 13:2 resonators have a higher mean libration amplitude than the 3:2 and 5:2 resonators. In all of these resonances, libration amplitudes below 20° are either nonexistent or an insignificant fraction of the population. This reflects a combination of reduced phase space at low amplitude and the inefficiency of deep capture because the population is implanted through scattering capture. Volk et al. (2016) searched for low libration amplitude Plutinos in the OSSOS survey which may require resonance sweeping capture; their minimum libration amplitude detected TNO has an amplitude of $10^{\circ}{}^{+8}_{-4}$. This low libration amplitude Plutino discovery suggests that the Plutinos include a sweep-up capture component; the presence or absence of low-libration amplitude 5:2 resonators in the real Kuiper belt could provide useful insight into the extent of the planetesimal disk.

The dynamical behavior of the n:1 resonators is more complex than the n:2 test particles because the n:1 resonators can occupy three libration islands: the symmetric island at 180° as well as the leading and trailing asymmetric libration islands. Because

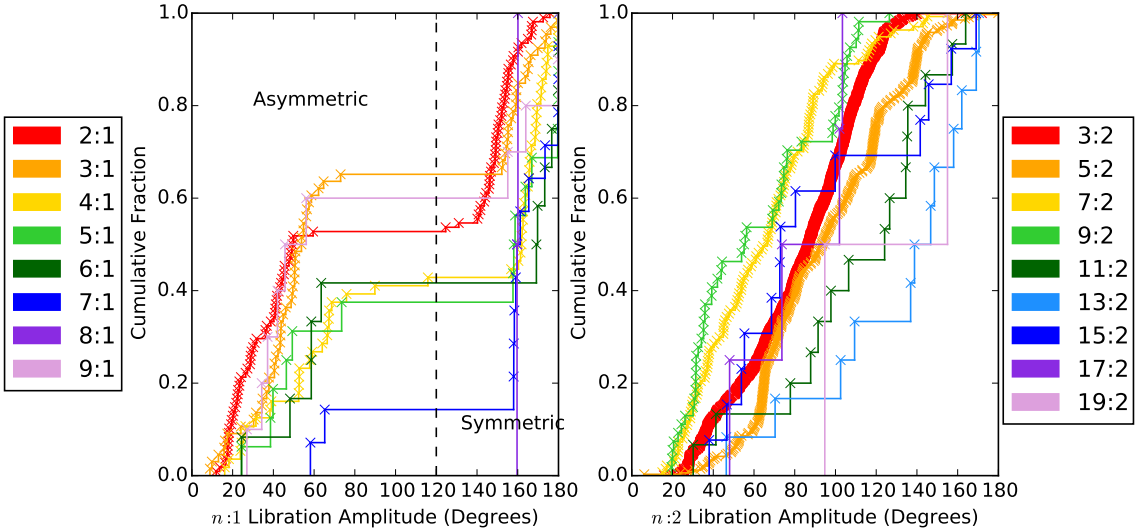

Figure 4.9 The cumulative fractions of libration amplitudes for the stable test particles in the n:1 (left) and n:2 (right) resonances. The n:1 resonators include high amplitude symmetric librators and a high fraction of low amplitude asymmetric librators. The n:2 includes only symmetric resonators, which possess a large range of libration amplitudes, from 6° to 179°. The slightly discontinuous nature of the distributions is likely an effect of slightly under-sampling the resonant phase space.

of the segregated phase space, symmetric librators all have large libration amplitudes ($\gtrsim$ 120°) and asymmetric librators have small amplitudes. As a result, the relative fractions of symmetric and asymmetric resonators are apparent in Figure 4.9, as a large gap separates the libration amplitude of the symmetric and asymmetric islands.

The 2:1 resonators in the B&M simulation include a significant number of asymmetric librators. Gladman et al. (2012) population models for the n:1 resonances use an asymmetric fraction of 30%; the B&M asymmetric fraction for the 2:1 resonance is a factor of two higher, ∼60%. The Gladman et al. (2012) model uses an evenly divided asymmetric population, which is inconsistent with both the B&M model and the different simulation results from Chiang & Jordan (2002).

The relative fraction of leading and trailing asymmetric librators for the 2:1 resonance may be diagnostic of Neptune's mode of migration. Chiang & Jordan (2002) tested a range of simulation migration speeds, from 50,000 years to 5 Myr, and found that the faster migration speeds increased the fraction of 2:1 resonators in the trailing libration island. Measuring this fraction is a goal of characterized surveys; the complete OSSOS survey will provide strong constraints on this ratio (e.g. Volk et al.,

2016). Based on CFEPS and the first results from the OSSOS survey, Volk et al. (2016) constrains the fraction of 2:1 leading asymmetric resonators at $< 90\%$, and more survey blocks focused on the leading libration island are required to reduce the significant uncertainty of this measurement; these will be part of the full OSSOS survey. Determining relative population sizes of the different resonant components in the Kuiper belt based on survey results will provide constraints on different Solar System migration models.

The distribution of symmetric and asymmetric librators for several of the n:1 resonances is presented in Table 4.6. The B&M 2:1 population includes 47 test particles in the leading asymmetric island, 21 test particles in the trailing asymmetric island, and 40 particles in the symmetric island. This gives a fractional occupancy of 37% symmetric librators, 43% leading and 19% trailing asymmetric librators. This is surprising given the simulation results from Chiang & Jordan (2002) that the trailing 2:1 libration island was more populated than the leading island, an effect that became more amplified with faster Neptune migration (up to $\sim 300\%$). The majority of the B&M giant planet orbital evolution takes place within $\sim 10^6$ years, a very similar timescale to the faster simulations in Chiang & Jordan (2002). However, the B&M model has a factor of two enhancement in the leading island over the trailing island. The enhancement in particular libration islands must depend on additional migration parameters than purely migration speed, such as the starting orbital parameters of all of the giant planets and the initial orbits of the particles. This is unfortunate as many authors have hoped that measuring the ratios of populations in the various libration islands could provide a diagnostic of migration speed; this result shows the interpretation will be more complicated.

Table 4.6 Libration Islands of Stable n:1 Resonators

p:q	Particles	Leading	Symmetric	Trailing
2:1	108	43%	37%	19%
3:1	66	53%	27%	19%
4:1	56	37%	41%	21%
5:1	16	37%	31%	31%
6:1	12	50%	33%	16%
7:1	14	50%	50%	0%

The asymmetric islands of the B&M n:1 resonances are all heavily populated,

and the preference for the leading island continues through all n:1 resonances that have enough test particles for a reliable ratio to be determined. The fraction of test particles in each libration island is given in Table 4.6. The 2:1 and 3:1 resonances are particularly enhanced, with two to three times as many particles in the leading than trailing island. In the B&M model, an asymmetric fraction of 50%-70% is found for the 2:1, 3:1, 4:1, 5:1, 6:1, and 7:1 resonances. These more distant resonances must be populated through scattering capture. The large fraction of asymmetric librators may reflect the greater stability of the lower libration amplitude subcomponent of the resonances; the majority of unstable resonators in the B&M simulations are symmetric. The B&M simulation results confirm that short migration timescales can often produce asymmetries in libration island capture in a similar manner to Chiang & Jordan (2002), however more theoretical work is needed to understand the additional constraints which influence the specifics of where the asymmetries appear.

4.5.6 The Importance of the Kozai Mechanism

The Kozai mechanism results in an exchange between eccentricity and inclination, conserving the z-component of angular momentum (Lidov, 1962; Kozai, 1962). Outside of mean-motion resonances, this can only operate for very high inclinations (Thomas & Morbidelli, 1996). But inside mean-motion resonances, even moderate inclination objects can experience this effect (e.g. Pluto at $i \simeq 17°$; Williams & Benson, 1971). The angular momentum exchange results in anti-correlated oscillations of eccentricity and inclination, and oscillation of the argument of pericenter, ω, all having the same period ($\sim$Myr timescales).

Kozai resonators are identified within several mean motion resonances in the B&M simulation. Figure 4.10 shows the eccentricity-inclination distribution for three mean-motion resonances with Kozai oscillators: the 3:2, 5:2, and 2:1 resonances. Kozai oscillators in each of the resonances occupy a significant fraction of the highest e and i space. Because the z-component of the angular momentum is conserved during an oscillation, a given object will appear to move along an arc in e–i space; this is especially visible for the 5:2 resonance. The tight arcs in the 5:2 resonance are likely a result of cloning oversampling a particular Kozai energy state; the 3:2 resonance is better sampled and displays an expected continuum of Kozai resonators.

Particularly for the Kozai plutinos, larger i correlates with a constrained range of e values (see Figure 4.10). This dependence is not usually included in population

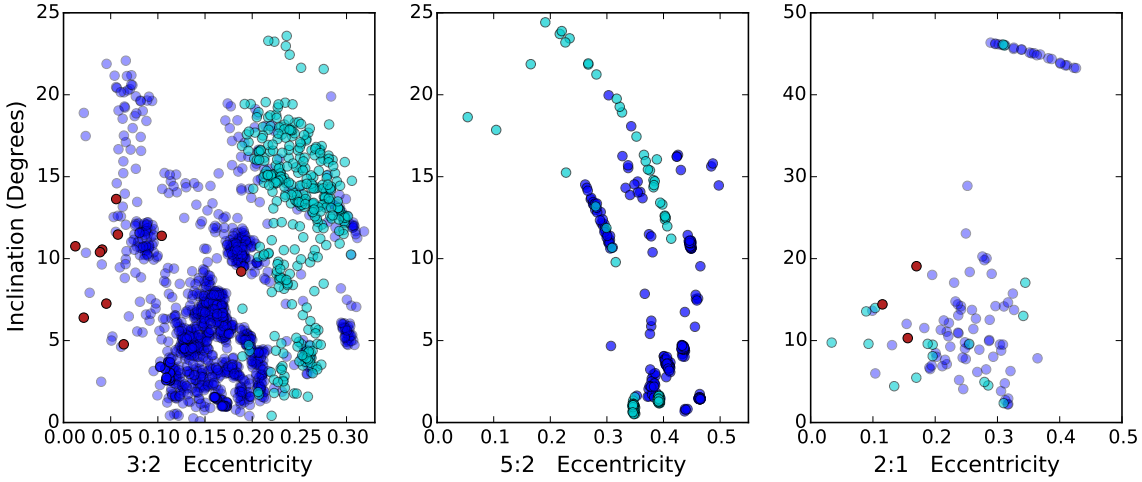

Figure 4.10 The B&M simulation particles in the 3:2, 5:2, and 2:1 resonances are shown in e–i space. The 3:2 and 5:2 have strong e–i dependence. The structure in the 5:2 resonance is exaggerated (as a result of cloning); the 3:2 Kozai particles show the expected continuum distribution. The red circles are not stable in the resonance, the blue circles are stable, and the cyan circles are stable Kozai resonators. At the end of the B&M simulation 20–30% of objects in the 3:2, 5:2 and 2:1 resonances also exhibit Kozai oscillations.

models, which is a major weakness of typical resonant population modeling. 21% of the 1640 B&M Plutinos are in Kozai which agrees well with the highest likelihood Kozai fraction of 20% for the OSSOS survey found by Volk et al. (2016). Though the Kozai fraction matches observations, the inclination distribution within the B&M Plutinos doesn't include sufficiently excited particles. A migration rate for which Kozai is more effective may be key to a sufficiently hot inclination distribution for the Plutinos.

The inclination distribution of the B&M model 5:2 resonators appears to have multiple discrete components as a result of Kozai resonance and particle cloning during the simulation. The $e < 0.3$ particles all have large i; two components for both the eccentricity and inclination are apparent. 29% of the 337 5:2 resonators are in Kozai. The inclination distribution of the non-Kozai fraction of the 5:2 is less dynamically hot than the 5:2 population as a whole; this distinction has important implications for population models.

Even though Kozai is not operating for all of the resonant particles at the end-state of the simulation, its effect is clearly seen in the distribution. The interdependence

of inclination and eccentricity as well as the presence of high inclination particles is indicative of Kozai evolution. Kozai resonance dropout may be just as important for shaping the orbital element distribution within resonances as resonant dropout is for shaping the distribution of detached objects, as discussed in the following section.

Signatures of Kozai Beyond the Main Classical Region

The effects of temporary evolution in Kozai resonance are apparent in the regions beyond the main classical belt. This region is populated by outer classical objects (an extension of the main classical belt), objects in resonance with Neptune, detached objects, and scattering objects, which have semi-major axes that are changing on short timescales as a result of Neptune's influence. The outer classical objects are defined to have $e < 0.24$, so this population is sharply truncated. In Figure 4.1, the outer classical objects and some detached objects can be seen located near the resonance fingers. These particles all have $q > 40$ AU and were likely emplaced by the same mechanism that created the detached objects in the same q range; these particles cannot be primordial because no test particles started at these large semi-major axes. A pericenter cut of $q > 40$ AU AU is a more useful division of distant objects. This $q = 40$ AU boundary is a black arc starting from $a = 40$ AU in Figure 4.1. The particles with $q > 40$ AU, referred to as 'high-q' objects, include test particles from the detached and outer classical populations ($a > 62.5$). These subpopulations have different dynamical characteristics as a result of their emplacement histories. Figure 4.11 shows the inclination and eccentricity distributions of particles in the various sub-populations in the outer Kuiper belt.

The high-q subpopulation has different characteristics than the detached and scattering populations. These high-q particles have a much colder eccentricity distribution, reaching down to $e = 0.16$. This population also has a hotter inclination distribution, with a median of 28°. Based on the e and i distributions, it appears that these particles were emplaced through resonance dropout or diffusion, after the Kozai mechanism reduced their eccentricities and increased their inclinations. When objects evolve to low-e, where the resonance is narrower, particles are more likely to exit the resonance. Some of the detached objects are not particularly close to a resonance, and these particles (as well as others near resonance) may have been emplaced through dropout as Neptune (and the resonances) migrated outward (Gomes, 2003). A circularization of Neptune's orbit can also shrink the width of the resonance, particularly

at low eccentricity, and cause resonance dropout (Gomes et al., 2008). These high-q particles are consistent with formation through resonant dropout after modification by Kozai within distant mean-motion resonances.

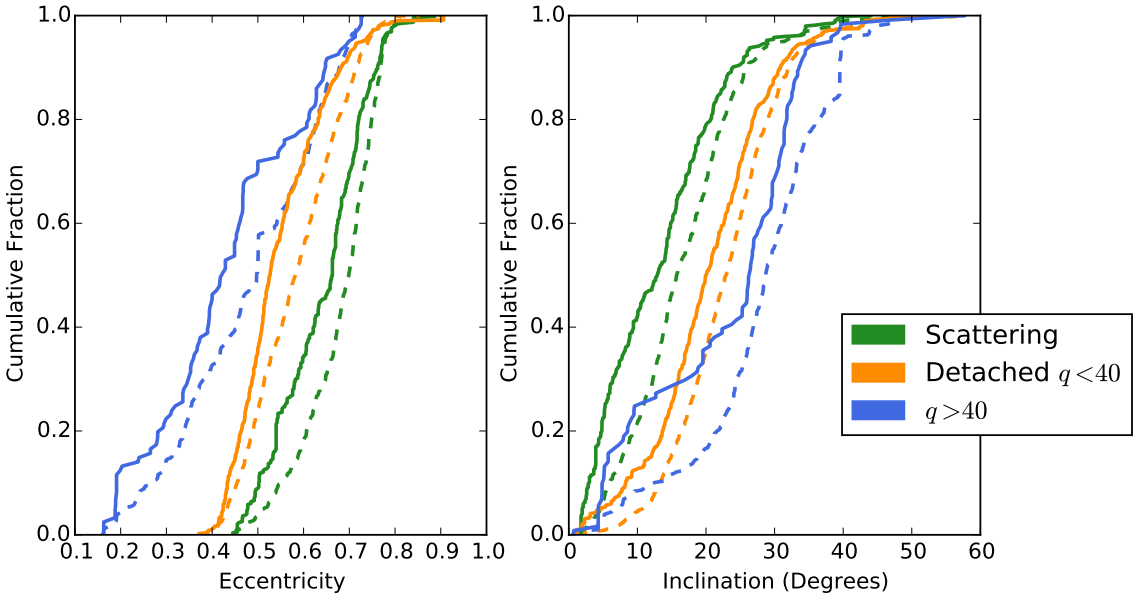

Figure 4.11 These are the cumulative fractions of non-resonant B&M objects beyond the 3:1 resonance (62.5 AU) in eccentricity and inclination. The scattering objects (green) have hotter eccentricities and colder inclinations, while the detached objects with $q < 40$ AU (orange) have intermediate inclinations and colder eccentricities. The high-q particles (blue) have lower eccentricities and higher inclinations. The dashed lines show the simulation test particles, and the solid lines show the test particles biased using the survey simulator. Except for the inclination distribution of high-q objects, the choice of size distribution has a minimal effect on the detectability of these populations.

The detached population includes the majority of these high-q objects in addition to a large $q < 40$ AU population. The eccentricity distribution of the detached objects is somewhat hotter and the inclination distribution is somewhat colder than the $q > 40$ AU sub-population, indicating the larger sample includes particles less modified as a result of Kozai. In Figure 4.11, only the $q < 40$ AU sub-component of the detached objects is presented. These particles still may be emplaced through resonant dropout, however the Kozai mechanism likely did not play a significant role in the $q < 40$ AU portion of the detached population.

The scattering objects, in contrast, have hotter eccentricity distributions and

colder inclination distributions. These particles were also likely modified by the Kozai mechanism, increasing the eccentricity and decreasing the inclination during a resonance capture. The mean-motion resonances are weaker at the extreme values of e and i, so escape is more likely for these particles. After the particle diffuses or drops out of resonance it is scattered by Neptune on relatively short timescales.

The distant B&M particles have a range of eccentricity and inclination distributions indicative of their emplacement history. The Kozai mechanism within mean motion resonances has resulted in populations anti-correlated in i and e. This distribution of objects in the B&M simulation in e and i is consistent with the Kuiper belt, and the effect of the Kozai mechanism has been noted in previous simulations, which found a noticeable fraction of distant resonant objects evolving to low-e (Gomes, 2003; Pike et al., 2015).

4.5.7 Scattering Objects

The distribution of the B&M scattering objects is similar to the model used by Shankman et al. (2013, 2016b). The Shankman et al. (2013, 2016b) scattering object model used orbital parameters based on the simulation results from Kaib et al. (2011). The detectability of scattering objects with the divot, knee, and SPL size distributions on the B&M simulation scattering objects is shown in Figure 4.12 (see Equation 4.2 for details).

The models are compared in the semi-major axis region of the classified B&M model, 24-155 AU. The biased simulation with the SPL, knee, and divot H-distribution all provide a statistically acceptable semi-major axis distribution match for the real detections. The SPL results in a significantly worse eccentricity distribution, nearly rejectable by the AD statistic of 7%. The knee and divot e-distributions are non-rejectable at 61% and 54%. The difference in inclination distribution models is not significant; the more important issue is the lack of retrograde objects in the B&M simulation results; these come from the Oort cloud (Brasser et al., 2012). When the detected retrograde TNO (from Kavelaars et al. (2008) at $i > 90^\circ$ in Figure 4.12) is excluded, the three H-distributions all haveAD statistics of 60%-85%. Based on the B&M model of the a, e, and i distribution of the scattering objects, a knee (Fraser et al., 2014) or divot (Shankman et al., 2013) size distribution provides a significantly better representation of the real detections than a SPL distribution; this confirms the results from Shankman et al. (2013, 2016b). The orbital parameters of the scattering

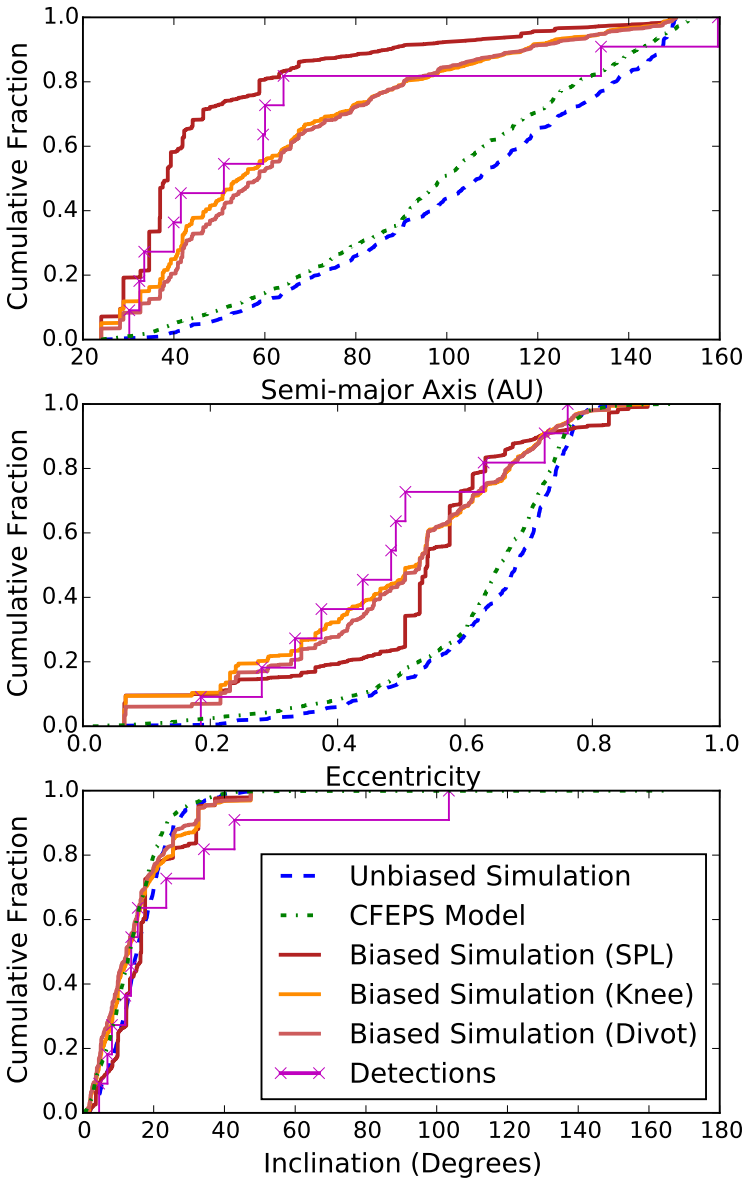

Figure 4.12 The cumulative fraction of scattering objects in the B&M simulation with the a, e, and i values are indicated in blue. The green (dash-dot) line indicates the model used to represent the unbiased CFEPS distribution (Shankman et al., 2013, 2016b), which is similar to the blue (dashed) B&M simulation end state. The B&M particles were biased using the survey simulator and three different H-magnitude distributions. The magenta 'x' marks indicate actual detections from the surveys simulated, for comparison with the B&M biased simulation results. The observed orbital element distributions are better matched by the knee or divot size distributions than the SPL.

objects are consistent with the parameters from Kaib et al. (2011), confirming that properties of the scattering population are not particularly dependent on the specifics of the scattering event. The scattering objects in the B&M simulation provide a good model of this population for comparison, but requires a knee or divot size distribution.

4.6 Discussion and Conclusions

In this chapter, the results of the B&M simulation were compared with well-characterized surveys: CFEPS (Petit et al., 2011; Kavelaars et al., 2008), OSSOS (Bannister et al., 2016), and Alexandersen et al. (2016). This tests the effectiveness of a cosmogonic model involving Neptune scattering (similar to the Nice model) in creating a detailed Kuiper Belt that matches the reality observed today. For some resonant populations, this Nice model scenario provides a reasonable match, particularly resonances populated through scattering capture, but for others the model does not produce an acceptable population distribution.

The B&M simulation produces test particles with an orbital distribution similar to the main classical TNOs. The inclination distribution of the test particles displays two components, similar to the inclination distribution model of Petit et al. (2011), which is based on real TNO detections and has a colder component of $\sigma_i = 2.6°$ and a hotter component with $\sigma_i = 16°$. The B&M main classical particles with low inclinations have a slightly hotter eccentricity distribution than real TNOs, however this distribution does extend to low-e. The discrepancy in eccentricity distribution probably results from a starting population with large e; this could possibly be mitigated by using a lower-e starting disk. The B&M modeled dynamical evolution naturally produces a two component inclination distribution, different in specifics but broadly similar to the hot classical objects and the cold classical belt.

The size of the B&M population in the 5:1 resonance is severely underpopulated compared to the other resonant populations and the scattering objects in the B&M model. Pike et al. (2015) calculated that the 5:1 population is likely as populous as the 3:2 resonance based on object detections in Petit et al. (2011) and Kavelaars et al. (2008). The B&M simulation produces acceptable population ratios between the 3:1, 4:1, and scattering populations. The 5:1 resonance is populated in the same manner as the 3:1 and 4:1 resonances, however the B&M simulation produces far too few 5:1 resonators compared to the number of detected TNOS from CFEPS and the model by Pike et al. (2015). The B&M simulation results were compared with

the de-biased CFEPS models of the 5:1 and scattering population, and the B&M simulation results were biased using the CFEPS survey simulator and compared to the detections. In both comparisons, the small size of the 5:1 resonance in the B&M simulation is incompatible with the three 5:1 detections. The population in the 5:1 resonance must have an additional source and population mechanism in order to have a large enough population to be consistent with detected 5:1 objects. The inclusion of an additional planet in the Kuiper belt region would only result in smaller populations in the 5:1 resonance (Lykawka & Mukai, 2008). The large observed population of 5:1 resonators in the Kuiper belt remains unexplained.

The B&M simulation used rapid planetary migration and results in asymmetric capture into the n:1 resonance islands. B&M use migration rates similar to those modeled in Chiang & Jordan (2002), who found unequal capture into the 2:1 asymmetric islands. Chiang & Jordan (2002) and Murray-Clay & Chiang (2005) determined that the **trailing** libration island was more populated for the 2:1 resonators, captured through resonance sweeping. The B&M model produces an asymmetry in the 2:1 resonance, as well as the 3:1, 4:1, 5:1, 6:1, and 7:1 resonators, where the **leading** libration island is more populated. The particles trapped in the n:1 resonances in the B&M simulations are captured through scattering; this shows that scattering capture also produces asymmetries. The B&M model shows the opposite asymmetry than predicted by previous work, so asymmetries in libration island capture are indicative of specifics of migration, but capture asymmetry is sensitive to more than just the migration rate. In addition to the capture mechanism, the initial planet semi-major axes and eccentricities may also play a role, and more work is needed to determine the best interpretation of asymmetries in the n:1 populations if they are discovered in future observations of the real Kuiper belt.

The effect of the Kozai mechanism in the simulations is apparent in multiple populations. Approximately 20% of the 3:2, 2:1, and 5:2 resonators are in Kozai, which matches the Kozai fraction measured for the Plutinos (Volk et al., 2016). Lykawka & Mukai (2007a) found a Kozai fraction 20-30% for the 2:1's, consistent with the B&M fraction, but observation biases for Kozai resonators are complicated, and a complete model is required to properly debias these observed Kozai fractions (Lawler & Gladman, 2013). The signature of the Kozai effect is also identifiable in non-resonant populations; these particles were likely resonant and in Kozai at an earlier time in the B&M orbital evolutions. Particles can enter Kozai more easily while in mean motion resonance since Kozai oscillations occur at much lower inclinations in-

side resonances. This alternately pumps the particle's eccentricity or inclination. At large-e and large-i, resonances are less strong, and particles can diffuse or drop out of resonance.

The non-resonant simulation objects beyond the 3:1 resonance have distinct e and i distributions. The high-q ($q > 40$ AU) objects have lower e (resulting in the large q), but this low e is strongly correlated with a hotter inclination distribution. These large inclinations and low eccentricities were likely produced through temporary capture into a mean-motion resonance and Kozai, which decreased the eccentricity and increased the inclination. The test particles then diffused or dropped out of the resonance and became detached or outer classical objects. The detached objects include a large fraction of these high-q objects, and this population had almost as cold an e and hot an i distribution, but is diluted by objects which are not significantly evolved by Kozai resonance capture. The scattering objects are those that had the opposite occur: they are likely created by leaking out of resonance after the e is increased and the i is decreased due to Kozai inside mean-motion resonances.

The Gladman et al. (2008) dynamical classification system beyond the main classical belt was not optimal for understanding the B&M simulation results. This classification separated test particles which share a common origin into different subcomponents, and it also placed into the same classification some particles with very different evolutionary histories. The 'outer classical' objects in the B&M simulation are clearly just the low-e extension of the $q > 40$ AU population, which is much more dynamically distinct. With the initial conditions of the B&M model, objects in the outer classical region cannot be primordial. There is a shared dynamical origin for the outer classical and some detached objects, so a pericenter cut for dynamical classification is more informative than the Gladman et al. (2008) classification in the distant Solar System.

The resonant objects are a good test of the B&M simulation; they account for 42% of the test particles and are sensitive to the specifics of migration. Several of the resonant test particle populations do not have a hot enough inclination distribution, a common issue in dynamical evolution models (Gladman et al., 2012), however the more distant resonance inclination distributions are well represented by the B&M simulation. The simulated eccentricity distributions are consistent with the data, and may provide a useful model basis for the more distant resonances which have significantly fewer detections. These high-a resonances in the B&M simulation often lack a low-e component, typically omitted from population models for detectability

concerns (Gladman et al., 2012; Pike et al., 2015; Volk et al., 2016), which suggests that the practice of omitting these nearly undetectable low-e objects from population models does not invalidate these population estimates.

The B&M simulation results in an acceptable model of the populations in the Kuiper belt created primarily through capture of objects scattered by Neptune, but also reveals some of the areas where improvement is necessary. Resonant populations which include the capture of particles through resonance sweeping do not match the parametric distributions of real TNOs from characterized surveys. However, the outer resonant populations and the scattering, detached, and outer classical populations are an informative comparison sample for real TNOs. Overall, the B&M simulation provides a good model of the population sizes and orbital distributions of the distant components of the Kuiper Belt, and provides us with the ability to make the most detailed comparisons between the model and reality to date.

Chapter 5

On a Possible Size/Color Relationship in the Kuiper Belt

This chapter contains my research from Pike & Kavelaars (2013). I created the model color distributions from the literature and used the survey simulator to determine detectability. Dr. JJ Kavelaars provided a basic script to calculate the Anderson-Darling statistic, which I refined to include my additional bootstrapping calculations.

The focus of this chapter is to quantify the misleading nature of detections reported in the available literature. Using all TNOs with measured surface properties provides a large sample, but the unknown discovery and photometric followup biases imposed on the data can result in an observed color distribution which does not resemble the underlying color distributions. Quantifying the intrinsic color distributions of TNOs requires a sample with well understood discovery and measurement biases, and cannot be accomplished with any sample currently available in the literature.

5.1 Abstract

Color measurements and albedo distributions introduce non-intuitive observational biases in size-color relationships among Kuiper Belt Objects (KBOs) that cannot be disentangled without a well characterized sample population with systematic photometry. Peixinho et al. (2012) report that the form of the KBO color distribution varies with absolute magnitude, H. However, Tegler et al. (2003) find that KBO color distributions are a property of object classification. We construct synthetic models of observed KBO colors based on two $B-R$ color distribution scenarios: color distri-

bution dependent on H magnitude (H-Model) and color distribution based on object classification (Class-Model). These synthetic $B-R$ color distributions were modified to account for observational flux biases. We compare our synthetic $B-R$ distributions to the observed 'Hot' and 'Cold' detected objects from the Canada-France Ecliptic Plane Survey (CFEPS) and the Meudon Multicolor Survey (2MS). For both surveys, the Hot population color distribution rejects the H-Model, but is well described by the Class-Model. The Cold objects rejected the H-Model, but the Class-Model (while not statistically rejected) also does not provide a compelling match for data. Although we formally reject models where the structure of the color distribution is a strong function of H magnitude, we also do not find that a simple dependence of color distribution on orbit classification is sufficient to describe the color distribution of classical KBOs (cKBOs).

5.2 Introduction

The first color measurements of KBOs found that they exhibited a surprising diversity of colors. If KBOs were formed in situ, they would have nearly identical compositional properties and weathering histories because the region between 34 AU and ∼60 AU is characterized by a single set of stable volatile materials (Brown et al., 2012). Color measurements of KBOs, however, show a range from very red ($B-R \sim 2.0$) to neutral or blueish ($B-R \sim 1.0$), compared to a solar $B-R$ of 1.03. There is little consensus on the origin of the KBO color heterogeneity.

The effects of collisional processing and weathering on KBO colors have been considered. Luu & Jewitt (1996) performed numerical simulations which incorporated a reddening component from irradiation and a collisional erosion process which exposed neutral material on the objects' surfaces. This model successfully reproduces the range of colors observed in KBOs, but also predicts objects with large photometric light curves due to surface color variations and partial resurfacing from impacts. This was later found to be inconsistent with the small magnitude variations for KBOs, regardless of $B-R$ color (Jewitt & Luu, 2001). The model also does not predict the correlated colors of binary KBOs (Benecchi et al., 2009). A balance of collisional resurfacing and weathering processes was found to be incompatible with the observed properties of KBOs.

Space weathering may still have a measurable impact on the apparent colors of KBOs. Kaňuchová et al. (2012) used a two component model of KBO composition

and investigated the effects of weathering due to solar wind ions. Their lab experiments showed that irradiation caused reddening in the carbon-bearing material, but further exposure resulted in a darkening and flattening of the spectra. Their model incorporated a component with a flat spectrum and a silicate material with a carbon-bearing layer. The varying combination of these components with different amounts of irradiation reproduces the range of colors seen in the outer solar system. If the colors of KBOs are a result of solar wind irradiation, the entire evolutionary history, as well as original composition, would affect the apparent color of KBOs.

Different KBO colors may primarily reflect compositional variation during formation. Brown et al. (2012) argue that when objects form outside of approximately 20 AU, methanol ice (CH_4O) is stable and will be incorporated into the objects. The irradiation of this ice will result in a red object with a high albedo (Brunetto et al., 2006). Inward of approximately 20 AU, the surfaces of objects are composed of water (H_2O), carbon dioxide (CO_2), and small amounts of hydrogen sulfide (H_2S), creating a dark, neutral surface color when irradiated (Moroz et al., 2004; Palumbo et al., 2004). Transport of this assortment of KBOs from their different source regions to their current locations in the Kuiper belt may explain the distribution of neutral and red KBOs observed.

At least two scenarios of KBO color distribution have been proposed. Tegler et al. (2003) found that the Cold cKBOs were red while the Hot cKBOs were grey. Hot and Cold objects were differentiated using perihelion, q, and inclination, i, and they found two different unimodal color distributions. Different color distributions for different dynamical classifications suggests that the Hot and Cold cKBOs have different histories, perhaps different formation locations. A recent paper by Peixinho et al. (2012) performed a detailed statistical analysis of KBO colors based on H magnitude, a proxy for size, searching for a correlation with $B-R$ color distributions. Data were compiled from previous surveys, and 253 objects were included in the analysis. The colors of small objects ($H > 6.8$) were found to be well described by a bimodal distribution. The larger objects ($H < 5.0$) were also found to follow a bimodal distribution, but with slightly different peak values. The intermediate objects were found to be unimodal, covering the full range of $B - R$ values seen in the other H ranges. If this H magnitude dependency is true, new models will be required to understand the physical processes that create this effect. Resolving the nature of the color diversity is a necessary step in understanding the global evolution of the Kuiper belt.

KBO discoveries and followup observations have had limited success because of the challenges presented by several observational biases. The discovery of KBOs in a survey results in predicted observational arcs. Depending on the prediction algorithm, assumptions are made about the objects' orbits, such as an energy constraint, a circular orbit, or the detection location (perihelion or aphelion). These different assumptions have different recovery rates for different dynamical classes of object (Jones et al., 2006). The size of the recovery field also has a significant impact on the likelihood of successfully detecting the KBO during followup observations. These challenges are reflected in the Minor Planet Center database, which often includes objects that were "lost" or have ambiguous orbital parameters. KBOs with poorly predicted orbits may even have incorrect orbital classifications. It can require years of observations to constrain an orbit accurately enough to determine if an object is in a resonance (Gladman et al., 2001). The discovery wavelength can also have an impact on the colors of discovered objects; redder objects are easier to find in an R band survey, but extremely red objects are difficult to measure in a range of photometric colors. The effect of these biases becomes more difficult to quantify when data are combined from multiple surveys.

We investigate the $B - R$ color distributions of cKBOs using two sample populations. We use a sample from CFEPS (Petit et al., 2011), with a known discovery method, and a sample from the 2MS photometric measurements (Doressoundiram et al., 2005), which has unknown selection effects. The KBOs are classified into Hot and Cold populations in two different ways: based on their q and semi-major axis, a, as well as by an i cut. The a and q cuts appear to provide a better division between the Hot and Cold cKBO populations in the CFEPS L7 model (Petit et al., 2011). We create synthetic cKBO populations with color distributions based on object classifications and H magnitudes and attempt to account for the biases introduced by photometric followup observations. The cKBO model populations are compared to the real cKBO samples using the Anderson-Darling statistical test. We find that an H magnitude based color distribution is statistically rejectable by the observations, but color distributions purely based on dynamical classification appear to be insufficient to describe the color distribution of cKBOs.

5.3 Sample populations

To distinguish between competing models for KBO color distributions, we compare published KBO color measurements with model based distributions. We consider two independent samples of KBO colors; a sample derived from the CFEPS L7 release (Petit et al., 2011), and one based on the 2MS data (Doressoundiram et al., 2005). The CFEPS L7 sample was cross referenced with the MBOSS database of photometric KBO observations (Hainaut & Delsanti, 2002) to determine the photometric properties of the sample. Selecting only the classical CFEPS L7 objects that have high-quality photometric measurements in the MBOSS database results in a sample of 8 objects, shown in Figure 5.1. The 2MS sample is a survey of photometric observations, and those values were used directly. The 2MS sample is considerably larger (21 objects), however the selection criterion of the data are unknown. The $B-R$ colors of the 2MS sample are shown in Figure 5.2. Each of these KBO color sample populations is compared to a set of synthetic detections.

Two sets of criterion were used to classify the sample objects into Hot and Cold subpopulations. One classification scheme is based on their q and a values and the other is based on a cut in i. For the q criterion, cKBOs with $35 < q < 40$ AU are placed in the Hot subpopulation and those with $q > 40$ AU and $42.5 < a < 47.2$ AU in the Cold. For the i criterion, Hot cKBOs have $i > 7°$ and Cold ones have $i < 4°$. A gap in the inclination cuts for this criterion minimizes possible contamination between the subpopulations. All orbital parameters used in these classifications were taken from the Minor Planet Center database.

5.4 Methods

We created model KBO populations and color distributions in order to compare the sample populations with the color distribution models. Different synthetic KBO populations were created for the CFEPS and 2MS observations. The synthetic objects were assigned colors based on color distribution models to create the H-Model and the Class-Model. We also included the effect of photometric biases, resulting from observing the intrinsic population, into our synthetic detection models. These models, incorporating KBO orbital characteristics, $B-R$ color, and measurement bias, were used to test the consistency of the observations with color distribution models.

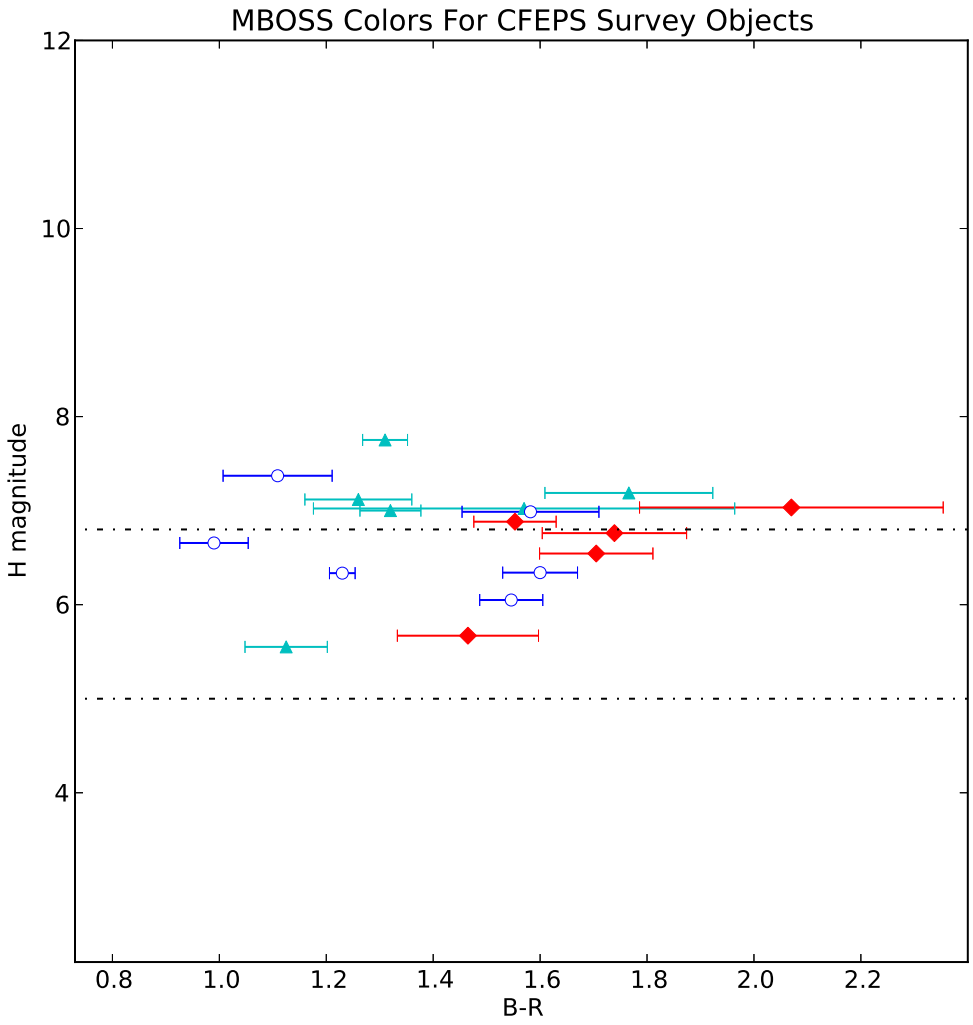

Figure 5.1 CFEPS KBO detections are cross referenced with the MBOSS color database. Hot objects are marked by triangles, Cold objects are marked with diamonds, and Resonant objects are shown as open circles. The classical objects have been classified using their q and a values, as described in the text. The horizontal lines indicate the regions of different $B - R$ color distribution according to the H-Model.

5.4.1 Model Populations

The L7 synthetic model provides a reasonable representation of the intrinsic Kuiper Belt (Petit et al., 2011). Using the CFEPS L7 characterization and the input L7 model, we build a simulated sample of detected CFEPS KBOs. For these simulated

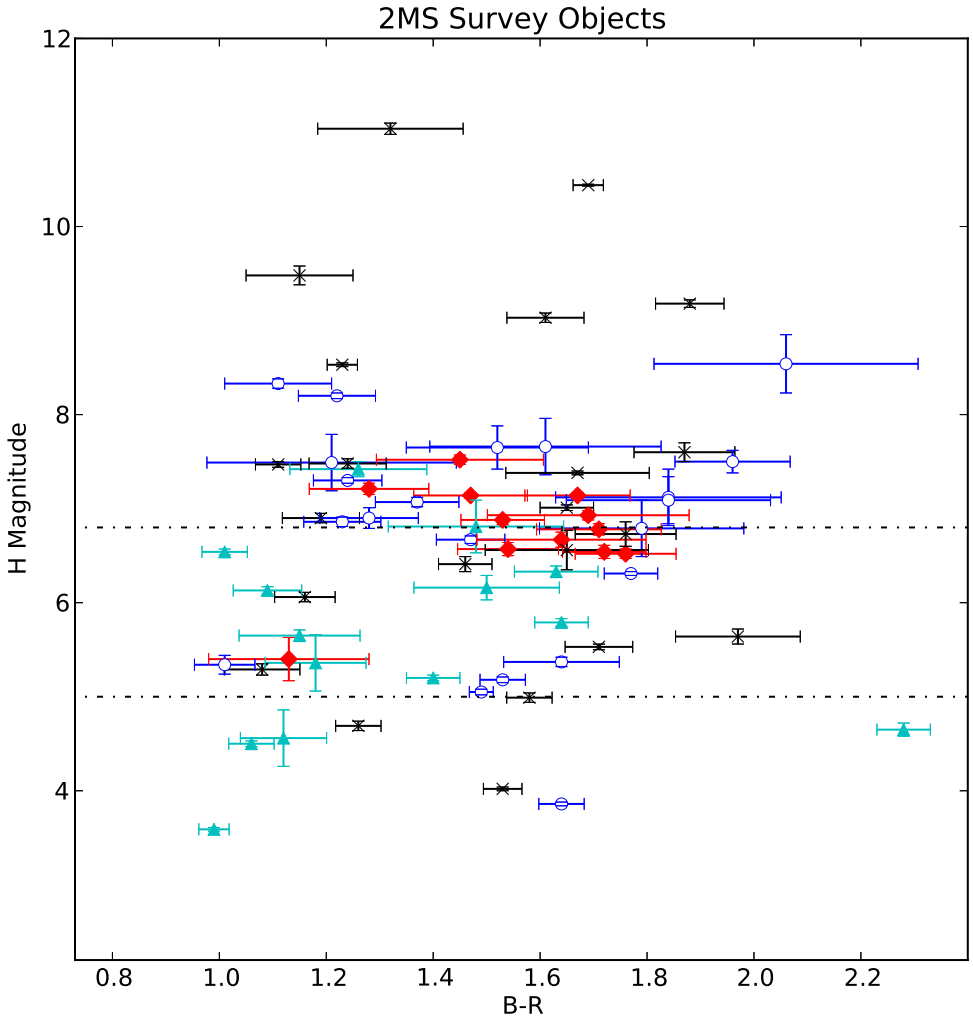

Figure 5.2 The Meudon Multicolor Survey objects are indicated by the same symbols as in Figure 5.1. Other object types, such as Centaurs, are marked with an 'x'. The Cold objects primarily cluster around $B-R$ of 1.6. The Hot object at a H magnitude of 4.6 and $B-R$ of 2.3 appears to be an outlier and was excluded from the analysis. The horizontal lines indicate the regions of different $B-R$ color distribution according to the H-Model.

detections, the orbital elements, H magnitudes, and dynamical classifications of the objects are known. The expected flux and H magnitude measurement uncertainties are modeled. This process allows us to understand the photometric biases present in

the CFEPS cKBO color samples.

For the 2MS sample, a bootstrapped comparison population was derived. The selection biases introduced in the 2MS discovery methods are not known. Because the objects were not discovered in a systematic survey, the 2MS objects did not have a representative distribution of H magnitudes. The synthetic detections were created by resampling the actual objects from within their H magnitude uncertainties. This generated a large model population for comparison, which could be assigned colors based on H magnitude and orbital parameters representative of the 2MS data.

The cKBOs were selected from the synthetic populations, and classified into Hot and Cold objects. (Resonant objects are highly sensitive to survey characteristics and are excluded from our analysis.) Different classification schemes for the CFEPS and 2MS synthetic detection models were required because of the different methods used to create the models. For the CFEPS synthetic objects, we used the known model classifications (Petit et al., 2011). The 2MS synthetic objects were classified in the same way as the 2MS data, based on their q, a, and i values. These theoretical model populations provide a good match to the Kuiper belt orbital distribution as sampled by the data and were used as our Hot and Cold comparison populations for modeling the various $B-R$ color distributions.

5.4.2 H Magnitude Color Model

The $B-R$ color distribution of the H-Model depends on the H magnitude of the objects, as described in Peixinho et al. (2012). Three different H magnitude ranges were identified. Peixinho et al. (2012) determined that objects with $H > 6.8$ and the objects with $H < 5.0$ were bimodal, while the intermediate H magnitude objects were found to be unimodal. The bimodal low and high H magnitude populations also had different $B-R$ peak values defining their distribution. For the $H > 6.8$ objects we used a bimodal $B-R$ color distribution with peaks at 1.2 and 1.8, each represented by a gaussian with a standard deviation of 0.125 magnitudes. The intermediate H objects were modeled as a single broad distribution centered at $B-R$ of 1.6 with a standard deviation of 0.33 magnitudes. The $H < 5$ objects had peak $B-R$ values of 1.05 and 1.6 with standard deviations of 0.1 magnitudes. $B-R$ colors were generated randomly from these distributions, and assigned to the synthetic objects in the model populations based on their H magnitudes to create the H-Model.

5.4.3 Classification Color Model

The second $B-R$ color model assumes that the color distribution of the KBOs is based on the objects' dynamical classification. We used a color distribution with a red peak at $B-R$ of 1.55 with a standard deviation of 0.1, and a blue peak at $B-R$ of 1.15 with a standard deviation of 0.12 magnitudes. These parameters were selected to match the color distribution of 2MS objects in Figure 5.3. The 2MS data have two peaks, however, the data in Figures 5.1 and 5.2 suggest that the Cold population lacks a blue component. We modeled the Cold objects' color distribution with a unimodal red peak, and for the Hot objects we sampled the bimodal distribution. The distribution of $B-R$ colors for the 2MS sample and the classification based color models are shown in the histogram in Figure 5.3. The $B-R$ colors were assigned to the synthetic objects in the model populations based on their classifications to create the Class-Model.

5.4.4 Color Magnitude Bias Model (CMB)

In addition to a survey detection bias, the precision of the measured $B-R$ magnitudes will introduce an observational bias because of the brightness of the target objects. Color surveys of KBOs generally select objects that appear bright enough in R band for photometry. However, for two equally bright objects in R, redder objects have higher B magnitudes, and are therefore more difficult to measure. The 2MS data were used to derive a relationship between larger magnitude uncertainties and increasing R magnitude, and these model uncertainties were then applied to the Class-Model and H-Model synthetic colors. A $\sim$0.4 magnitude separation of the two color peaks in the model suggests that photometric precision is required to successfully detect the bimodality of the intrinsic population. The KBOs with $\delta(B-R) > 0.15$ were considered un-measurable due to their large photometric uncertainty and removed from both of the color models. The remaining objects were assigned magnitude values within their error bars from the R magnitude error model. These observable objects and colors with photometric error included were used to create new color models for both the H-Model and Class-Model, and are referred to as the color measurement biased models (CMB).

Once the photometric uncertainty cut is applied to the model, the new CMB models show a clear correlation between classification and H magnitude, for both the H and Class -Model samples. The different physical locations of the different classes

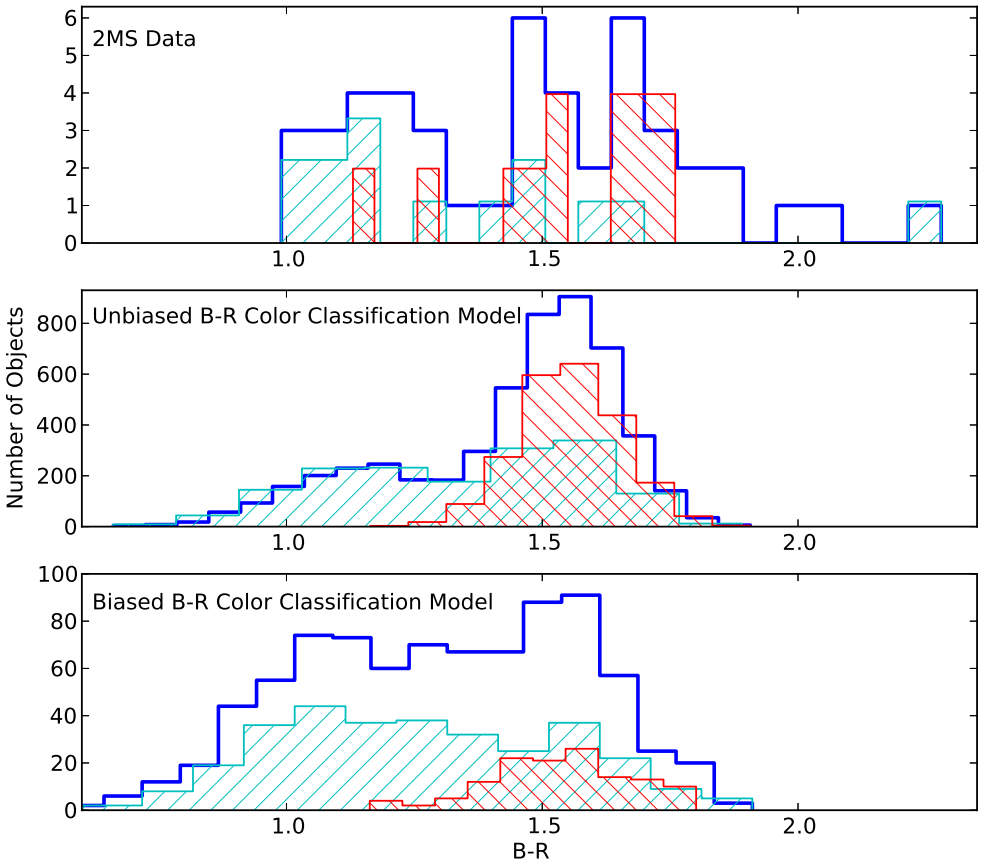

Figure 5.3 Panel 1: The 2MS object $B-R$ magnitudes. The complete sample (thick line) includes only the Hot (thin line with '/'), Cold (thin line with '\'), and Resonant objects (not plotted separately). The very red objects that are not well described by the model include an excluded Hot object and Resonant objects not considered in this analysis. Panel 2: The Class-Model with Hot and Cold objects. Panel 3: The Class-Model with color measurement bias.

of objects make larger-H objects in some classes easier to detect than others. This is evident even in the 2MS data in Figure 5.2, where the larger-H objects are all centaurs. In the models, the faintest objects predicted, with H magnitudes greater than 7.5, are almost entirely Resonant objects. A mix of Resonant and Hot objects are found between H magnitudes of 6.75 to 7.5, and the detectable Cold objects almost all have H magnitudes below 6.75. The observing biases caused by photometric detection limits and H magnitude dependence make it more difficult to understand the nature

of the underlying population.

5.4.5 Statistical Tests

We used the Anderson-Darling (AD) test to compare the samples, as in CFEPS (Kavelaars et al., 2009). Similar to the Kolmogorov-Smirnov (KS) test, the AD statistic computes the maximum distance between two distributions, however, the AD statistic (D) is weighted (see section 2.5 for details). In order to determine the significance of the AD statistic value, a bootstrapping method was used. The significance of rejection of the null hypothesis, where the distributions are identical, was calculated by comparing the real object D statistics with the input model D statistics.

To mitigate the effect of precise sample values in our observational data, the AD D value was calculated for photometric measurements consistent with the uncertainty associated with the data. For each object, the magnitude measurements were randomly assigned a value within their reported uncertainty range, and then the AD D values was computed. This process was then repeated 1000 times. The mean and the standard deviation of the range of D statistic values generated from the resampled data were compared to the D statistic range found using the synthetic models. This gave the probability that the observations, with measurement uncertainties, could be from the synthetic color models.

5.5 Results

Tables 5.1 and 5.2 show the agreement of observations with the different $B-R$ models used. The results for the color models are given, with and without the addition of the CMB. Both the H-Model (color distributions based on H magnitude) and the Class-Model (colors based on object type) were compared to the CFEPS objects and the 2MS data, using both orbital subpopulation classification criteria. The $B-R$ distributions of Hot and Cold objects observed were compared separately against the model Hot and Cold objects. The use of q or i classification scheme is as indicated in Tables 5.1 and 5.2. The range of statistical significance given in the tables provides an indicator of the robustness of the results; large ranges are primarily a result of an insufficient number of precise $B-R$ color measurements of real objects. Low significance values, in bold in the table, indicate that the observed $B-R$ color

distribution is unlikely to have been derived from the referenced theoretical model.

Table 5.1 Statistical Test Results: Hot cKBOs

Model	CFEPS (q)	2MS (q)	CFEPS (i)	2MS (i)
H-Model	10^{20}_{10}	$\mathbf{0.2}^{0.2}_{0.2}$	40^{40}_{30}	$\mathbf{0.9}^{1}_{0.6}$
H-Model & CMB	20^{40}_{20}	$\mathbf{0.7}^{0.9}_{0.4}$	70^{90}_{50}	$\mathbf{3}^{5}_{2}$
Class-Model	20^{40}_{20}	20^{30}_{10}	80^{90}_{60}	30^{40}_{20}
Class-Model & CMB	40^{50}_{30}	80^{90}_{60}	80^{90}_{70}	90^{90}_{70}

The numbers represent the percentage of times the Anderson-Darling D statistic for the observed sample was larger than the bootstrapped input model. The bold values indicate the model is statistically rejected. See text for details.

Table 5.2 Statistical Test Results: Cold cKBOs

Model	CFEPS (q)	2MS (q)	CFEPS (i)	2MS (i)
H-Model	30^{40}_{30}	5^{10}_{5}	40^{60}_{30}	9^{10}_{7}
H-Model & CMB	$\mathbf{4}^{6}_{2}$	$\mathbf{0}^{0.1}_{0}$	6^{10}_{4}	$\mathbf{1}^{2}_{0.5}$
Class-Model	30^{50}_{4}	$\mathbf{3}^{20}_{0.4}$	$\mathbf{0.7}^{10}_{0}$	$\mathbf{3}^{20}_{1}$
Class-Model & CMB	40^{60}_{10}	6^{20}_{2}	5^{20}_{1}	6^{20}_{2}

5.6 Discussion

We have used two independent approaches to classification of cKBOs into Hot and Cold subpopulations: a q based selection criterion and an i based criterion. These two approaches classify the majority of objects into the same subpopulations, with a few sources moving between categories. The q criterion was chosen to reflect the orbit model generation process as described in the appendix of Petit et al. (2011) while the i selection criterion is common in the literature. We also explored various i cuts and boundaries, none of which resulted in a significant variation in our results. The acceptance/rejection of various theoretical models was not found to be dependent on the classification criterion.

The results for the Hot cKBO population provide some insight into the underlying population distribution. The CFEPS data is inconclusive due to the small number

statistics. However, the 2MS data appears to reject the H-Model, with and without the inclusion of the CMB. We also find that while the classification scheme does not change the overall rejection or acceptance of the models, the q based classification sharpens the rejection of the H-Model. A classification based model is not rejected for the Hot objects, and, with the inclusion of the CMB, the Class-Model is an excellent match with the data.

The $B - R$ color distribution of Cold cKBOs have different compatibility issues when compared with the models. The H-Model is only rejected with the inclusion of the CMB. The CMB improves the acceptability of the Class-Model, however this model still does not provide a satisfying match to these data. The lack of goodness of fit of the unimodal distribution in the Class-Model is likely due to the four KBOs with $B - R < 1.3$ (see Figure 3). The inclusion of the color measurement bias expands the expected color range to include half of these objects, but these four color measurements have acceptable photometric uncertainties, which suggests that the unimodal idea for the Cold objects may require revision. The Cold KBOs have a steep size distribution, and bluer KBOs have lower average albedos than red KBOs. This could introduce an additional sampling bias, that would cause a bimodal population of small objects to appear primarily red. The difficulty in understanding the inherent Cold object color distribution may be primarily a selection effect.

The application of combined datasets of KBO colors to understand inherent relationships between different KBO properties is a complicated process. Understanding the selection effects and biases introduced by different survey procedures is difficult, if not impossible, and assumptions about these effects can influence the apparent acceptability of color distribution models. The effects of KBO albedo may also result in an oversampling of red objects, and with the combination of these unknown effects we believe it is premature to claim conclusive trends in size-color relationships of KBOs.

Chapter 6

Colors as a Probe of the Origin of the 5:1 Resonators

This chapter contains preliminary work on TNO colors. As part of the Colors of the Outer Solar System Origins Survey (Col-OSSOS; PI: Dr. Wesley Fraser) international collaboration, I have contributed to this large survey project. I have executed observations on one of the observing runs and done the image preparation for all of the optical photometry. I have also measured the photometry of the Subaru data as well as the Gemini 5:1 optical data (from my own program with Dr. J.J. Kavelaars). Dr. Wesley Fraser calculated the color conversion between SDSS and the Subaru and Gemini filters. The photometry measurements for the Col-OSSOS g, r, and J band data were done by Michaël Marsset and Dr. Wesley Fraser. Light curve corrections for the Col-OSSOS targets were calculated by Dr. Megan Schwamb. Team members have contributed to observing proposals and Gemini observing. We have refined our photometric methods and expect to begin publication of several survey papers in the Fall of 2016, including the first data release and survey overview. I will contribute a paper based on the preliminary z band results presented here.

6.1 Introduction

One of the early features discovered in the Trans-Neptunian Objects (TNOs) in the outer Solar System was that these objects had a large range of surface colors. Early work suggested that TNO colors were bimodal in $B-R$ (Tegler et al., 2003), and the colors of centaurs are clearly bimodal in $B-R$ (Peixinho et al., 2003; Tegler et al.,

2003). However, recent work suggests that color distributions of TNOs (including centaurs) may also be dependent on object H-magnitude and bimodal for small TNOs (Fraser & Brown, 2012; Peixinho et al., 2012, 2015). The vast majority of TNOs are too faint for spectroscopic studies of surface composition, so the surface reflectance of TNOs is used to provide constraints on surface composition. TNOs in general have red optical colors in g, r, and i bands; even the 'neutral' TNOs are slightly redder than solar colors. Because of the unknown biases inherent in the known TNO sample, determining the relative population sizes of different surface types (and even detection sensitivity for different surface types) from the current published colors is not possible (Pike & Kavelaars, 2013).

Except for the brightest TNOs, the majority of color measurements are in the optical wavelengths. B, V, R, and I measurements are available in the literature for a large number of TNOs (Hainaut & Delsanti, 2002), however the compiled literature color measurements provided may not come from concurrent photometry, and thus may suffer from light curve and phase effects. TNOs have also been explored in H band, which probes methane and ice absorption. A few samples have been studied with Hubble Space Telescope, which can cover optical and near-infrared imaging, including the $\sim 1\mu$m filter (e.g. Fraser et al., 2015). In part due to detector sensitivity, z band photometry has not been utilized as a tool for probing TNO surface types, however this wavelength range is sensitive to the presence or absence of organics and silicates on minor planet surfaces (Ivezić et al., 2001).

The composition of TNOs has been the subject of much investigation; constraining the surface composition of TNOs is challenging. Large TNOs can be studied spectroscopically, and approximately half of the 40 objects with published spectra show absorption in ice or ices (such as methane, nitrogen, water, ammonia, and CH_3OH; Barucci et al., 2008). Spectroscopic results have also shown indications of aqueous alteration of silicates (Fornasier et al., 2004). Low resolution spectroscopy of 15 TNOs found that all the TNOs studied exhibited some water ice, either in a pure form, or mixed with a red component (Brown et al., 2012). Near-infrared photometry and low resolution spectra of the dwarf planet 2007 OR10 show a water absorption feature and a very red optical slope; this reddening is expected to be a substance such as irradiated methane (Brown et al., 2011). Fraser & Brown (2012) explored a range of two component red and neutral mixtures, and found that all small dynamically excited TNOs show a color bifurcation. Detailed modeling of surface composition has been attempted; using organic tholins produces the red surface colors of TNOs

(Cruikshank et al., 2003), but precise mixing models cannot be effectively constrained until the surface materials of the objects are clearly identified.

The most significant weakness of previous color distribution samples is the biases in sample selection. Because the TNOs are selected based on unknown criteria (likely a combination of brightness, on sky availability, weather, telescope scheduling, etc.), the fraction of TNOs of a particular surface type is likely not representative of the underlying population (Pike & Kavelaars, 2013). The recent Outer Solar Systems Origin Survey (OSSOS, Bannister et al., 2016) on the Canada-France Hawaii Telescope (CFHT) is a large TNO discovery survey which provides an opportunity to measure the surface features of a large sample with known discovery biases. As part of the Colors of OSSOS (Col-OSSOS) collaboration, I contributed to the design of a large photometric survey (Schwamb et al., 2016). This Large Program on Gemini North is obtaining g, r, and J band photometry of a flux limited subset of the OSSOS TNO sample, ensuring that the sample biases are well understood. The precision photometry has $\leq$5% uncertainty, which is necessary to distinguish between different possible surface types (Fraser & Brown, 2012; Dalle Ore et al., 2013). The sample selection and precision of the simultaneous multi-band photometry will make Col-OSSOS a powerful legacy color survey of TNOs.

6.2 Simultaneous Observations from Gemini and Subaru Observatories

The Col-OSSOS project uses Gemini Observatory to acquire g, r, and J band photometry of all OSSOS discoveries with $r < 23.6$. These data are being augmented by observations in z and i band from Subaru and u band from CFHT. This project will create a legacy color survey of the Kuiper belt, capable of addressing the colors of TNOs with statistically meaningful methods. Col-OSSOS observations span August 2014 to 2017, targeting 30-40 TNOs per semester.

The Col-OSSOS observations discussed in this work were obtained at Gemini Observatory and Subaru Telescope. The Gemini optical data was acquired with the Gemini Multi-Object Spectrographs (GMOS) North in imaging mode, and the J band data was acquired using the Near InfraRed Imager and Spectrometer (NIRI). During the first semester of observing, several i band images as well as z band data for the majority of the targets were also acquired using GMOS and Subaru Suprime-

Cam. These additional wavelengths add an exploratory component to this large color survey.

The observations reported here were acquired from Subaru Telescope and Gemini Observatory. The OSSOS targets were observed during the Col-OSSOS observing runs and fit the selection criteria of the Col-OSSOS sample, a flux limited subsample of the OSSOS discoveries. I also used a Gemini Observatory Fast Turnaround program to acquire g, r, and z band photometry of the three known 5:1 resonant objects (Pike et al., 2015). These three objects are within the flux limit of the Col-OSSOS sample, and also provide a complete sample of the known 5:1 objects. All of these TNOs were discovered in characterized surveys, OSSOS (Bannister et al., 2016) and the Canada-France Ecliptic Plane Survey (CFEPS, Petit et al., 2011; Kavelaars et al., 2008). The Col-OSSOS sample can thus be used as a comparison sample to interpret the colors of the 5:1 resonators.

6.2.1 Observations

Data were acquired using both Subaru and Gemini Observatories and prepared according to the reduction pipeline instructions. On Subaru, the observations included Rc, i, and z band photometry with Suprime-Cam. The Suprime-Cam images were reduced using Subaru's automated pipeline, which includes a bias subtraction, flat field correction, and a distortion correction. The CCD chips containing the TNOs were selected from each set of observations; some observations included multiple TNOs within the field of view. The GMOS images were prepared using the Gemini IRAF package in Ureka. This includes a bias subtraction, flat field correction, and a mosaic routine to combine the different chips into a single extension. Master flats were also produced for the Col-OSSOS observations and used to produce a better flat correction.

The list of targets for which z band was acquired is in Table 6.1 and Table 6.2. The g, r, and J band photometry for the Col-OSSOS targets is discussed in Schwamb et al. (2016). The majority of the z band measurements were taken from Subaru; targets O13BL3RG, O13BL3TF, and O13BL3TA also have z band data from GMOS. The photometry of the 5:1 resonators is presented for the first time in this work. These objects were discovered in ecliptic and the high latitude component of the CFEPS survey (Petit et al., 2011; Kavelaars et al., 2008), and details of their classification are discussed in Pike et al. (2015).

Table 6.1 Col-OSSOS Target List

OSSOS ID	Col-OSSOS ID	a (AU)	e	i (degrees)	OSSOS r' mag	H_r mag	r (AU)
o3l79	O13BL3TA	46.33 ± 0.17	0.168 ± 0.012	8.48 ± 0.00	22.79 ± 0.04	5.75	50.54 ± 0.00
o4h50	Col3N01	43.71 ± 0.00	0.066 ± 0.000	4.49 ± 0.00	22.68 ± 0.04	6.00	46.56 ± 0.00
o3l77	O13BL3RE	42.76 ± 0.06	0.113 ± 0.002	27.34 ± 0.01	22.96 ± 0.17	6.10	47.53 ± 0.00
o3l76	O13BL3TF	44.10 ± 0.09	0.088 ± 0.007	3.47 ± 0.00	23.12 ± 0.06	6.37	47.30 ± 0.00
o3l43	O13BL3QX	45.82 ± 0.11	0.100 ± 0.010	2.02 ± 0.00	23.02 ± 0.11	6.59	43.04 ± 0.00
o3l39	O13BL3RB	43.61 ± 0.15	0.068 ± 0.018	4.18 ± 0.00	22.96 ± 0.06	6.59	42.48 ± 0.00
o4h45	Col3N03	43.37 ± 0.01	0.130 ± 0.001	3.66 ± 0.00	23.07 ± 0.05	6.61	44.31 ± 0.00
o3l57	O13BL3RH	45.08 ± 0.14	0.079 ± 0.016	1.84 ± 0.00	23.30 ± 0.08	6.74	44.40 ± 0.00
o3l63	O13BL3RG	45.23 ± 0.12	0.067 ± 0.015	3.36 ± 0.00	23.63 ± 0.21	7.01	45.09 ± 0.00
o3l46	O13BL3S3	46.61 ± 0.02	0.076 ± 0.007	2.47 ± 0.00	23.61 ± 0.09	7.15	43.42 ± 0.00
o4h20	Col3N06	46.35 ± 0.01	0.199 ± 0.000	7.95 ± 0.00	22.97 ± 0.06	7.18	37.95 ± 0.00
o4h31	Col3N07	44.48 ± 0.00	0.099 ± 0.000	18.29 ± 0.00	23.26 ± 0.09	7.22	40.15 ± 0.00
o3l15	O13BL3SY	38.29 ± 0.03	0.018 ± 0.007	19.84 ± 0.00	23.41 ± 0.17	7.52	38.74 ± 0.00
o3l06	O13BL3SH	42.27 ± 0.07	0.253 ± 0.004	2.67 ± 0.00	22.69 ± 0.07	7.54	32.73 ± 0.00
o3l09	O13BL3RN	36.38 ± 0.01	0.070 ± 0.005	2.02 ± 0.00	23.22 ± 0.16	7.76	34.45 ± 0.00
o4h01	Col3N02	23.18 ± 0.01	0.377 ± 0.000	21.32 ± 0.00	22.71 ± 0.10	10.26	17.76 ± 0.00
o3l01	O13BL3RQ	55.87 ± 0.09	0.719 ± 0.001	22.25 ± 0.00	23.06 ± 0.07	10.89	16.05 ± 0.00

Table 6.2 5:1 Resonator Target List

CFEPS ID	MPC ID	a (AU)	e	i (degrees)	CFEPS mag	H_g (H_r) mag	r (AU)
L3y02	2003 YQ_{179}	88.41±0.02	0.57866±0.00008	20.874±0.000	23.38±0.09 (g)	7.3 (∼6.6)	39.3
HL7c1	2007 FN_{51}	87.49±0.07	0.6188±0.0004	23.237±0.000	23.20±0.06 (r)	∼7.7 (7.2)	39.1
HL7j4	2007 LF_{38}	87.57±0.03	0.5552±0.0002	35.825±0.000	22.53±0.09 (r)	∼6.0 (5.5)	48.4

6.2.2 Photometry

Precision photometry is a goal of the Col-OSSOS project. Flux measurements were made on the calibrated images using a customized aperture correction method (Fraser et al., 2016). The images were acquired using sidereal tracking, with exposures of $\leq$ 300 seconds, so trailing due to object motion is minimal. However, the precision photometry requires uncertainties on the order of a few percent in order to differentiate between different surface type groups (Fraser & Brown, 2012; Dalle Ore et al., 2013), so a precise photometric measurement is necessary.

For TNOs (and other Solar System objects) the object motion creates a complication. To measure the target and reference star flux, we use aperture photometry because a point spread function (PSF) fitting method is less accurate for moving sources as a result of distortions caused by variable seeing. To accurately measure flux, one can track at half the TNO rate of motion so that the stars and TNO have a PSF variability, or track the stars and model the TNO motion using a non-circular aperture. The custom-designed pill-shaped aperture uses the known rate of motion of the TNO relative to the stellar tracking to minimize trailing losses (Fraser et al., 2016). The pill-shaped aperture correction technique results in a PSF uncertainty less than 0.01 magnitudes as a result of incorrect PSF information of the trailed source. Properly accounting for object motion significantly reduces the uncertainty in object measurements. The resulting photometry is reported in Tables 6.3 and 6.4.

6.2.3 SDSS Color Calibration

Even when the same Sloan filters are selected, the filter bandpasses for Subaru and Gemini are not identical. The differing efficiencies over their filter wavelength coverage is a result of telescope optics and instrument sensitivity. In order to combine data from the two telescopes, it is necessary to properly characterize the flux measurement of each telescope and scale the magnitude to a common reference frame.

The Col-OSSOS data are scaled to the Sloan Digital Sky Survey (SDSS) magnitudes. Stars on the science images with magnitudes in the SDSS system were used to calculate the conversion between the SDSS system and the GMOS and Suprime-cam filter systems. The effect of the transform depends on the color of the TNO, so the correction is computed for each object. The GMOS photometry on Gemini (r_G, g_G, z_G) is converted to SDSS (r_{SDSS}, g_{SDSS}, z_{SDSS}) using the following relations:

$$r_G = r_{SDSS} - 0.051 \times (g_{SDSS} - r_{SDSS}) \tag{6.1}$$

$$g_G = g_{SDSS} - 0.146 \times (g_{SDSS} - r_{SDSS}) \tag{6.2}$$

$$z_G = z_{SDSS} \tag{6.3}$$

The Subaru data (Rc_S, z_S, i_S) is converted to SDSS filters according to these relationships:

$$Rc_S = Rc_{SDSS} - 0.044 \pm 0.023 \times (g_{SDSS} - r_{SDSS}) \tag{6.4}$$

$$i_S = i_{SDSS} - 0.096 \pm 0.019 \times (g_{SDSS} - r_{SDSS}) \quad (6.5)$$

$$z_S = z_{SDSS} - 0.077 \pm 0.034 \times (g_{SDSS} - r_{SDSS}) \quad (6.6)$$

An additional color term was used to convert Rc_{SDSS} to r_{SDSS} from Jordi et al. (2006).

$$Rc_{SDSS} - r_{SDSS} = (-0.153 \pm 0.003) * (r_{SDSS} - i_{SDSS}) - (0.117 \pm 0.003) \quad (6.7)$$

Three of our targets have consistent duplicate z band measurements, one taken from Subaru and one from Gemini (see Table 6.6). The consistency of the measurements regardless of the telescope used demonstrates the success of this method. Tables 6.3 and 6.5 present the TNO magnitudes in the SDSS filters.

6.2.4 Determining Colors from TNO Photometry

An accurate color determination requires multi-band photometry taken within a short timescale to mitigate light curve and phase effects. Where possible, the Subaru photometry was taken simultaneously with the Gemini photometry. However, in some cases an additional Rc or r band observation was taken from either Subaru or Gemini so that an $r-z$ color could be determined separately. The r value used in the $r-z$ color was the measurement that was acquired temporally closest to the z band observation. A few z band measurements lack an associated r measurement within ± 0.5 hours; these are included in the photometry Table 6.3 for completeness, but no $r-z$ color is reported. More precise knowledge of the light curve may enable us to constrain the color of these objects in $r-z$ in the future.

The TNO colors are reported in Table 6.6. The z band flux measurements are not as precise as the optical colors from the main Col-OSSOS survey observations. The serendipitous opportunity to acquire the additional z band data resulted in a variety of photometric uncertainties in these measurements. The effects of combining observations from multiple nights for some targets is also reflected in the reported measurement uncertainties in Table 6.6.

6.3 Results

The color measurements of these objects show that z band measurements increase the distinction between different surface types when combined with the g, r, and J band

Table 6.3 TNO Photometry Sequences from Subaru in SDSS Magnitudes

Col-OSSOS ID	OSSOS ID	MPC ID	Filter (SDSS)	Magnitude	MJD	Exposure Time (s)
Col3N01	o4h50	...	i	22.36 ± 0.03	56894.40706	150
Col3N01	o4h50	...	z	22.13 ± 0.05	56894.41911	150
Col3N01	o4h50	...	z	22.14 ± 0.07	56897.42265	150
Col3N01	o4h50	...	Rc (r)	22.67 ± 0.03	56894.42717	150
Col3N01	o4h50	...	Rc (r)	22.41 ± 0.03	56894.42717	150
Col3N03	o4h45	...	z	22.81 ± 0.13	56897.42265	150
Col3N02	o4h01	...	z	22.57 ± 0.10	56897.42053	150
Col3N06	o4h20	...	z	22.94 ± 0.15	56897.42265	150
Col3N07	o4h31	...	z	23.12 ± 0.17	56897.42481	150
O13BL3QX	o3l43	...	i	22.52 ± 0.04	56892.40975	150
O13BL3QX	o3l43	...	z	22.29 ± 0.08	56892.41698	150
O13BL3QX	o3l43	...	Rc (r)	22.72 ± 0.04	56892.42619	150
O13BL3QX	o3l43	...	Rc (r)	22.51 ± 0.04	56892.42619	150
O13BL3RB	o3l39	...	z	22.32 ± 0.07	56895.41934	150
O13BL3RB	o3l39	...	z	22.54 ± 0.13	56896.41319	150
O13BL3RB	o3l39	...	Rc (r)	22.72 ± 0.04	56896.42616	150
O13BL3RB	o3l39	...	Rc (r)	22.34 ± 0.04	56896.42616	150
O13BL3RG	o3l63	...	z	23.20 ± 0.16	56895.42145	150
O13BL3RN	o3l09	...	z	22.60 ± 0.09	56897.41821	150
O13BL3RQ	o3l01	...	i	22.90 ± 0.06	56894.40391	150
O13BL3RQ	o3l01	...	z	22.75 ± 0.11	56894.41690	150
O13BL3S3	o3l46	...	z	23.55 ± 0.29	56896.41111	150
O13BL3SH	o3l06	...	i	22.42 ± 0.04	56892.40761	150
O13BL3SH	o3l06	...	z	22.17 ± 0.06	56892.41914	150
O13BL3SY	o3l15	...	z	23.33 ± 0.21	56897.42720	150
O13BL3RE	o3l77	...	z	21.04 ± 0.24	56897.41603	150
O13BL3TF	o3l76	...	z	20.38 ± 0.27	56896.40887	150

measurements for the TNOs. These color measurements are shown in Figure 6.1. The $r-z$ colors of the objects span a large range of values, ~ 0.6 magnitudes. This is a similar range to the $g-r$ colors of TNOs. In the plot of $r-z$ versus $g-r$, clusters of different surface colors become apparent. The variations in color are an indicator of variation in surface properties. The bi-modality is strongly linked to the previously known $g-r$ bi-modality, and indicates at least two distinct surface compositions are present.

The addition of TNO dynamical classifications based on orbital parameters provides a more complete picture. The Col-OSSOS TNOs are divided into dynamically excited objects and cold classical objects. The orbital distributions of cold classical objects and hot classical objects overlap, so the objects identified in Figure 6.1 as

Table 6.4 TNO Photometry Sequences of the 5:1 Resonators from Gemini

CFEPS ID	MPC ID	Filter	Magnitude (Gemini)	MJD	Exposure Time (s)
L3y02	2003 YQ_{179}	r	22.91 ± 0.02	57308.63136	300
L3y02	2003 YQ_{179}	g	23.61 ± 0.04	57308.63533	300
L3y02	2003 YQ_{179}	z	22.50 ± 0.05	57308.63933	300
HL7j4	2007 LF_{38}	r	23.12 ± 0.02	57435.63929	200
HL7j4	2007 LF_{38}	g	23.59 ± 0.03	57435.64328	300
HL7j4	2007 LF_{38}	z	22.86 ± 0.04	57435.64728	300
HL7j4	2007 LF_{38}	r	23.10 ± 0.02	57435.65007	200
HL7c1	2007 FN_{51}	g	24.35 ± 0.03	57432.50984	300
HL7c1	2007 FN_{51}	g	24.25 ± 0.03	57432.51365	300
HL7c1	2007 FN_{51}	g	24.33 ± 0.03	57432.51746	300
HL7c1	2007 FN_{51}	r	23.69 ± 0.03	57432.52142	300
HL7c1	2007 FN_{51}	z	23.06 ± 0.04	57432.52536	300
HL7c1	2007 FN_{51}	z	23.11 ± 0.04	57432.52916	300
HL7c1	2007 FN_{51}	g	24.33 ± 0.03	57432.53317	300
HL7c1	2007 FN_{51}	g	24.42 ± 0.03	57432.53697	300
HL7c1	2007 FN_{51}	g	24.39 ± 0.04	57432.54078	300
HL7c1	2007 FN_{51}	z	23.25 ± 0.05	57432.54477	300
HL7c1	2007 FN_{51}	z	23.41 ± 0.07	57432.54858	300
HL7c1	2007 FN_{51}	r	23.68 ± 0.03	57432.55252	300
HL7c1	2007 FN_{51}	g	24.37 ± 0.04	57432.55649	300
HL7c1	2007 FN_{51}	g	24.29 ± 0.04	57432.56030	300
HL7c1	2007 FN_{51}	g	24.41 ± 0.05	57432.56410	300

Table 6.5 TNO Photometry of the 5:1 Resonators: Mean Magnitudes

CFEPS ID	MPC ID	Filter	Magnitude (Gemini)	Magnitude (SDSS)
L3y02	2003 YQ_{179}	r	22.91 ± 0.02	22.95 ± 0.02
L3y02	2003 YQ_{179}	g	23.61 ± 0.04	23.72 ± 0.04
L3y02	2003 YQ_{179}	z	22.50 ± 0.05	22.50 ± 0.05
HL7j4	2007 LF_{38}	r	23.11 ± 0.01	23.14 ± 0.02
HL7j4	2007 LF_{38}	g	23.59 ± 0.03	23.67 ± 0.03
HL7j4	2007 LF_{38}	z	22.86 ± 0.04	22.86 ± 0.04
HL7c1	2007 FN_{51}	r	23.68 ± 0.05	23.72 ± 0.05
HL7c1	2007 FN_{51}	g	24.35 ± 0.05	24.45 ± 0.05
HL7c1	2007 FN_{51}	z	23.18 ± 0.05	23.18 ± 0.05

Table 6.6 TNO Colors (SDSS) with propagated Poisson uncertainties

Survey ID	MPC ID	$g-r$ Gemini	$r-z$ Gemini	$r-J$ Gemini	$r-z$ Subaru
Col3N01	...	1.02 ± 0.01	...	1.83 ± 0.06	0.6 ± 0.12
Col3N02	...	0.64 ± 0.01	...	1.15 ± 0.07	0.77 ± 0.15
Col3N03	...	0.68 ± 0.01	...	1.35 ± 0.06	0.76 ± 0.19
O13BL3QX	...	0.86 ± 0.03	...	1.36 ± 0.06	0.27 ± 0.12
O13BL3RB	...	0.61 ± 0.02	...	1.39 ± 0.06	0.5 ± 0.12
O13BL3RE	...	0.55 ± 0.01	...	0.77 ± 0.08	0.32 ± 0.19
O13BL3RG	...	1.04 ± 0.04	0.42 ± 0.07	1.22 ± 0.09	0.52 ± 0.2
O13BL3RN	...	1.01 ± 0.02	...	1.41 ± 0.05	0.78 ± 0.13
O13BL3RQ	...	0.66 ± 0.04	...	1.72 ± 0.08	0.86 ± 0.16
O13BL3S3	...	0.88 ± 0.01	...	1.64 ± 0.08	0.15 ± 0.3
O13BL3SH	...	0.82 ± 0.04	...	1.78 ± 0.07	0.87 ± 0.09
O13BL3SY	...	0.63 ± 0.02	...	1.13 ± 0.08	0.43 ± 0.2
O13BL3TA	...	0.61 ± 0.01	0.38 ± 0.01	1.09 ± 0.11	0.31 ± 0.11
O13BL3TF	...	0.99 ± 0.03	0.49 ± 0.05	1.51 ± 0.06	0.40 ± 0.21
L3y02	2003 YQ_{179}	0.78 ± 0.05	0.44 ± 0.05	...	...
HL7j4	2007 LF_{38}	0.52 ± 0.04	0.29 ± 0.05	...	...
HL7c1	2007 FN51	0.67 ± 0.03	0.63 ± 0.03	...	...

cold classical TNOs are very likely cold classicals, but this population may include a small amount of contamination from the hot classical population. These cold classical TNOs were selected based on pericenters > 38 AU, semi-major axes 39.4–48 AU, and inclinations $< 6°$. The majority of these cold classical TNOs cluster in surface color in both color plots; they are red in $g-r$ and $r-J$. In $r-J$, the dynamical classification is necessary to identify the superimposed trends of the cold classical surfaces and dynamically excited TNO surfaces.

The dynamically excited TNOs include a neutral and red component in $g-r$. The red component is not well sampled in these data, and the reflectivity of these surfaces in z band should be explored in future work. The 'neutral' objects in $g-r$ ($g-r \lesssim 0.7$) show a trend of increased $r-z$ colors with increased $g-r$ colors, a continuation of the spectral slope found in g and r band reflectance. The dynamically excited TNOs show a trend of increasing z band with increasing J band measurements. This correlation for excited TNOs in z and J band is obscured if the cold classical objects are included.

I explore the surface reflectance of these objects in Figure 6.2. Reflectance, R, is an albedo ratio calculated by removing solar colors. The color, C, of a TNO is the

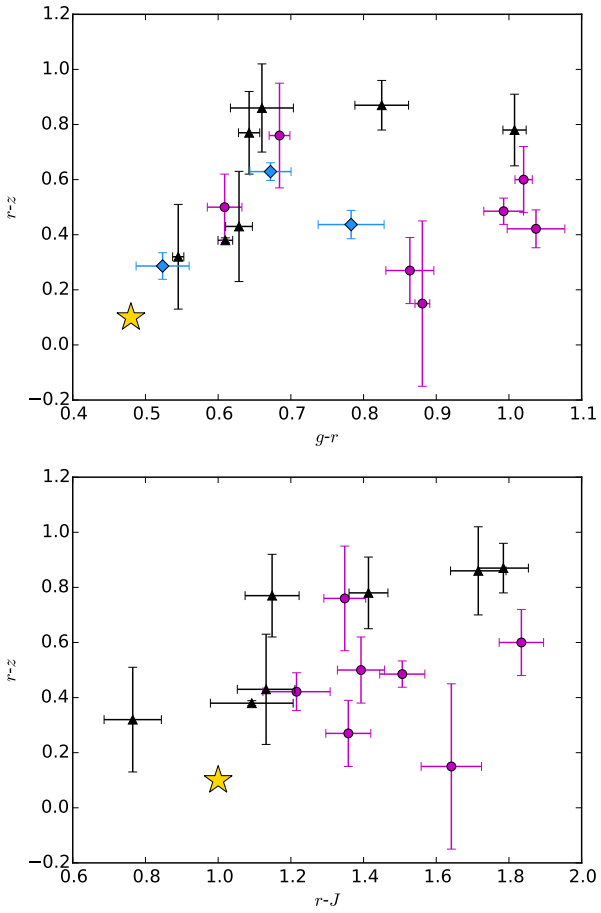

Figure 6.1 All Col-OSSOS targets with z band photometry, including dynamically excited TNOs (black triangles), cold classical TNOs (magenta circles), and the 5:1 resonators (blue diamonds), are shown here. Solar colors are indicated by the 'star'. From the upper plot, it is clear that $g-r$ and $r-z$ color show multiple populations with different correlations. The objects appear to clump in $(g-r)$ – $(r-z)$ space. These measurements indicate that z band assists in determining the $g-r$ color group in which the TNO belongs. The lower plot shows the range of $r-z$ compared to $r-J$ color; for the dynamically excited population, z and J band measurements are correlated.

magnitude difference, e.g. for $g-r$:

$$C = g - r = 2.5 \log(F_r/F_g). \tag{6.8}$$

The reflectance, $R = 10^{0.4(C_{Solar} - C_{TNO})}$, is thus a ratio of reflected flux from the TNO, F, and solar flux, f.

$$R = 10^{0.4 \times 2.5(\log \frac{f_r}{f_g} - \log \frac{F_r}{F_g})} = \frac{F_g/f_g}{F_r/f_r} \tag{6.9}$$

After this conversion to reflectance, I display the multi-band photometry as though they were very low resolution spectra. The different shapes of the spectral curves show that some g–r slopes predict the z band measurement while some do not. Reflectance in i band is highly predictable based on g–r slopes (see Sheppard, 2012, for examples). The behavior of J band in Figure 6.2 shows a range of behaviors, and needs to be carefully compared to the color-color plots. Nearly all TNOs identified as cold classical objects have a higher J band reflectance than z band.

The 5:1 resonators show a range of spectral slope in all measured filters. In Figure 6.1, these objects span a range of both $g - r$ and $r - J$ colors. One of these 5:1 resonators is the least-red object in our sample, and the others are more average in color. Two are clearly consistent with the neutral dynamically excited TNO surfaces in Figure 6.1. In Figure 6.2, the 5:1 resonators show three very different spectral shapes: a flat, convex, and concave spectral reflectance. These shapes are similar to some of the other objects in the sample.

6.4 Discussion

The variations seen in z band result from compositional differences of TNO surfaces. There are a wide range of $r - z$ colors for both the Col-OSSOS sample and the three 5:1 resonators. While these data are not sufficiently extensive or precise to test multi-component composition models, they show that z band explores a range of values relative to the optical g and r bands as well as the near-infrared J band, some of which is correlated. Based on materials speculated to cover TNO surfaces (ices, irradiated organics, and silicates), variation in the z band is expected and deviations from the expected spectral slope may be indicative of the presence of silicates.

6.4.1 TNO Surfaces in z band

The variation in z band color is indicative of TNO surface properties. In Figure 6.3, the laboratory spectra of multiple possible constituents are presented. The ‘tholin’

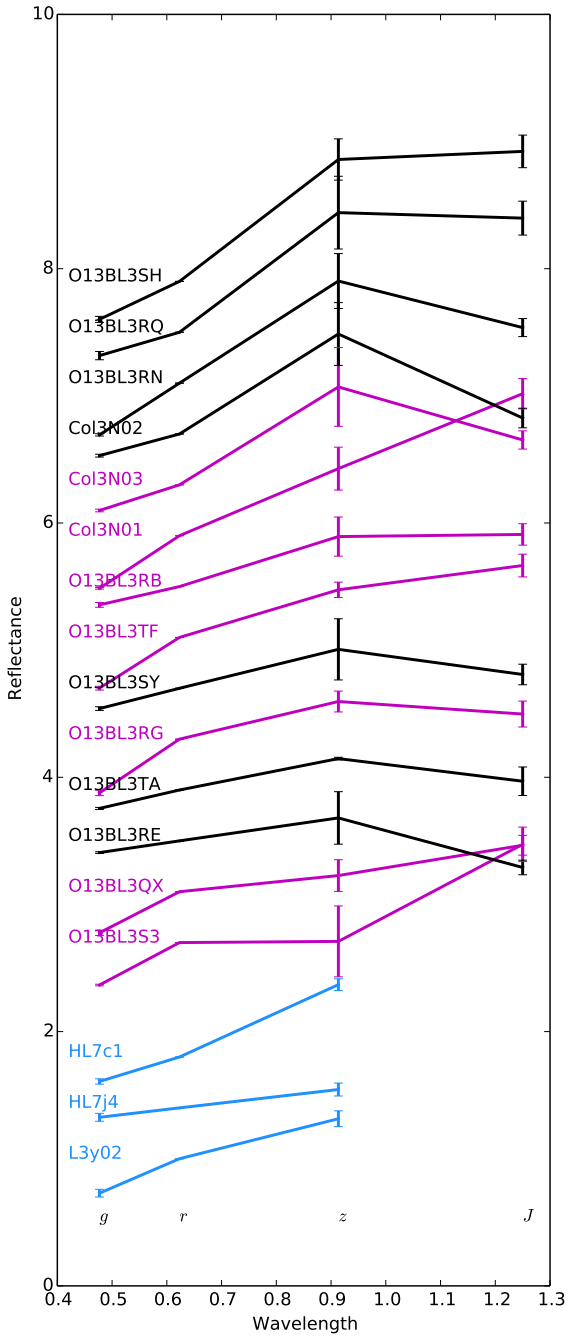

Figure 6.2 TNO reflectance spectra for the targets. All measurements are normalized; offsets have been added so individual objects can be identified. (The Col-OSSOS TNOs are sorted with the largest $r - z$ at the top.) A range of spectral shapes are visible here. In some cases, the z band color continues the g to r red slope, but for some TNOs, the z band is more or less reflective than the g and r measurement slope continuation. It is clear that TNOs can display similar reflectance in g, r, and z but different J band reflectance. The colors are the same as in Figure 6.1: dynamically excited TNOs– black, cold classicals– magenta, 5:1 resonators– blue.

material is an organic compound which has been reddened through irradiation (Roush & Dalton, 2004); a material of this type is typically thought to be responsible for the red spectral slopes of TNOs in g, r, and i band. Figure 6.3 clearly shows this slope should extend through z band as well, so if a tholin-like material dominates the TNO surface we expect TNO z band measurements to correlate clearly with g and r band. However, if TNO surfaces include contributions from an iron-rich material, such as olivine or pyroxene (Clark et al., 2007), these materials are less reflective in z band. With contributions from an olivine material, z band should be significantly decreased relative to g and r, but enhanced relative to J band. Surface pyroxene would also result in a decreased z band reflectance relative to other optical bands and affect the J band flux in a nearly identical manner. Based on the laboratory reflectance spectra in Figure 6.3, I conclude that variations in z band are reasonable due to the range of possible surface compositions, and a large sample of precise multi-band photometry could constrain the major TNO surface components.

The TNOs clearly show a bi-modality in $g - r$ versus $r - z$. The bi-modality is primarily driven by the $g-r$ measurement, however for objects with an average $g-r$ color, knowledge of the z band value aids in differentiating which clump the TNOs belong in. The more 'neutral' colored TNOs, $g - r \lesssim 0.7$, show a correlated slope between the $g-r$ and $r-z$ colors. The majority of these TNOs show the continuation of the red tholin-like slope in the optical, without additional contributions altering the surface reflectance. The redder component of the bi-modality shows a range of colors which indicates these objects likely have different surface compositions, affecting the z band reflectance.

The relative colors of TNOs in $r - z$ and $r - J$ are strongly linked to dynamical classification. The dynamically excited TNOs show a clear correlation between these values; increasing z increases J. The cold classical objects show a more clumped behavior.

6.4.2 Colors of the 5:1 Resonators

The three 5:1 resonators in our sample have a wide range of surface colors. This is true both in $g-r$ and $r-z$. Two of the objects are clearly consistent with the colors of neutral excited objects, and the third is like a red excited surface; none conclusively resemble the cold classical object surfaces (see Figure 6.1). The known 5:1 resonators have surfaces consistent with the dynamically excited population.

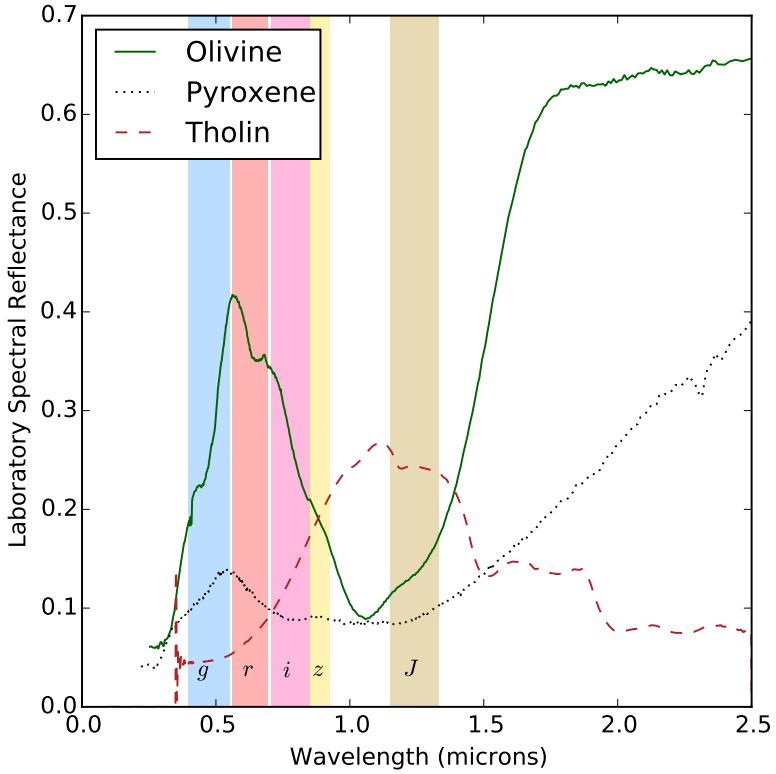

Figure 6.3 The laboratory measured spectral reflectances are plotted for olivine, pyroxene (Clark et al., 2007), and tholin (Roush & Dalton, 2004). Olivine is the solid green line, pyroxene is the dotted black line, and tholin is the dashed red line. If the surfaces of TNOs are exclusively covered by tholins or a similar irradiated organic compound, the z band photometry will provide a continuation of the spectral slope measured for g, r, and i bands. If the surface contains contributions from an iron rich material such as pyroxene or olivine, the z band reflectance should decrease relative to g, r, and i bands and may increase relative to J band.

Dynamically excited populations display a range of $g-r$ surface colors, seen here and in previous work (e.g. Tegler et al., 2003). This range of surface colors may have resulted from formation in different locations closer to the Sun (Brown et al., 2012), followed by scattering into the outer Solar System. Pike et al. (2015) speculates that the 5:1 objects are captured from the scattering objects, and the range of 5:1 resonator surface colors is consistent with the scattering object colors, a dynamically excited TNO population. None of the 5:1 resonators have similar surface colors, suggesting that they did not form together, so it is extremely unlikely they formed in situ or share

formation histories. These objects were likely captured during a scattering event or from the scattering population.

6.5 Conclusion

I explore TNO colors in the z band and determine that z band photometry provides a powerful tool to more precisely discriminate surface groups. The z band reflectance varies relative to g, r, and J band depending on object dynamical classification, and better reveals the bi-modality in the $g - r$ vs $r - z$ colors. A pure irradiated organics composition (such as tholins) would result in z band measurements strongly correlated with g, r, and i bands, as is clearly the case for some of the TNOs. A change in reflectance in z relative to this slope may be due to the presence or absence of silicate materials. TNOs are sufficiently bright in z band for this measurement to be a reasonable addition to a TNO color survey (especially compared to near-infrared observations), and expanding the z band data would provide a useful tool for exploring TNO surface composition.

The 5:1 resonators in the sample exhibit a wide range of surface color. This is consistent with the colors of scattering and most dynamically excited objects. The three entirely different surface properties, implied by the observation of three completely different grz reflectance shapes for these objects, indicates that these objects do not share a formation location.

Chapter 7

Conclusions

This thesis is a detailed study of the 5:1 Neptune resonance, with emphasis on careful understanding and modeling of observational biases. The effects of discovery and followup biases for TNOs can significantly impact our ability to understand the underlying population. The 5:1 resonance contains an unexpectedly large population with an unclear origin; the known objects were discovered in characterized TNO discovery surveys. Survey characterization is important because TNO discovery surveys have biases in object rate of motion, brightness, and sky location. Discovery surveys are typically followed by targeted studies measuring TNO properties, such as light curves or surface color. Followup photometry surveys introduce additional biases because of their selection criteria and measurement efficiency. I focus on understanding and minimizing these effects in order to understand the dynamics, history, and surface properties of the 5:1 Neptune resonators.

I characterize the newly discovered population near the 5:1 Neptune resonance. The three known 5:1 resonators (and a nearby non-resonant object) were recently discovered in Petit et al. (2011) and Kavelaars et al. (2008). I determined the dynamical behavior of the objects near the 5:1 resonance and analyzed their long-term evolution. Three of these TNOs are 5:1 resonators and the fourth is consistent with having been resonant at some point in the past. This object, HL8k1, may have exited the 5:1 resonance through resonance dropout (during planetary migration) or resonance diffusion (in the current Solar System configuration). This non-resonant object is long-term stable and consistent with a steady-state population supplied by the 5:1 resonance. Of the three resonant objects, one is an unstable or temporary resonator and two are likely long-term stable; many of the clones are stable for 4 Gyr. The discovery of these 5:1 resonators is indicative of a significant population in the

distant Kuiper belt.

I combine this classification of three 5:1 resonators with the discovery characteristics of the surveys in order to model the underlying population in a statistically consistent way. I create a parametric model of the resonance and use statistical tests to constrain the range of acceptable orbital parameters, such as inclination, compared to the real detections. Using the survey biases here is critical, because the surveys do not sample all phase space equally, and near the detection limit of the survey, the small changes in survey depth in the different survey fields has a measurable impact on the detectability of objects. I determined that the inclination distribution of the 5:1 resonance was dynamically hot, with $\sigma_i \sim 22°$– likely hotter than the Plutino population. Using the preferred orbital parameters, I calculated the size of the 5:1 resonant population necessary in order to produce the three detected resonators: 1900^{+3300}_{-1400} objects with $H_g < 8$. This population may be as large as the Plutinos, the resonance with the most detections. The large population at high semi-major axis is unexpected based on emplacement in current planetary migration models.

Based on the long-term evolution of the 5:1 particles and their interaction with the scattering objects, I determined that the 5:1 resonance was likely populated via resonance sticking from the scattering objects. A remnant population (non-steady state) of a larger population emplaced in a large scattering event may account for some of the 5:1 resonators, but the escape rate from the resonance indicates that this population would decrease steadily over time. Some 5:1 clones would exit the resonance, scatter, and enter other resonances. If the 5:1 is maintained through resonance sticking, I expect that other distant resonances such as the 6:1 and 7:1 are also heavily populated. Large populations reservoirs in the outer Solar System provide a source population for scattering objects, and thus Centaurs and Jupiter Family Comets. However, these large populations in the distant n:1 resonances are not found in planetary migration models.

I analyzed the migration model from Brasser & Morbidelli (2013, B&M) in detail in an attempt to unravel the origin of the 5:1 resonators. The scattering TNOs produced by the B&M model match the parametric distribution of the scattering TNOs used in the CFEPS model. The relative population sizes of the scattering objects, the 3:1 resonators, and the 4:1 resonators in this model are consistent with the detections and with the population estimates from the surveys. The 5:1 resonance, however, is underpopulated by a factor of ~ 100 compared to population estimates, and ~ 20 when compared to the real detections. This is even more surprising because

the parametric distribution of the 5:1 resonance population created by the B&M simulation is consistent with my models from Pike et al. (2015). The fraction of stable and unstable resonators in the B&M model is consistent with the 2 stable and 1 unstable real objects. The only significant differences between the B&M population and the Pike et al. (2015) parametrization would increase the estimated population size, e.g. the larger e range. Emplacing the 5:1 resonant objects thus requires a population mechanism, such as a scattering event, that is not more efficient than the B&M simulation at populating the 3:1 and 4:1 or implants a population into those resonances that is less stable than the implanted 5:1 resonators.

I also analyzed surface property measurements in order to constrain the source population and emplacement mechanism of the 5:1 resonance. I explored the color distributions of known TNOs and the effects of discovery surveys and followup on the literature color measurements of these objects. Typically TNO color surveys do not describe their selection biases, and these may be difficult for even the authors to quantify in a meaningful way (e.g. TNOs visible on the night of observations). This complicates our understanding of surface properties of TNOs and the distribution of these properties in the outer Solar System. As a member of the Col-OSSOS collaboration, I contributed to the design and execution of a large program to measure TNO surface reflectance in g, r, and J band. Our first semester targets were also measured in z band, which provides another measurement of the spectral slope and likely probes absorption due to silicates. My additional Gemini Fast Turnaround program measured the three 5:1 resonators in g, r, and z band. The colors of the 5:1 resonators span the range of spectral slope behaviors. One has a continuous slope, indicative of the dominant tholin-like reddened surface. The other two show a convex and a concave spectral reflectance, indicative of additional absorption and reflectance in z band relative to r band. This wide range of surface reflectance properties means that the 5:1 resonators do not have a single origin and evolutionary history. These surface properties exclude the primary capture into the resonance being resonance sweeping of nearby primordial objects. If the 5:1 resonance was populated in a major scattering event in the past, the objects captured into the 5:1 resonance must have come from a range of formation locations. This range of surface properties is consistent with the large color range of Centaurs, the low-pericenter scattering objects, and may indicate that the 5:1 resonators are populated through resonance sticking of scattering objects.

There have not been any 5:1 resonators discovered since the CFEPS ecliptic and

high latitude surveys. OSSOS, a current large TNO discovery survey, (Bannister et al., 2016) has surveyed 160 square degrees and has not found any 5:1 resonators. This survey has focused on regions within $\sim 5^\circ$ of the ecliptic plane, so the lack of 5:1 resonator discoveries is not particularly surprising. The three 5:1 resonators all have large inclinations, $i > 20^\circ$. The B&M model supports a high-inclination population in the 5:1 resonance, and is consistent with the inclination distribution of the detections. These high-inclination objects spend significantly less time near the ecliptic plane than low-inclination objects. The inclusion of the OSSOS non-detection fields will better constrain the acceptable inclination distribution of the 5:1 resonators, but will not significantly reduce the population estimate.

7.1 Summary

I have analyzed the dynamics, population, and surface properties of the 5:1 resonators to understand the importance of this population in constraining Solar System formation and evolution. The surface properties and dynamical evolution of these objects suggest this population is maintained through scattering capture. However, the relative population sizes of the scattering objects and 5:1 resonators in migration models is still inconsistent; the scattering objects cannot maintain a population in the 5:1 resonance of the size measured in surveys. The solution may lie in a large scattering event which preferentially populated the 5:1 resonance (and possibly more distant n:1s) with a larger population that is slowly leaking out of resonance, leaving behind a currently enhanced population in the 5:1 resonance.

7.2 Future Work

This work can be explored further through both observations and simulations. Currently, there are no surveys in progress likely to detect 5:1 resonators, so an observational approach would require designing and implementing a large TNO survey off the ecliptic plane. A survey such as this will naturally result from the LSST survey, provided the cadence is appropriate for TNO discoveries (see section 1.6 for details on LSST). LSST will survey all of the visible sky to $m_R \gtrsim 24$, about half a magnitude fainter and with significantly increased coverage compared to CFEPS. This should result in ∼30–100 detections of 5:1 resonators if the population estimate from Pike

et al. (2015) is correct, which would provide additional constraints on the inclination and eccentricity distributions of these TNOs.

Additional dynamical simulations should be tested to see if a large scattering event can sufficiently excite TNOs to distant orbits, such as the 5:1. This likely requires a large jump in Neptune's semi-major axis, which results in a large change in the particles semi-major axes. The inclusion of additional giant planets may also play a role; the ejection of a giant planet could cause energetic scattering. An extra giant planet may have also caused more unstable regions in the Kuiper belt before its removal from the system. Whatever scattering event produces this signature must also be compatible with additional periods of smoother migration, which is likely based on the orbital distribution of the Plutinos.

Future studies of the population in the 5:1 Neptune resonance will continue to explore its utility in constraining the evolution of the giant planets and the Solar System.

Bibliography

Adams, E. R., Gulbis, A. A. S., Elliot, J. L., Benecchi, S. D., Buie, M. W., Trilling, D. E., & Wasserman, L. H. 2014, Astronomical Journal, 148, 55

Aitken, R. G. 1926, Publications of the ASP, 38, 277

Alexandersen, M., Gladman, B., Greenstreet, S., Kavelaars, J. J., Petit, J.-M., & Gwyn, S. 2013, Science, 341, 994

Alexandersen, M., Gladman, B., Kavelaars, J. J., Petit, J.-M., Gwyn, S., Shankman, C., & Pike, R. E. 2016, Astronomical Journal, Accepted

Allen, R. L., Gladman, B., Kavelaars, J. J., Petit, J.-M., Parker, J. W., & Nicholson, P. 2006, Astrophysical Journal, Letters to the Editor, 640, L83

ALMA Partnership et al. 2015, Astrophysical Journal, Letters to the Editor, 808, L3

Anderson, T. W. & Darling, D. A. 1952, Ann. Math. Statist., 23, 193

Anderson, T. W. & Darling, D. A. 1954, Journal of the American Statistical Association, 49, 765

Bannister, M. 2016, P&SS, Accepted

Bannister, M. T. et al. 2016, Astronomical Journal, Accepted

Barucci, M. A., Brown, M. E., Emery, J. P., & Merlin, F. 2008, Composition and Surface Properties of Transneptunian Objects and Centaurs, ed. M. A. Barucci, H. Boehnhardt, D. P. Cruikshank, A. Morbidelli, & R. Dotson, 143–160

Barucci, M. A., Cruikshank, D. P., Dotto, E., Merlin, F., Poulet, F., Dalle Ore, C., Fornasier, S., & de Bergh, C. 2005, Astronomy and Astrophysics, 439, L1

Batygin, K., Brown, M. E., & Fraser, W. C. 2011, Astrophysical Journal, 738, 13

Beauge, C. 1994, Celestial Mechanics and Dynamical Astronomy, 60, 225

Belskaya, I. N., Levasseur-Regourd, A.-C., Shkuratov, Y. G., & Muinonen, K. 2008, Surface Properties of Kuiper Belt Objects and Centaurs from Photometry and Polarimetry, ed. M. A. Barucci, H. Boehnhardt, D. P. Cruikshank, A. Morbidelli, & R. Dotson, 115–127

Benecchi, S. D., Noll, K. S., Grundy, W. M., Buie, M. W., Stephens, D. C., & Levison, H. F. 2009, Icarus, 200, 292

Benecchi, S. D. & Sheppard, S. S. 2013, Astronomical Journal, 145, 124

Bernstein, G. & Khushalani, B. 2000, Astronomical Journal, 120, 3323

Bernstein, G. M., Trilling, D. E., Allen, R. L., Brown, M. E., Holman, M., & Malhotra, R. 2004, Astronomical Journal, 128, 1364

Beust, H. et al. 2014, Astronomy and Astrophysics, 561, A43

Booth, M., Wyatt, M. C., Morbidelli, A., Moro-Martín, A., & Levison, H. F. 2009, Monthly Notices of the RAS, 399, 385

Brasser, R. & Morbidelli, A. 2013, Icarus, 225, 40

Brasser, R., Schwamb, M. E., Lykawka, P. S., & Gomes, R. S. 2012, Monthly Notices of the RAS, 420, 3396

Brown, M. E. 2001, Astronomical Journal, 121, 2804

— 2002, Annual Review of Earth and Planetary Sciences, 30, 307

— 2012, Annual Review of Earth and Planetary Sciences, 40, 467

Brown, M. E., Barkume, K. M., Ragozzine, D., & Schaller, E. L. 2007, Nature, 446, 294

Brown, M. E., Burgasser, A. J., & Fraser, W. C. 2011, Astrophysical Journal, Letters to the Editor, 738, L26

Brown, M. E., Schaller, E. L., & Fraser, W. C. 2012, Astronomical Journal, 143, 146

Brunetto, R., Barucci, M. A., Dotto, E., & Strazzulla, G. 2006, Astrophysical Journal, 644, 646

Campbell, W. W. 1916, The Scientific Monthly, 3, 521

Chiang, E. I. & Jordan, A. B. 2002, Astronomical Journal, 124, 3430

Chiang, E. I. et al. 2003, Astronomical Journal, 126, 430

Clark, R. N., Swayze, G. A., Wise, R., Livo, E., Hoefen, T., Kokaly, R., & Sutley, S. J. 2007, USGS digital spectral library splib06a: U.S. Geological Survey, Digital Data Series 231, `http://speclab.cr.usgs.gov/spectral.lib06`

Cruikshank, D. P., Roush, T. L., & Poulet, F. 2003, Comptes Rendus Physique, 4, 783

Dalle Ore, C. M., Dalle Ore, L. V., Roush, T. L., Cruikshank, D. P., Emery, J. P., Pinilla-Alonso, N., & Marzo, G. A. 2013, Icarus, 222, 307

Davies, J. K., McFarland, J., Bailey, M. E., Marsden, B. G., & Ip, W.-H. 2008, The Early Development of Ideas Concerning the Transneptunian Region, ed. M. A. Barucci, H. Boehnhardt, D. P. Cruikshank, A. Morbidelli, & R. Dotson, 11–23

Dawson, R. I. & Murray-Clay, R. 2012, Astrophysical Journal, 750, 43

Delsanti, A. & Jewitt, D. 2006, The Solar System Beyond The Planets, ed. P. Blondel & J. W. Mason (Springer), 267

Doressoundiram, A., Peixinho, N., Doucet, C., Mousis, O., Barucci, M. A., Petit, J. M., & Veillet, C. 2005, Icarus, 174, 90

Duncan, M., Quinn, T., & Tremaine, S. 1988, Astrophysical Journal, Letters to the Editor, 328, L69

Duncan, M. J. & Levison, H. F. 1997, Science, 276, 1670

Duncan, M. J., Levison, H. F., & Lee, M. H. 1998, Astronomical Journal, 116, 2067

Edgeworth, K. E. 1949, Monthly Notices of the RAS, 109, 600

— 1961, The earth, the planets, and the stars

Elliot, J. L. et al. 2005, Astronomical Journal, 129, 1117

— 2007, Astronomical Journal, 134, 1

Fernandez, J. A. 1980, Monthly Notices of the RAS, 192, 481

Fernandez, J. A. & Ip, W.-H. 1981, Icarus, 47, 470

Fornasier, S. et al. 2004, Astronomy and Astrophysics, 421, 353

Fraser, W. et al. 2016, The Astronomical Journal, 151, 158

Fraser, W. C. & Brown, M. E. 2012, Astrophysical Journal, 749, 33

Fraser, W. C., Brown, M. E., & Glass, F. 2015, Astrophysical Journal, 804, 31

Fraser, W. C., Brown, M. E., Morbidelli, A., Parker, A., & Batygin, K. 2014, Astrophysical Journal, 782, 100

Gallardo, T. 2006, Icarus, 181, 205

Gallardo, T., Hugo, G., & Pais, P. 2012, Icarus, 220, 392

Gardner, J. P. et al. 2006, Space Sci. Rev., 123, 485

Gladman, B., Holman, M., Grav, T., Kavelaars, J., Nicholson, P., Aksnes, K., & Petit, J.-M. 2002, Icarus, 157, 269

Gladman, B., Kavelaars, J. J., Petit, J.-M., Morbidelli, A., Holman, M. J., & Loredo, T. 2001, Astronomical Journal, 122, 1051

Gladman, B. et al. 2012, Astronomical Journal, 144, 23

Gladman, B., Marsden, B. G., & Vanlaerhoven, C. 2008, Nomenclature in the Outer Solar System, ed. M. A. Barucci, H. Boehnhardt, D. P. Cruikshank, A. Morbidelli, & R. Dotson, 43–57

Gomes, R. S. 2003, Icarus, 161, 404

Gomes, R. S., Fern Ndez, J. A., Gallardo, T., & Brunini, A. 2008, The Scattered Disk: Origins, Dynamics, and End States, ed. M. A. Barucci, H. Boehnhardt, D. P. Cruikshank, A. Morbidelli, & R. Dotson, 259–273

Gomes, R. S., Gallardo, T., Fernández, J. A., & Brunini, A. 2005, Celestial Mechanics and Dynamical Astronomy, 91, 109

Gulbis, A. A. S., Elliot, J. L., Adams, E. R., Benecchi, S. D., Buie, M. W., Trilling, D. E., & Wasserman, L. H. 2010, Astronomical Journal, 140, 350

Hahn, J. M. & Malhotra, R. 2005, Astronomical Journal, 130, 2392

Hainaut, O. R. & Delsanti, A. C. 2002, Astronomy and Astrophysics, 389, 641

Hamid, S. E., Marsden, B. G., & Whipple, F. L. 1968, Astronomical Journal, 73, 727

Holman, M. J. & Wisdom, J. 1993, Astronomical Journal, 105, 1987

Ivezic, Z. et al. 2008, Serbian Astronomical Journal, 176, 1

Ivezić, Ž. et al. 2001, Astronomical Journal, 122, 2749

Janson, M., Carson, J. C., Lafrenière, D., Spiegel, D. S., Bent, J. R., & Wong, P. 2012, Astrophysical Journal, 747, 116

Jewitt, D. & Luu, J. 1993, Nature, 362, 730

Jewitt, D. C. & Luu, J. X. 2001, Astronomical Journal, 122, 2099

Jones, R. L. et al. 2006, Icarus, 185, 508

Jones, R. L., Parker, J. W., Bieryla, A., Marsden, B. G., Gladman, B., Kavelaars, J., & Petit, J.-M. 2010, Astronomical Journal, 139, 2249

Jordi, K., Grebel, E. K., & Ammon, K. 2006, Astronomy and Astrophysics, 460, 339

JWST Collaboration 2016, Explore James Webb Space Telescope, `http://jwst.nasa.gov/about.html`, accessed 2016-01-10.

Kaib, N. A., Roškar, R., & Quinn, T. 2011, Icarus, 215, 491

Kalas, P. et al. 2008, Science, 322, 1345

Kalas, P., Graham, J. R., & Clampin, M. 2005, Nature, 435, 1067

Kalas, P., Graham, J. R., Fitzgerald, M. P., & Clampin, M. 2013, Astrophysical Journal, 775, 56

Kaňuchová, Z., Brunetto, R., Melita, M., & Strazzulla, G. 2012, Icarus, 221, 12

Kavelaars, J. 2016, Private Communication.

Kavelaars, J. J., Gladman, B., Petit, J., Parker, J. W., & Jones, L. 2008, in Bulletin of the American Astronomical Society, Vol. 40, AAS/Division for Planetary Sciences Meeting Abstracts #40, 481

Kavelaars, J. J. et al. 2009, Astronomical Journal, 137, 4917

Kowal, C. T. 1989, Icarus, 77, 118

Kowal, C. T., Liller, W., & Marsden, B. G. 1979, in IAU Symposium, Vol. 81, Dynamics of the Solar System, ed. R. L. Duncombe, 245–250

Kozai, Y. 1962, Astronomical Journal, 67, 591

Kuiper, G. P. 1951, Proceedings of the National Academy of Science, 37, 1

Lawler, S. M. & Gladman, B. 2013, Astronomical Journal, 146, 6

Lawler, S. M., Greenstreet, S., & Gladman, B. 2015, Astrophysical Journal, Letters to the Editor, 802, L20

Lazzarin, M., Barucci, M. A., Boehnhardt, H., Tozzi, G. P., de Bergh, C., & Dotto, E. 2003, Astronomical Journal, 125, 1554

Levison, H. & Duncan, M. 1989, in Bulletin of the American Astronomical Society, Vol. 21, Bulletin of the American Astronomical Society, 1144

Levison, H. F. 1996, in Astronomical Society of the Pacific Conference Series, Vol. 107, Completing the Inventory of the Solar System, ed. T. Rettig & J. M. Hahn, 173–191

Levison, H. F. & Duncan, M. J. 1993, Astrophysical Journal, Letters to the Editor, 406, L35

— 1994, Icarus, 108, 18

Levison, H. F., Morbidelli, A., Van Laerhoven, C., Gomes, R., & Tsiganis, K. 2008, Icarus, 196, 258

Lidov, M. L. 1962, Planet. Space Sci., 9, 719

LSST Corporation 2016, Large Synoptic Survey Telescope: Opening a Window of Discovery on the Dynamic Universe, `http://www.lsst.org/about/timeline`, accessed 2016-01-10.

Luu, J. & Jewitt, D. 1996, Astronomical Journal, 112, 2310

Luu, J. X. & Jewitt, D. 1988, Astronomical Journal, 95, 1256

Lykawka, P. S. & Mukai, T. 2006, Planet. Space Sci., 54, 87

— 2007a, Icarus, 189, 213

— 2007b, Icarus, 192, 238

— 2008, Astronomical Journal, 135, 1161

Malhotra, R. 1993, Nature, 365, 819

— 1995, Astronomical Journal, 110, 420

— 1996, Astronomical Journal, 111, 504

Marengo, M., Stapelfeldt, K., Werner, M. W., Hora, J. L., Fazio, G. G., Schuster, M. T., Carson, J. C., & Megeath, S. T. 2009, Astrophysical Journal, 700, 1647

Mastrapa, R. M. E. 2010, NASA Planetary Data System, 126

Monet, D. G. et al. 2003, Astronomical Journal, 125, 984

Morbidelli, A., Levison, H. F., Tsiganis, K., & Gomes, R. 2005, Nature, 435, 462

Morbidelli, A., Thomas, F., & Moons, M. 1995, Icarus, 118, 322

Moroz, L., Baratta, G., Strazzulla, G., Starukhina, L., Dotto, E., Barucci, M. A., Arnold, G., & Distefano, E. 2004, Icarus, 170, 214

Murray-Clay, R. A. & Chiang, E. I. 2005, Astrophysical Journal, 619, 623

Nesvorný, D. 2015a, Astronomical Journal, 150, 73

— 2015b, Astronomical Journal, 150, 68

Nesvorný, D. & Morbidelli, A. 2012, Astronomical Journal, 144, 117

Nesvorný, D. & Roig, F. 2000, Icarus, 148, 282

Noll, K. S., Grundy, W. M., Chiang, E. I., Margot, J.-L., & Kern, S. D. 2008, Binaries in the Kuiper Belt, ed. M. A. Barucci, H. Boehnhardt, D. P. Cruikshank, A. Morbidelli, & R. Dotson, 345–363

Oort, J. H. 1950, Bulletin Astronomical Institute of the Netherlands, 11, 91

Palumbo, M. E., Ferini, G., & Baratta, G. A. 2004, Advances in Space Research, 33, 49

Parker, A. et al. 2016, Publications of the ASP, 128, 018010

Parker, A. H. & Kavelaars, J. J. 2010, Astrophysical Journal, Letters to the Editor, 722, L204

Peixinho, N., Delsanti, A., & Doressoundiram, A. 2015, Astronomy and Astrophysics, 577, A35

Peixinho, N., Delsanti, A., Guilbert-Lepoutre, A., Gafeira, R., & Lacerda, P. 2012, Astronomy and Astrophysics, 546, A86

Peixinho, N., Doressoundiram, A., Delsanti, A., Boehnhardt, H., Barucci, M. A., & Belskaya, I. 2003, Astronomy and Astrophysics, 410, L29

Petit, J.-M., Kavelaars, J. J., Gladman, B., Jones, L., & Parker, J. 2014, in AAS/Division for Planetary Sciences Meeting Abstracts, Vol. 46, AAS/Division for Planetary Sciences Meeting Abstracts, 507.07

Petit, J.-M. et al. 2011, Astronomical Journal, 142, 131

Pike, R. E. & Kavelaars, J. J. 2013, Astronomical Journal, 146, 75

Pike, R. E., Kavelaars, J. J., Petit, J. M., Gladman, B. J., Alexandersen, M., Volk, K., & Shankman, C. J. 2015, Astronomical Journal, 149, 202

Roush, T. L. & Dalton, J. B. 2004, Icarus, 168, 158

Schwamb, M. et al. 2016, In Prep.

Shankman, C., Amélard, R., Kavelaars, J., Pike, R. E., & Wong, A. 2016a, In prep.

Shankman, C., Gladman, B. J., Kaib, N., Kavelaars, J. J., & Petit, J. M. 2013, Astrophysical Journal Letters, 764, L2

Shankman, C. et al. 2016b, Astronomical Journal, 151, 31

Sheppard, S. S. 2012, Astronomical Journal, 144, 169

Skrutskie, M. F. et al. 2006, Astronomical Journal, 131, 1163

Stern, A. 2016, New Horizons, http://pluto.jhuapl.edu/News-Center/PI-Perspectives.php?page=piPerspective_10_23_2014, accessed 2016-01-10.

Stern, S. A. et al. 2015, Science, 350, aad1815

Stetson, P. B. & Harris, W. E. 1988, Astronomical Journal, 96, 909

Tegler, S. C., Romanishin, W., & Consolmagno, G. J. 2003, Astrophysical Journal, Letters to the Editor, 599, L49

Thomas, F. & Morbidelli, A. 1996, Celestial Mechanics and Dynamical Astronomy, 64, 209

Thommes, E. W., Duncan, M. J., & Levison, H. F. 1999, Nature, 402, 635

Tiscareno, M. S. & Malhotra, R. 2009, Astronomical Journal, 138, 827

Tody, D. 1993, in Astronomical Society of the Pacific Conference Series, Vol. 52, Astronomical Data Analysis Software and Systems II, ed. R. J. Hanisch, R. J. V. Brissenden, & J. Barnes, 173

Trilling, D. E. & Bernstein, G. M. 2006, Astronomical Journal, 131, 1149

Trujillo, C. A. 2008, Future Surveys of the Kuiper Belt, ed. M. A. Barucci, H. Boehnhardt, D. P. Cruikshank, A. Morbidelli, & R. Dotson, 573–585

Trujillo, C. A. & Brown, M. E. 2003, Earth Moon and Planets, 92, 99

Trujillo, C. A., Brown, M. E., Rabinowitz, D. L., & Geballe, T. R. 2005, Astrophysical Journal, 627, 1057

Trujillo, C. A. & Sheppard, S. S. 2014, Nature, 507, 471

Trujillo, C. A., Sheppard, S. S., & Schaller, E. L. 2011, Astrophysical Journal, 730, 105

Tsiganis, K., Gomes, R., Morbidelli, A., & Levison, H. F. 2005, Nature, 435, 459

Vilenius, E. et al. 2012, Astronomy & Astrophysics, 541, A94

Volk, K. et al. 2016, The Astronomical Journal, 152, 23

Whipple, F. L. 1950, Astronomical Journal, 55, 83

— 1964, Proceedings of the National Academy of Science, 51, 711

Williams, J. G. & Benson, G. S. 1971, Astronomical Journal, 76, 167

Wisdom, J. & Holman, M. 1991, Astronomical Journal, 102, 1528

Wyatt, M. C. & Dent, W. R. F. 2002, Monthly Notices of the RAS, 334, 589

Wyatt, M. C., Dermott, S. F., Telesco, C. M., Fisher, R. S., Grogan, K., Holmes, E. K., & Piña, R. K. 1999, Astrophysical Journal, 527, 918

Wyatt, M. C., Holland, W. S., Greaves, J. S., & Dent, W. R. F. 2003, Earth Moon and Planets, 92, 423